Universidad Michoacana de San Nicolás de Hidalgo

Instituto de Física y Matemáticas

Tesis

que para obtener el grado de

Doctora en Ciencias en el Área de la Física

Unraveling the internal structure of pseudo-scalar mesons: From Form Factors to Generalized Parton Distributions

Presenta:

M.C. Isela Melany Higuera Angulo

Director de tesis :

Prof. Adnan Bashir

Morelia, Michoacán, México.

Noviembre 2023

Dedicated to my beloved mother.

Acknowledgements

I take this opportunity to acknowledge and express my gratitude to all those who supported and guided me during my Ph.D. ...

In addition, I would like to thank CONACyT (Mexico) for the scholarship received to carry out my postgraduate studies.

Abstract

We conducted an extensive investigation into the internal structure of pseudo-scalar mesons, employing a unified algebraic model based on the Schwinger-Dyson equations (SDEs). Our study involved the calculation of various non-perturbative objects, such as electromagnetic (EFFs) and transition form factors (TFFs), parton distribution functions (PDFs), generalized parton distributions (GPDs), and impact parameter space GPDs.

To achieve this, we employed two different approaches: the overlap approximation in the light front formalism and the triangle diagram approximation (impulse approximation). The overlap approximation of the light front wave function straitly related to the distribution amplitudes of quarks, allowed us to construct the GPDs, providing a 3D image of mesons. From these GPDs, we derived PDFs, EFFs, and the impact parameter space GPD. Furthermore, the PDFs of mesons containing the light valence quarks were evolved from the hadronic scale of approximately 0.3 GeV to the experimentally relevant scale of 5.2 GeV.

Concurrently, the triangle diagram approximation facilitated the construction of EFFs and TFFs ($\mathrm{M} \to \gamma\gamma^*$) in a simplified manner. This approach enabled us to fit the model's parameters through a global analysis, leading to excellent agreement with experimental and phenomenological results. We also determined the charge radius end presented our results for pion, kaon, η_c, and η_b using the algebraic model and compared these findings with previous theoretical approaches, including SDEs and lattice.

Furthermore, we collaborated on an exhaustive study of EFFs for all light, heavy-light, and heavy ground-state scalar and pseudoscalar mesons. This research was based on the treatment of SDEs involving a vector $\times$ vector contact interaction.

Through these endeavors, we gained a comprehensive understanding of the capabilities and limitations of the algebraic model and the contact interaction model concerning pseudoscalar mesons. Our research significantly contributes to advancing our knowledge of the internal structure of these mesons, providing valuable insights for future studies.

Resumen

Realizamos una extensa investigación sobre la estructura interna de los mesones pseudoescalares, empleando un modelo algebraico unificado basado en las ecuaciones de Schwinger-Dyson (SDEs). Nuestro estudio involucró el cálculo de varios objetos no perturbadores, como factores de forma electromagnéticos (EFFs) y de transición (TFFs), funciones de distribución de partones (PDFs), distribuciones generalizadas de partones (GPDs) y el parámetro de impacto del espacio de GPD.

Para lograr esto, empleamos dos enfoques diferentes: la aproximación de superposición en el formalismo de frente de luz y la aproximación del diagrama de triángulo (aproximación de impulso). La aproximación de superposición de la función de onda del frente de luz (estrechamente relacionada con las amplitudes de distribución de los quarks), nos permitió construir los GPDs, proporcionando una imagen 3D de los mesones. A partir de estos GPDs, derivamos las PDFs, EFFs y el parámetro de impacto del espacio de GPDs. Además, las PDFs de los mesones que contienen los quarks de valencia ligeros se evolucionaron desde la escala hadrónica de aproximadamente 0.3 GeV a la escala experimental relevante de 5.2 GeV.

Al mismo tiempo, la aproximación del diagrama de triángulos facilitó la construcción de EFFs y TFFs ($\mathrm{M} \to \gamma\gamma^*$) de manera simplificada. Este enfoque nos permitió ajustar los parámetros del modelo a través de un análisis global, lo que llevó a una excelente concordancia con los resultados experimentales y fenomenológicos. También determinamos el radio de carga y presentamos nuestros resultados para pion, kaon, η_c y η_b utilizando el modelo algebraico y comparamos estos hallazgos con enfoques teóricos anteriores, incluidas las SDEs y Lattice.

Además, colaboramos en un estudio exhaustivo de los EFFs para todos los mesones escalares y pseudoescalares ligeros, pesados-ligeros y pesados. Esta investigación se

basó en el tratamiento de las SDEs que involucran una interacción de contacto vector $\times$ vector.

A través de estos esfuerzos, obtuvimos una comprensión integral de las capacidades y limitaciones del modelo algebraico y el modelo de interacción de contacto con respecto a los mesones pseudoescalares. Nuestra investigación contribuye significativamente al avance de nuestro conocimiento de la estructura interna de estos mesones, proporcionando información valiosa para futuros estudios.

Modelo Algebraico, Imagen tridimensional, Ecuaciones de Schwinger-Dyson, Funciones de Distribución, Factores de Forma de Transición.

Contents

Chapter 1

Introduction

Particle physics delves into the fundamental building blocks of the universe and the forces that control their interactions. At the heart of this endeavor lies the well-known Standard Model, the most successful framework to date that elegantly encapsulates these components across the spectrum of the fundamental forces: electromagnetic, weak, and strong nuclear. However, our journey is far from complete. As we venture deeper, the mysteries invite us to explore further. For instance, some of the more enigmatic unresolved phenomena concerning strong interactions are confinement and dynamical mass generation, which plays a crucial role on the spectrum and dynamics of nuclear and hadronic structure [1].

The masses of particles, once attributed to the Higgs boson [2], raise deeper questions about the mechanisms underlying the dynamical mass generation. Since, despite the essential role played by the Electro-Weak symmetry breaking, it contributes only a marginal fraction to the overall mass of visible matter. Surprisingly, about 98% of the total visible matter mass is due to dynamical chiral symmetry breaking (DCSB) [3], a mechanism intrinsically related to strong interactions. Quantum Chromodynamics (QCD), is the theory that describes strong interactions between its degrees of freedom -quarks and gluons-, the only particles not found freely in nature, implying that they are confined within hadrons [4–6], but also, presenting asymptotic freedom at high energy scales [7–9]. The confinement property presents a challenge in the description of the hadronic structure in terms of quarks and gluons from first principles. Since, perturbative studies become impossible at low energy scales due to the QCD's coupling constant.

Consequently, emerging concepts aim to improve our understanding of hadrons, such as "factorization" [10], which represents high-energy processes as a convolution of partonic subprocess happening at the given hard scale and non-perturbative objects, such as Parton Distribution Functions (PDFs), Form Factors (FFs), and Generalized Parton Distributions (GPDs), encapsulating information about hadron structure.

In recent decades, all over the world several accelerators have been built, like Jefferson Lab (JLab), Large Hadron Collider (LHC), German Electron Synchrotron (DESY), Relativistic Heavy Ion Collider (RHIC), High Energy Accelerator Research Organization (KEK), Stanford Linear Accelerator Center (SLAC), among others, which have generated a vast amount of experimental data, playing a significant role in the experimental pursuits [11–20]. The horizon looks even brighter with ongoing projects like JLab12 and, on a broader timescale, the ambitious Electron-Ion Collider (EIC) planned for potential construction in the U.S. during the 2020s [21–25].

The development of phenomenological models can help to improve agreement with available experimental data, but they inherently fall short of providing a complete dynamic understanding, like how GPDs are generated from the fundamental degrees of freedom of the theory. For this level of comprehension, models based in non-perturbative methods are indispensable. The method discussed here is based on the Schwinger-Dyson equations (SDEs) [26], which have achieved notable success. Nevertheless, the fusion of phenomenological and theoretical approaches enables a comprehensive harmony between experimental data and theoretical frameworks, giving a better understanding of the nature of hadrons [27, 28].

The structure of this thesis is as follows: Chapter 1 introduces the historical discovery of the hadron internal structure and the beginning of QCD. QCD's symmetry, Lagrangian, and chiral symmetry breaking will be discussed. Chapter 2 advances in the theoretical definitions of our interest equations such as the EFFs, PDFs, GPDs, and the parton distribution amplitudes (PDAs). Chapter 3 explains SDEs, their underlying physics, and the developed models that will help us to obtain the non-perturbative functions of the following chapters. Then, in Chapter 4 we find the computation and extraction of the GPDs, PDFs, EFFs, and impact parameter space GPD, on the light-front formalism through its respective PDA. Chapter 5 shows the analytical development and the extraction of EFFs and TFFs through the triangle diagram with two approaches that are the Contact Interaction (CI) model and the Algebraic Model (AM). Finally, in

Chapter 6, we discuss the results obtained by comparing and summarizing the findings of the different methods and models, and concludes this work.

1.1 The structure of hadrons and the beginning of a theory

1.1.1 The internal structure of nucleons

Since Ernest Rutherford's discovery of the proton in 1919 [29], scientists thought of it as a point-like particle. However, in the early 1930s, the proton's magnetic moment was first measured [30], revealing substantial deviations from the predictions derived from Paul Dirac's equation, which had treated the proton as a point particle. This offered the first indication of the internal complexity of the proton.

However, it was until 1953 that Hofstadter's breakthrough came to light [31]. Through the elastic scattering of electrons on nucleons, his experiments dismantled the notion of nucleons as rigid, indivisible point particles and instead exhibited a charge and current distribution within them, as visually depicted in Figure 1.1. This suggested

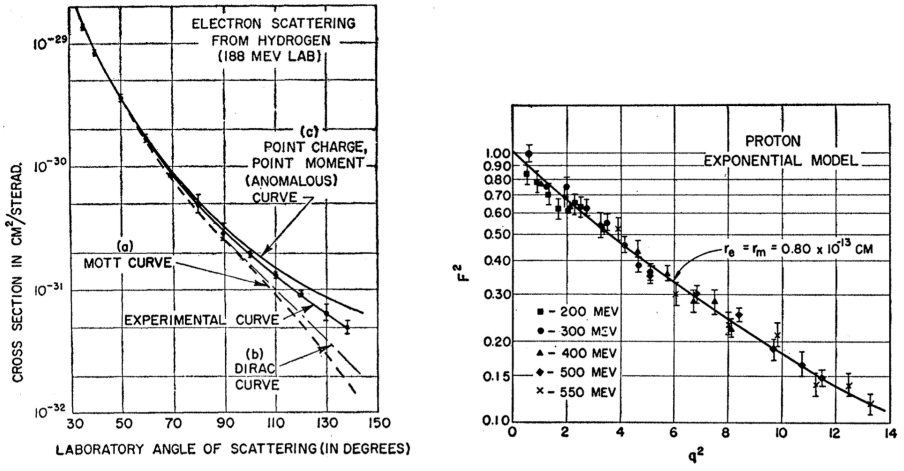

FIGURE 1.1: Original measurements by Hofstadter taken from [32]. Left panel- Cross section of an electron-proton scattering from a proton. Right panel- Proton form factor as a function of the photon incidence energy, q^2.

that the cross section of such a process would require the existence of form factors, the presence of which would lead to a reduction of the effective values of the charge and

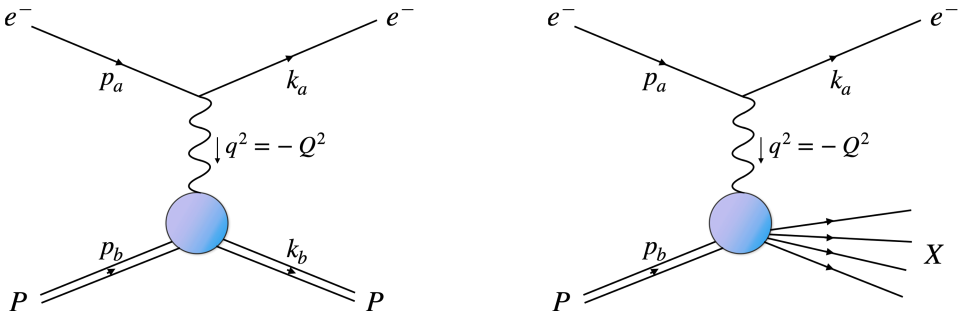

FIGURE 1.2: Left panel- Elastic scattering for a $e^- p \to e^- p$ collision. Right panel- $e^- p$ Deep Inelastic Scattering.

magnetic moment. In essence, the calculation of the amplitude of the elastic scattering $e^- p \to e^- p$ represented in the left panel of Figure 1.2 is as follows:

$$\begin{aligned} \mathcal{M}(e^- p \to e^- p) &= j^{\mu}_{e^-}(p_a, k_a)\Big(i\Delta^0_{\mu\nu}(q)\Big) j^{\mu}_{p}(p_b, k_b) \\ &= \frac{e^2}{q^2}\overline{u}_e(k_a)\gamma^{\mu}u_e(p_a)\langle p_b|j^{\mu}_p(0)|k_b\rangle\,, \end{aligned} \tag{1.1}$$

where e is the electric charge. Consequently, the resulting spin average invariant amplitude becomes:

$$\overline{|\mathcal{M}(e^- p \to e^- p)|^2} = \frac{e^4}{q^4} L^e_{\mu\nu} W^{\mu\nu}_p\,, \tag{1.2}$$

with,

$$L^e_{\mu\nu} \equiv \frac{1}{2}\sum_{s_e}\Big(\overline{u}_e(k_A)\gamma_{\mu}u_e(p_A)\Big)\Big(\overline{u}_e(k_A)\gamma_{\nu}u_e(p_A)\Big)^*\,, \tag{1.3}$$

$$W^{\mu\nu}_p \equiv \frac{1}{2}\sum_{s_p}\Big(\overline{v}_p(k_B)\gamma^{\mu}v_p(p_B)\Big)\Big(\overline{v}_p(k_B)\gamma^{\nu}v_p(p_B)\Big)^*\,, \tag{1.4}$$

where the sum is over the projections of the spin of the electron (s_e) and the proton (s_p). This, in turn, leads to the cross section for a 1/2-spin particle:

$$\frac{d\sigma}{d\Omega}(e^- p \to e^- p) = \left(\frac{d\sigma}{d\Omega}\right)_{\text{Mott}}\left[A(q^2) + B(q^2)\tan^2(\theta/2)\right]\,, \tag{1.5}$$

where θ is the scattering angle of the electron, Ω is the solid angle of the outgoing electron and $q^2 = -Q^2$ is the square momentum transferred by the photon mediating the interaction. Furthermore, $(d\sigma/d\Omega)_{Mott}$ is the cross section associated to the scattering

between an electron and a fundamental spin-0 particle, the subscript "Mott" is in honor of the scientist Nevill Francis Mott, and is given by:

$$\left(\frac{d\sigma}{d\Omega}\right)_{\text{Mott}} = \frac{\alpha_{em}^2 \cos^2(\theta/2)}{16 M_p^2 E_e^{i\,2} \sin^4(\theta/2)} \frac{E_e^i}{E_e^f} \,. \tag{1.6}$$

E_e^i y E_e^f are the electron initial and final energies, respectively, and M_p is the proton mass. Finally, $A(q^2)$ and $B(q^2)$ are the introduced electric and magnetic form factors. Fundamentally, these form factors would not depend on Q^2 for a point particle. Something that indeed was not observed by Hofstadter's results, as seen in the right panel of Figure 1.1, confirming that the proton possesses an extended nature and giving him the Novel Prize in 1961. Actually, these functions are related with the Saks's electric and magnetic form factors G_E y G_M, of proton in the following form:

$$A(q^2) = \frac{G_E^2(q^2) + \tau G_M^2(q^2)}{1+\tau} \,, \tag{1.7}$$

$$B(q^2) = 2\tau G_M^2(q^2) \,. \tag{1.8}$$

In a corresponding manner, these form factors are interconnected with the renowned Dirac (F_1) and Pauli (F_2) form factors, outlined as follows:

$$G_E(q^2) = F_1(q^2) - \tau\kappa F_2(q^2) \,, \tag{1.9}$$

$$G_M(q^2) = F_1(q^2) + \kappa F_2(q^2) \,, \tag{1.10}$$

where $F_1(0) = F_2(0) = 1$. And finally, in the previous expressions, κ is the anomalous magnetic moment of the proton, τ is a scaling variable defined as $\tau = Q^2/4M_p^2$.

The next decade was characterized by a profusion of conceptual developments concerning the potential constituents of nucleons (protons and neutrons) and another large array of particles, referred to as *hadrons*, that were being discovered concurrently. Initially, these particles were categorized based on their charge and isospin according to their strangeness. To obtain further insights, hadrons were classified into groups with similar properties and masses, a process facilitated by the "*eightfold way*" method introduced in 1961 by Gell-Mann and Yuval Ne'eman [33]. Additionally, in 1964, Gell-Mann and George Zweig proposed that the structure of hadron could be explained by adding a new quantum number called *flavor*, derived from subatomic constituents called *quarks*. This concept aimed to elucidate the diversity of hadrons through the SU(3) symmetry. This model gained credibility by predicting the existence of the Ω^- baryon. Yet, the

quark model encountered initial inconsistencies. The Δ^{++} baryon, in the quark model, is composed of three up quarks with parallel spins, which violate the Pauli exclusion principle.

In 1964-1965, independent solutions emerged from Greenberg and Han-Nambu. They proposed an added gauge degree of freedom—later referred to as *color* charge—for quarks, within $SU_c(3)$ symmetry. Han and Nambu noted that quarks could interact via an octet of vector gauge bosons known as *gluons*. This marked the inception of Quantum Chromodynamics (QCD).

However, in the late 1960s, new visualizations emerged with the first Deep Inelastic Scattering (DIS) experiment at SLAC12 [34, 35]. This experiment yielded fresh visualizations that affirmed the reality of quarks as genuine particles, a concept Richard Feynman called "*partons*".

1.1.2 Parton Model

In 1969, Bjorken [36, 37] and Feynman [38] provided crucial insights into deep inelastic scattering (DIS) measurements by proposing that the proton was comprised of point-like particles with spin 1/2. This groundbreaking concept, known as the "*parton model*", aligned well with the experimental results from SLAC. The key characteristics of the parton model are summarized below. With P as the momentum of the target hadron, we can express the invariant amplitude of the processes $e^- p \to e^- X$ (shown in the right panel of Figure 1.2) in terms of the leptonic ($L^e_{\mu\nu}$) and hadronic ($W^{\mu\nu}_p$) tensors, analogous to Eq. (1.2), as:

$$\overline{|\mathcal{M}(e^- p \to e^- X)|^2} = \frac{e^4}{q^4} L^e_{\mu\nu} W^{\mu\nu}_X \,. \tag{1.11}$$

Leading to the cross-section:

$$\frac{d^2\sigma}{d^2\Omega dE^f_e} = \frac{\alpha^2_{em}}{Q^2} \frac{E^f_e}{E^i_e} L^e_{\mu\nu} W^{\mu\nu}_p \,. \tag{1.12}$$

The leptonic tensor is entirely described by Quantum Electrodynamics (QED) and can be calculated at the tree level as follows:

$$L^e_{\mu\nu} = 2\left(p^\mu_a k^\nu_a + k^\mu_a p^\nu_a - \frac{Q^2}{2} g^{\mu\nu}\right) , \tag{1.13}$$

where $g^{\mu\nu}$ is the metric tensor. However, the hadronic tensor cannot be computed directly beforehand. Nevertheless, Hermiticity and current conservation yield:

$$W^{\mu\nu}_p = W^{\nu\mu}_p \, , \tag{1.14}$$

$$q_\mu W^{\mu\nu}_p = 0 \, . \tag{1.15}$$

Hence, the hadronic tensor can be expressed in terms of two essential structure functions, $W_1(Q^2, \nu)$ and $W_2(Q^2, \nu)$:

$$W^{\mu\nu}_p = W_1(Q^2,\nu)\left(g^{\mu\nu} - \frac{q^\mu q^\nu}{q^2}\right) + \frac{W_2(Q^2,\nu)}{M^2}\left(P^\mu - \frac{P\cdot q}{q^2} q^\mu\right)\left(P^\nu - \frac{P\cdot q}{q^2} q^\nu\right) . \tag{1.16}$$

This leads to the following form of the cross section:

$$\frac{d^2\sigma}{dQ^2 d\nu}(e^- p \to e^- X) = \frac{\pi\alpha^2}{4E_e^{i\,2}\sin^4(\theta/2)} \frac{1}{E^i_e E^f_e} \left[W_2 \cos^2(\theta/2) + 2W_1 \sin^2(\theta/2)\right] . \tag{1.17}$$

In principle, one might expect that the dependence of W_1 and W_2 on the variables Q^2 and ν would be very complicated, reflecting the complexity of the inelastic scattering processes. However, in 1969, Bjorken [36] predicted that in the DIS regime, when Q^2 and ν are infinitely large (compared to the natural scales of the system, such as particle masses), the functions W_1 and W_2 behave in a very simple way: in DIS, these structure functions scale, meaning they become functions not of Q^2 and ν independently but of the ratio Q^2/ν between them. This property is known as "*Bjorken scaling*". Therefore, it is convenient to introduce the following scaling variables:

$$x_B = Q^2/2M_p\nu \, , \tag{1.18}$$

$$y_B = \nu/E^i_e \, . \tag{1.19}$$

Explicitly, the Bjorken scaling tells us that for very large values of Q^2 and ν, but a fixed value for x, we have:

$$\begin{aligned} W_1(Q^2,\nu) &\to F_1(x_B)\,, \\ W_2(Q^2,\nu) &\to F_2(x_B)\,. \end{aligned} \tag{1.20}$$

Introducing the functions $q_i(x)$ that represent the probability density of finding a particular charged parton of type i carrying a momentum fraction x of the total momentum of the proton. By averaging the structure functions, we arrive at the following equations:

$$F_1(x_B) = \sum_i \int dx e_i^2 q_i(x) \frac{1}{2} \delta(x - x_B)\,, \tag{1.21}$$

$$F_2(x_B) = \sum_i \int dx e_i^2 q_i(x) x \delta(x - x_B)\,. \tag{1.22}$$

These q_i functions are the so called Parton Distribution Functions (PDFs). Subsequently, works by Callan, Gross, and Feynman [38, 39] showed that $2xF_1(x_B) = F_2(x_B)$. We should not confuse these functions F_1 and F_2 with the Dirac and Pauli form factors.

One of the most important consequences of Eqs. (1.20) is that, in the DIS regime, the cross-section for the $e^- p \to e^- X$ scattering, Eq. (1.17), does not depend on Q^2. Behavior that only occurs in elastic scattering processes.

The cross-section for DIS behaves akin to elastic scattering at high values of Q^2 and ν. In this high-energy regime, the electron's interaction with the proton undergoes a fundamental change – it no longer treats the proton as a point-like entity but rather interacts with its constituent quarks. These quarks, being elementary and indivisible particles. This insightful interpretation of Bjorken scaling was first articulated by Feynman, who introduced the concept of the electron engaging with the proton's point-like constituents, partons (Feynman's parton model). In the contemporary understanding, we not only recognize quarks but also include gluons in the category of partons.

Feynman's parton model provides compelling evidence for the idea that nucleons consist of point-like, independent particles known as quarks or partons with spin-1/2. Moreover, it offers an explanation for the lack of dependence on Q^2 in the nucleon's scattering structure functions by framing electron-proton scattering as an incoherent

summation of the electron's elastic interactions with quarks. Consequently, the fundamental equation of the parton model is as follows:

$$\sigma_{eh}(p_b, q) = \sum_a \int_0^1 \sigma_{ea}(xp_b, q) f_{a/h}(x)\,. \tag{1.23}$$

Here, we have $\sigma_{eh}(p_b, q)$ as the cross-section for the process $e^-(p_a)+p(p_b) \to e^-(k_a)+X$, and $\sigma_{ea}(xp_b, q)$ as the cross-section for $e^-(p_a) + a(xp_b) \to e^-(k_a) + a(xp_b + q)$, where a represents a parton with a momentum fraction of the hadron h. Additionally, we introduce $f_a(x)$, as the PDFs, which quantifies the probability of finding a parton of type a (whether it's a quark or gluon) within a given hadron, such as the proton. This probability depends on a specific momentum fraction, denoted by x within the range of $[0, 1]$. Notably, these functions are differents for each type of parton, necessitating a summation over all possible partons.

It is important to note that we assume these PDFs to be independent of the specific scattering process. Furthermore, the inelastic hadron cross-section can be expressed as the sum of the convolutions between the elastic parton cross-sections and the parton distribution of the hadron. In the context of quantum mechanics, this summing of probabilities without taking into account the amplitudes represents an incoherence between the scattering at high momenta q and the parton distributions.

In addition, by invoking the parton model, we can describe the tensor $W_X^{\mu\nu}$ associated with the $e^-p \to e^-X$ scattering in the single-photon exchange approximation, as illustrated in the right panel of Figure 1.2, using the following expression:

$$W_X^{\mu\nu}(q, p_b) = \sum_a \int_y^1 \frac{dx}{x} f_a(x, \mu^2) H_a^{\mu\nu}(q, xp, \mu, \alpha_s(\mu)) + \text{corrections}\,. \tag{1.24}$$

In this context, μ defines the factorization scale, and the term referred to as "corrections" takes into consideration processes involving the exchange of two or more photons. We can observe that the PDF is also dependent of the scale. Finally, each tensor coefficient $H_a^{\mu\nu}$ is exclusively associated with the interaction between the photon and the respective parton a.

In 1979, the revelation of asymptotic freedom in strong interactions, along with the discovery of the existence of gluons and other phenomena, has led to the realization

that QCD emerges as the preeminent theory for describing the strong interactions among these elementary particles residing within hadrons.

1.2 Quantum Chromodynamics: general properties

QCD is a renormalizable quantum field theory that exhibits a perturbative and a non-perturbative facet, it governs the strong interactions (one of the four fundamental forces of the universe) between its degrees of freedom, the quarks, and gluons. Unlike QED, the gauge group of QCD is non-abelian. Next, we will see the fundamental properties of QCD:

- **Asymptotic Freedom.** At very high energies (or short distances), quarks and gluons interact very weakly. QCD predicts this behavior, which was discovered by David Politzer, Frank Wilczek and Davis Gross, and thanks to which they won the Nobel Prize in Physics in 2004. The discovery of asymptotic freedom allowed physicists to make more precise predictions using the perturbation theory technique. Evidence for gluons was seen first at PETRA in 1979. These experiments became increasingly precise, culminating in the perturbative verification of QCD at LEP and CERN.

- **Confinement.** Quarks and gluons cannot be seen free in nature at low energies (or long distances), but are observed confined within the hadrons. Quarks and gluons have then three color quantum numbers: red, green, and blue. The physical states correspond to neutral states (without color), being a combination of the colors. Since gluons can interact with each other, they form a color field that prevents the quarks from separating. The potential between quarks grows linearly with distance and, therefore, an infinite amount of energy is required to separate two quarks.

These resolution scale-dependent phenomena are due to the variation of the coupling constant of the strong interaction $\alpha_s(Q^2)$. We can observe in Figure 1.3 that at low energies, $\alpha_s \sim 1$, [40]. However, at high energies we have $\alpha_s(M_Z) \sim 0.118$, where M_z is the Z boson mass.

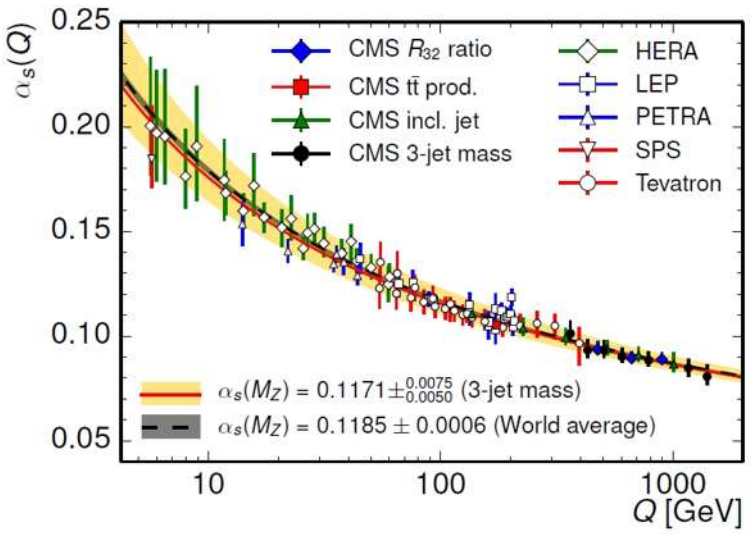

FIGURE 1.3: Strong coupling constant as a function of the energy scale, Q. The figure is taken from [40].

As a consequence of these dynamics, another intriguing phenomenon manifests within this theory: the ***dynamical chiral symmetry breaking*** (DCSB). This phenomenon tell us how quarks and gluons spontaneously acquire mass as the energy scale decreases. A more detailed exploration of this fascinating phenomenon awaits us in Chapter 3.

On the other hand, we can observed that at high energies, the strong coupling becomes small enough to allow us to employ perturbation theory, a crucial phenomenological tool. Within this framework, we can explore QCD dynamics depending on the energy regime we are investigating, distinguishing between *perturbative QCD* (pQCD) and *non-perturbative QCD* (npQCD).

pQCD, associated with the concept of asymptotic freedom, is effective for energy scales beyond the hadron mass. However, beyond this point, where the coupling constant becomes sufficiently large, perturbative techniques become invalid. Consequently, processes involving elementary particles in confinement scales cannot be directly calculated using pQCD.

In contrast, the npQCD regime necessitates the development of specific techniques to investigate quarks within their confined states, as detailed in Chapter 3. Thanks to the Factorization Theorem [41] of QCD, we can separate the scattering cross sections of processes into two distinct components: those calculable at short distances

using perturbation theory and universal functions that characterize long-distance behavior. Examples of these universal functions include the aforementioned EFF, PDFs, as well as the fragmentation functions, generalized parton distributions (GPDs), and parton distribution amplitudes (PDAs). These functions can be extracted through phenomenological adjustments, as we will show in this thesis.

Now because the dynamics of a system can be extracted from the corresponding Lagrangian, in the next section we will focus on the study of the QCD Lagrangian.

1.2.1 QCD lagrangian

The Lagrangian that describes QCD is given by the following elements:

$$\mathcal{L}_{QCD} = \mathcal{L}_{clas} + \mathcal{L}_{g-f} + \mathcal{L}_{ghost}\,. \tag{1.25}$$

In this context, $\mathcal{L}_{clas}$ represents the classical Lagrangian density, characterizing the interaction of quarks with a mass m_0, alongside massless gluons. The subsequent term, $\mathcal{L}_{g-f}$, serves as the factor that establishes the scale, a crucial parameter in defining the gluon propagator. The introduction of this term also necessitates the incorporation of the third term, $\mathcal{L}_{ghost}$, each of which will be described bellow.

- ***Classical lagrangian***. The classical lagrangian density has the form:

$$\mathcal{L}_{clas} = \sum_{j=1}^{N_f} \bar{\psi}_l^j (i\gamma^\mu D_\mu - m_j)\psi_l^j - \frac{1}{4} F^a_{\mu\nu} F_a^{\mu\nu}\,. \tag{1.26}$$

  Quarks are represented by the fermionic field ψ_q^j, where l is the color index, N_f is the number of flavors, and $j = u, d, s, c, b, t$ is the flavor index. Also, $D_\mu = \partial_\mu + ig_s t^a A^a_\mu$ is the covariant derivative, with A^a_μ the corresponding gluon field, g_s the coupling constant of the strong interaction according to $\alpha_s = g_s^2/4\pi$ and t^a are the generators of the $SU_c(3)$ group.

  The second term encompasses the dynamics of the gauge fields (gluons), including their kinetic energy and self-interactions, where $F^a_{\mu\nu}$ is the energy-momentum

tensor of the gluons, defined as ($a = 1, ..., 8$ is the color index):

$$F^a_{\mu\nu} = \partial_\mu A^a_\nu - \partial_\nu A^a_\mu + g_s f_{abc} A^b_\mu A^c_\nu \,. \tag{1.27}$$

In the above expression, the last term is responsible for introducing interactions among the gauge bosons themselves, a characteristic feature of non-abelian theories, i.e., theories described by a non-commutative symmetry group.

Moreover, f_{abc} are the completely antisymmetric structure constants of the gauge group of QCD. We have the following relationships:

$$\begin{aligned} [t^a, t^b] &= i f_{abc} t^c \,, \\ t^a t^a &= C_F I \,, \\ Tr[t^a t^b] &= \frac{1}{2}\delta_{ab} \,, \\ f_{acd} f_{bcd} &= C_A \delta_{ab} \,. \end{aligned} \tag{1.28}$$

In the fundamental representation of $SU_c(3)$: $C_A = 3$, $C_F = 4/3$, $t^a = \lambda^a/2$ where λ^a are the Gell-Man matrices.

- ***Covariant terms***. The second term, $\mathcal{L}_{g-f}$, in the Lagrangian takes the following form:

$$\mathcal{L}_{g-f} = -\frac{1}{2\xi}(\partial^\mu A\mu^a)^2 \,. \tag{1.29}$$

This term is introduced to eliminate redundant degrees of freedom, ensuring the invertibility of the gluon differential operator and well-defined propagators at the tree level. This is achieved by fixing the gauge, with ξ as the gauge-fixing parameter. Specifically, $\xi = 0$ corresponds to the Landau gauge, while $\xi = 1$ corresponds to the Feynman gauge. Fixing the gauge results in the Lagrangian losing its gauge invariance. However, it's important to note that physical observables are inherently independent of the gauge choice and remain gauge-invariant in nature. Therefore, the choice of ξ doesn't impact the final results.

Finally, the third term, denoted as $\mathcal{L}_{ghost}$ in the Lagrangian, takes the following form:

$$\mathcal{L}_{ghost} = -(\partial^\mu \bar{\eta}_a)(\partial_\mu \eta_a) - g_s f_{abc} (\partial_\mu \bar{\eta}_a) A^\mu_b \eta_c \,. \tag{1.30}$$

These fields, represented by η_a, correspond to the Faddeev-Popov ghost fields. In the context of non-abelian QCD, their inclusion becomes necessary when introducing the gauge term. These ghost fields don't represent physical particles; instead, they manifest as virtual entities in Feynman diagrams. Nevertheless, they play a crucial role in calculations involving arbitrary covariant gauges. The specific characteristics of these ghost fields may vary depending on the chosen gauge standard.

Therefore, the complete QCD Lagrangian Eq. (1.25) corresponds to

$$\mathcal{L}_{QCD} = \sum_{j=1}^{N_f} \bar{\psi}_l^j (i\gamma^\mu D_\mu - m_j)\psi_l^j - \frac{1}{4} F_{\mu\nu}^a F_a^{\mu\nu} - \frac{1}{2\xi}(\partial^\mu A\mu^a)^2 - (\partial^\mu \bar{\eta}_a)(\partial_\mu \eta_a) - g_s f_{abc}(\partial_\mu \bar{\eta}_a) A_b^\mu \eta_c \,. \tag{1.31}$$

Quantum Field Theories (QFTs) are one of the most significant theoretical concepts of the past century because they successfully combine two central theories of modern physics: special relativity and quantum mechanics. Among these QFTs are the so-called "gauge theories", which have proven to be highly successful in describing fundamental phenomena. In fact, the Standard Model (SM) is based on this type of theory.

Gauge theories are founded on the well-known "gauge principle", which states that interactions between fundamental particles are obtained by imposing that the system's Lagrangian remains invariant under a certain group of symmetry. This symmetry must be local and continuous, and it is referred to as "gauge symmetry".

The gauge symmetry corresponding to the SM is $SU_C(3) \times SU_L(2) \times U_Y(1)$. The $SU_L(2) \times U_Y(1)$ gauge group describes the electroweak sector, unifying electromagnetic and weak interactions, while $SU_C(3)$ is the fundamental symmetry of Quantum Chromodynamics (QCD). We will now explore some QCD symmetries.

1.2.2 flavor and baryon number symmetries

- ***Baryon number symmetry***.

  First, corresponding to the symmetry of the baryon number, we have the global $U(1)$ symmetry, where a field transformation $\psi(x) \to e^{i\theta}\psi(x)$ results in a baryonic current $J_B^\mu(x) = \bar{\psi}(x)\gamma^\mu\psi(x)$.

The conserved charge, denoted as B, is defined as the integral of the density $B = \int d^3x\psi^\dagger(x)\psi(x)$ and corresponds to the baryon number.

- ***Flavor symmetry***. We start with a state represented as $\psi(x) = (u\, d)^T$. When we consider isospin symmetry, it means that we assume the masses of the up and down quarks, denoted as m_u and m_d, are equal. To account for this symmetry, the flavor transformation of $SU(2)$ is as follows:

$$\psi(x) \to \psi'(x) = e^{i\frac{\tau^a}{2}\theta_a}\,. \tag{1.32}$$

Here, $\tau_a/2$ (with $a = 1, 2, 3$) represents the $SU(2)$ generators, the well-known Pauli matrices.

Within this framework, we define conserved currents as

$$\bar{V}_a^\mu(x) = \psi(x)\gamma^\mu\frac{\tau_a}{2}\psi(x)\,, \tag{1.33}$$

and the conserved charge Q_V is expressed as the integral of the density

$$Q_V = \int dx, \bar{V}_a^\mu(x)\,. \tag{1.34}$$

It's important to note that this description can be extended to situations where there are three different flavors of quarks ($N_f = 3$). In this extension, we include the strange quark component within the $\psi(x)$ representation, and we assume that the masses of the up, down, and strange quarks are all equal ($m_u = m_d = m_s$). In this case, we replace the Pauli matrices τ_a with the Gell-Mann matrices λ_a (where $a = 1, \ldots, 8$).

1.2.3 Gauge symmetry

We will elucidate how the imposition of gauge invariance under $SU_C(3)$ within the Lagrangian that characterizes quarks leads to the introduction of interactions among them.

Starting with a Lagrangian of spin-1/2 fermions, the Dirac Lagrangian:

$$\mathcal{L}_{Dirac}(x) = \bar{\psi}_l^j(x)\left(i\partial\!\!\!/ - m_j\right)\psi_l^j(x), \tag{1.35}$$

where $\not{\partial} \equiv \gamma^\mu \partial\mu$, and m_j represents the quark mass. Quarks are represented by the fermionic field $\psi_l^j(x)$ as we already mentioned, the sum over the indices is implicit. To introduce interactions among quarks, we need to ensure that this Lagrangian is invariant under gauge transformations related to $SU_C(3)$. For fermionic fields, gauge transformation is as follows:

$$\psi_q(x) \to \psi'_q(x) = e^{it^a\theta^a(x)}\psi_q(x)\,,$$

with $\theta_a(x)$ as scalar functions, and t^a as the generators of the $SU_C(3)$ group as regularly.

To maintain gauge invariance, we promote the partial derivative ∂_μ to the covariant derivative $D_\mu = \partial_\mu + ig_s t^a A^a_\mu$.

where we have introduce the spin-1 gauge fields, A^a_μ corresponging to gluons. The gauge transformation for A^a_μ is given by:

$$A^a_\mu \to A'^a_\mu = A^a_\mu - \partial_\mu\theta^a(x) - g_s f^{abc}\theta^b(x)A^c_\mu(x)\,, \tag{1.36}$$

f^{abc} is the already mentioned tructure constants. With these rules, the Dirac Lagrangian is redefined as:

$$\mathcal{L}_{Dirac}(x) \to \mathcal{L}_{\mathcal{I}}(x) = \bar{\psi}(x)\left(i\gamma^\mu D\mu - m\right)\psi(x)\,. \tag{1.37}$$

To identify the fields A^a_μ as physical particles (gluons), we introduce kinetic and potential energy terms. This requires adding a kinetic energy term to the Lagrangian as follows:

$$\mathcal{L}_{\mathcal{I}}(x) \to \mathcal{L}_{\mathcal{QCD}}(x) = \mathcal{L}_{\mathcal{I}}(x) - \frac{1}{4}F^a_{\mu\nu}F^{\mu\nu}_a\,, \tag{1.38}$$

where $F^a_{\mu\nu}$ is the energy-momentum tensor of gluons Eq. (1.27). Until now, the QCD Lagrangian is then expressed as:

$$\mathcal{L}_{\mathcal{QCD}}(x) = \sum_{j=1}^{N_f}\bar{\psi}^j_l(i\gamma^\mu D_\mu - m_j)\psi^j_l - \frac{1}{4}F^a_{\mu\nu}F^{\mu\nu}_a\,. \tag{1.39}$$

This Lagrangian corresponds to the classical Lagrangian.

Now, in order to eliminate unnecessary degrees of freedom within the gauge fields, we need to impose constraints on these fields. One such constraint involves setting the covariant gauge condition, typically referred to as the Lorentz gauge:

$$G(A) = \partial^\mu A_\mu = 0\,. \tag{1.40}$$

To incorporate this constraint, we introduce a term $\lambda(\partial^\mu A^a_\mu)^2$ where $\lambda = -1/(2\xi)$ which acts as a Lagrange multiplier, a parameter that we can adjust. When we add this term to the Eq. (1.39), it yields the following Lagrangian:

$$\mathcal{L}_{QCD} = \sum_{j=1}^{N_f} \bar{\psi}^j_l (i\gamma^\mu D_\mu - m_j)\psi^j_l - \frac{1}{4}F^a_{\mu\nu}F^{\mu\nu}_a - \frac{1}{2\xi}(\partial^\mu A\mu^a)^2\,. \tag{1.41}$$

It is important to note that, for quantization purposes, the introduction of ghosts are necessary to ensure unitarity. However, these aspects go beyond the scope of this thesis.

1.2.4 Chiral symmetry and its spontaneous violation

Chiral symmetry in QCD, is manifested when quark masses become exceedingly small. While quarks possess current masses (the mass of free quarks), we observed that it is substantially smaller than that of hadrons. This observation hints at an intriguing phenomenon – an approximate chiral symmetry, where $m_u \approx m_d \approx 0$. Allowing us to treat chiral symmetry as an approximation within strong interactions.

This symmetry is closely tied to the vector-axial current, which, when spontaneously broken, results in what we call *spontaneous chiral symmetry breaking*. This process dynamically generates masses for the particles involved.

A significant implication of this symmetry breaking is the presence of the Goldstone boson. In QCD, the Goldstone boson is the pion, which, according to this symmetry breaking, should ideally possess zero mass. The slight mass exhibited by pions arises from explicit chiral symmetry breaking, caused by the non-zero mass of free quarks.

For a more detailed perspective, let's examine a Lagrangian for two massless fermion flavors, a model that can be readily applied to QCD. We begin with the Dirac Lagrangian for m=0, which reads as follows:

$$\mathcal{L} = i\bar{\psi}^j \not{\partial} \psi^j \,. \tag{1.42}$$

Where the subscript j can represent u or d quarks. Now, let's consider the following transformation:

$$\psi_j \longrightarrow e^{-i\frac{\boldsymbol{\tau}}{2}\cdot\boldsymbol{\theta}}\psi^j \simeq \left(1 - i\frac{\boldsymbol{\tau}}{2}\cdot\boldsymbol{\theta}\right)\psi^j \,. \tag{1.43}$$

Here, $\vec{\tau}$ represents the Pauli matrices for isospin. The conjugate field transforms as:

$$\bar{\psi}^j \longrightarrow \bar{\psi}^j e^{i\frac{\boldsymbol{\tau}}{2}\cdot\boldsymbol{\theta}} \simeq \bar{\psi}^j \left(1 + i\frac{\boldsymbol{\tau}}{2}\cdot\boldsymbol{\theta}\right) \,. \tag{1.44}$$

It is evident that the Lagrangian (1.42) remains invariant under transformation (1.43):

$$\begin{aligned}\mathcal{L} = i\bar{\psi}^j \not{\partial}, \psi^j \longrightarrow \mathcal{L}' &= i\bar{\psi}^j \not{\partial}, \psi^j - i\boldsymbol{\theta}\cdot\left(i\bar{\psi}^j \not{\partial}\frac{\boldsymbol{\tau}}{2}\psi^j - i\bar{\psi}^j\frac{\boldsymbol{\tau}}{2}\not{\partial}\psi^j\right) \\ &= i\bar{\psi}^j \not{\partial}\psi^j \,.\end{aligned} \tag{1.45}$$

Thus, the associated conserved current is:

$$V^a_\mu = \bar{\psi}^j \gamma_\mu \frac{\tau^a}{2}\psi^j \,, \tag{1.46}$$

which is known as the vector current. Considering the following transformation:

$$\psi^j \longrightarrow e^{-i\gamma_5\frac{\boldsymbol{\tau}}{2}\cdot\boldsymbol{\theta}}\psi^j = \left(1 - i\gamma_5\frac{\boldsymbol{\tau}}{2}\cdot\boldsymbol{\theta}\right)\psi^j \,, \tag{1.47}$$

and, taking into account the gamma matrix anticommutation relationships, particularly $\gamma_0\gamma_5 = -\gamma_5\gamma_0$, it is evident that the Lagrangian pf Eq. (1.42) also remains invariant under transformation of Eq. (1.47):

$$\begin{aligned}\mathcal{L} = i\bar{\psi}^j \not{\partial}, \psi^j \longrightarrow \mathcal{L}' &= i\bar{\psi}^j \not{\partial}, \psi^j - i\boldsymbol{\theta}\cdot\left(i\bar{\psi}j\not{\partial}\gamma\mu\gamma_5\frac{\tau^a}{2}\psi^j - i\bar{\psi}^j\gamma_5\frac{\boldsymbol{\tau}}{2}\not{\partial}\gamma\mu\psi^j\right) \\ &= i\bar{\psi}_j \not{\partial}\psi^j \,.\end{aligned} \tag{1.48}$$

This results in the associated current:

$$A^a_\mu = \bar{\psi}^j \gamma\mu\gamma_5 \frac{\tau^a}{2} \psi^j \,. \tag{1.49}$$

Known as the vector-axial current. We can see that the Lagrangian for two massless fermions in QCD remains invariant under both transformations, forming the so-called chiral symmetry. However, when we introduce a mass term in the Lagrangian:

$$\delta\mathcal{L} = -m\bar{\psi}^j\psi^j \,. \tag{1.50}$$

It becomes clear that this term is invariant under transformation of Eq. (1.43) but not under transformation of Eq. (1.47). In particular, under transformation in Eq. (1.47), this term transforms as:

$$\delta\mathcal{L} = -m\bar{\psi}^j\psi^j \longrightarrow -m\bar{\psi}^j\psi^j + 2im\boldsymbol{\theta}\left(\bar{\psi}^j \frac{\tau^a}{2}\gamma_5\psi^j\right) \,. \tag{1.51}$$

This reveals a symmetry breaking for quarks due to their current mass. Since this mass is considerably small, we can treat it as an approximate symmetry. However, this is why we observe a dynamic generation of masses as energy decreases, transitioning from perturbative to non-perturbative regimes. This process is explored in more detail in Chapter 3 within the Schwinger-Dyson Equations approach.

Chapter 2

Hadronic structure

2.1 Electromagnetic Form Factor

Studying the nuclear structure of hadrons through an electromagnetic processes is one of the cleanest approaches available, as opposed to using alpha particles, which Rutherford famously employed to discover the atomic nucleus. Regarding the previous Chapter, if we consider the scenario of an elastic scattering between an electron and a composite particle, such as the proton ($e^- p \to e^- p$), which is depicted in the left panel of Figure 1.2, we would have that the electron interacts electromagnetically with the proton through the exchange of a photon. Also, by increasing the energy or frequency of this photon, it can probe the internal quark structure of the proton. Additionally, the quarks within the proton interact strongly with each other through the exchange of particles called gluons. This strong coupling between quarks and gluons at low energies makes these interactions non-perturbative. As a result, describing electron-proton scattering requires the introduction of the electromagnetic form factors. These form factors provide a way to encapsulate the non-perturbative nature of the strong interactions within the proton and help us understand its charge density. Furthermore, these form factors are experimentally accessible quantities.

To simplify and illustrate the concept, we can focus on a specific example involving spin-0 targets like pseudoscalar mesons, such as the pion. In the case of the elastic scattering between an electron and a pion ($e^- \pi^+(\pi^-) \to e^- \pi^+(\pi^-)$), we can visualize a diagram similar to the one of the left shown in Figure 1.2, where the circle represents

all potential interactions between the photon and the fundamental components of the pion.

Now, when considering a Coulomb scattering process, if the potential $V^0(\mathbf{r})$ arises from a charge density $\rho(\mathbf{r})$, then $V^0(\mathbf{r})$ must satisfy the Poisson equation:

$$\nabla^2 V^0(\mathbf{r}) = -Ze\rho(\mathbf{r})\,. \tag{2.1}$$

Here, Z represents the charge, and e is the elementary charge. In a special case where the charge density is concentrated at a single point ($\rho(\mathbf{r}) = \delta(\mathbf{r})$), the potential $V^0(\mathbf{r})$ reduces to the familiar form for a point charge: $V^0(\mathbf{r}) = Ze/4\pi|\mathbf{r}|$. To characterize this potential mathematically, we calculate its Fourier transform:

$$\tilde{V}^0(\mathbf{q}) = \int e^{i\mathbf{q}\cdot\mathbf{r}} V^0(\mathbf{r}) d^3\mathbf{r}\,. \tag{2.2}$$

Here, $\mathbf{q}$ represents the momentum transfer, and $\tilde{V}^0(\mathbf{q})$ is the Fourier-transformed potential. By applying the definition of $V^0(\mathbf{r})$, we derive the following relation:

$$\int e^{i\mathbf{q}\cdot\mathbf{r}} \nabla^2 V^0(\mathbf{r}) = -Ze \int e^{i\mathbf{q}\cdot\mathbf{r}} \rho(\mathbf{r}) d^3\mathbf{r} \equiv -ZeF(\mathbf{q})\,. \tag{2.3}$$

In this equation, the function $F(\mathbf{q})$ emerges as the static form factor, encapsulating the charge distribution's Fourier components. It's crucial to note that $F(\mathbf{q})$ satisfies the normalization condition $F(0) = 1$, signifying that the total charge is Ze.

Additionally, it is worth noting that:

$$\int \left(\nabla^2 e^{i\mathbf{q}\cdot\mathbf{r}}\right) V^0(\mathbf{r}) = -q^2 \int e^{i\mathbf{q}\cdot\mathbf{r}} V^0(\mathbf{r}) d^3\mathbf{r}\,. \tag{2.4}$$

As a result, when we employ the outcomes of Eqs. (2.2), (2.3), and (2.4), we obtain:

$$\tilde{V}^0(\mathbf{q}) = \frac{F(\mathbf{q})}{\mathbf{q}^2} Ze\,. \tag{2.5}$$

Consequently, we observe that, at the lowest order in perturbation theory, the transition element matrix is determined by the point-like amplitude, multiplied by the form factor $F(\mathbf{q})$. In this straightforward scenario, the form factor interprets as the Fourier transform of the charge distribution.

In the absence of a comprehensive theory, we turn to the principles of Lorentz invariance and the electromagnetic current conservation to restrict the general structure of the pion-pion-photon vertex. This approach allows us to derive a generalized static form factor for the real pion. To begin, considering Lorentz invariance, the electromagnetic vertex of a pion assumes the following form:

$$j^{\mu}_{\pi^+}(p,p') = \langle \pi^+, p' | j^{\mu}_{em,\pi}(0) | \pi^+, p \rangle = e\left[F(q^2)(p'+p)^{\mu} + G(q^2)q^{\mu}\right] . \tag{2.6}$$

The functions $F(q^2)$ and $G(q^2)$ represent the form factors. To derive these, we started by considering the condition $p' = p + q$, where $p^2 = p'^2 = M_{\pi}^2$, leading to $q^2 = 2M_{\pi}^2 - 2p \cdot p'$, being p and p' the corresponding initial and final moments of the pion.

Now, in order to determine the pion's form factor, we must adhere to our second principle, the conservation of electromagnetic current. In other words, we need to satisfy the current conservation condition:

$$q_{\mu} \langle \pi^+(p') | \hat{j}^{\mu}_{em,\pi}(0) | \pi^+(p) \rangle = 0 \, . \tag{2.7}$$

Combining the above equation with Eq. (2.6), we arrive at the following condition:

$$q_{\mu}\left[F(q^2)(p'+p)^{\mu} + G(q^2)q^{\mu}\right] = 0 \, . \tag{2.8}$$

The first term $(q \cdot (p'+p))$ is zero, as it signifies the electromagnetic current conservation condition for the vertex of a point-like particle. However, for the second term, we have $q^2 \neq 0$, implying that current conservation dictates that $G(q^2) = 0$.

In simpler terms, all the virtual effects of strong interaction in the pion-pion-photon vertex can be encapsulated by a Lorentz scalar function. Consequently, the pion's electromagnetic vertex can be expressed as:

$$j^{\mu}_{\pi^+}(p,p') = eF(q^2)(p'+p)^{\mu} \, . \tag{2.9}$$

Thus, a spin-0 particle such as the pion possesses a single electromagnetic form factor, denoted as $F(q^2)$, which extends the concept of the static form factor seen earlier. This form factor retains the normalization condition $F(0) = 1$.

Furthermore, we can observe that the invariant amplitude in Eq. (1.1) for $e^-(k) + \pi^+(p) \to e^-(k') + \pi^+(p')$ can be derived by simply substituting $j^{\mu}_{p}(p_b, k_b)$ with $j^{\mu}_{pi^+}(p,p')$,

along with the respective momenta for the electron. This implies that when q^2 is relatively small, the amplitude remains largely unchanged, reflecting the conservation of the initial state. As q^2 increases, we expect the amplitude for an inelastic process, involving the production of additional particles, will increase, while the amplitude for an elastic process correspondingly decreases.

Moreover, the form factor allows us to determine the charge radius of a particle, which will be explored next.

2.1.1 Charge radius

Recalling the expression:

$$F(q^2) = \int \rho(\mathbf{r}) e^{i\mathbf{q}\cdot\mathbf{r}} d^3\mathbf{r}\,, \tag{2.10}$$

where $d^3\mathbf{r} = d\phi \sin\theta d\theta r^2 dr$, the form factor for a radial charge density will be:

$$\begin{aligned} F(q^2) &= \int_0^{2\pi} d\phi \int_0^{\pi} \sin\theta d\theta \int_0^{\infty} r^2 \rho(r) e^{i\mathbf{q}\cdot\mathbf{r}} dr \\ &= 2\pi \int_0^{\infty} r^2 \rho(r) dr \int_{-1}^{1} d\cos\theta e^{iqr\cos\theta} \\ &= 2\pi \int_0^{\infty} r\rho(r) \left[\frac{e^{iqr} - e^{-iqr}}{iq}\right] dr \\ &= \frac{4\pi}{q} \int_0^{\infty} r\rho(r) \sin(qr) dr\,. \end{aligned} \tag{2.11}$$

Working in the limit of small momentum transfer, we can expand in $\sin(qr)$. From the equation above, we have:

$$\begin{aligned} F(q^2) &= \frac{4\pi}{q} \int_0^{\infty} r\rho(r) \left[qr - \frac{1}{3!}(qr)^3 + ...\right] dr \\ &= \int_0^{\infty} \rho(r) d^3r - \frac{q^2}{6} \int_0^{\infty} r^2 \rho(r) d^3r + \mathcal{O}(q^4) \\ &= 1 - \frac{q^2}{6} \int_0^{\infty} \psi^* r^2 \psi d^3r + \mathcal{O}(q^4) \\ &= 1 - \frac{q^2}{6} \langle r^2 \rangle + \mathcal{O}(q^4)\,, \end{aligned} \tag{2.12}$$

where $\rho(r) = \psi^*\psi$ is the probability density. This expression leads to:

$$\langle r^2 \rangle = -6 \left. \frac{dF(q^2)}{dq^2} \right|_{q^2=0} . \tag{2.13}$$

Being $\langle r^2 \rangle$ the charge radius of the hadron that corresponds to its charge density.

2.2 Parton Distribution Functions

PDFs are another fundamental quantity in the framework of non-perturbative QCD. They provide crucial insight into the internal structure of hadrons, offering a probabilistic description of how the momentum of a hadron is distributed among its constituent partons as a function of momentum fraction and energy scale.

For example, lets consider a simplified model without QCD interactions, nucleons (protons and neutrons) are viewed as composed of point-like, free spin-1/2 partons within the quark model. Gluons, although present, do not directly interact with photons; instead, photons-gluons interaction only occurs through the virtual quark-antiquark ($q\bar{q}$) pairs coupled to the gluons constituents. This creates a sea of $q\bar{q}$ partons within the nucleon. We can represent the probability distributions for the quarks $u, \bar{u}, d, \bar{d}, s, \bar{s}$, etc., as $u(x), \bar{u}(x), d(x), \bar{d}(x), s(x), \bar{s}(x)$, etc., with momentum fraction x in the proton. And, within the parton model, the proton structure functions have the following simple form in terms of parton distribution:

$$F_2^{ep}(x)/x = 2F_1^{ep}(x) = \frac{4}{9}[u(x) + \bar{u}(x)] + \frac{1}{9}[d(x) + \bar{d}(x)] + \frac{1}{9}[s(x) + \bar{s}(x)] + \dots . \tag{2.14}$$

Using isospin symmetry, we can relate the up- and down-quark distributions in a neutron to those in a proton:

$$u^n(x) = d^p(x) \equiv d(x) \;\; ; d^n(x) = u^p(x) \equiv u(x) \, . \tag{2.15}$$

This connection enables us to obtain separate information of the individual PDFs by combining data from different DIS processes.

Quark distributions must adhere to specific rules. For instance, both protons and neutrons having zero strangeness leads to the constraint:

$$\int_0^1 dx[s(x) - \bar{s}(x)] = 0\,. \tag{2.16}$$

Similar rules apply to heavier flavors. Furthermore, the electric charges of protons and neutrons result in two additional sum rules:

$$\int_0^1 dx[u(x) - \bar{u}(x)] = 2\,, \int_0^1 dx[d(x) - \bar{d}(x)] = 1\,. \tag{2.17}$$

These sum rules reflect the excess of up and down quarks over their respective anti-quarks.

Valence and sea contributions provide insight into nucleon structure. The remaining parton distributions are regarded as pure sea, simplifying the number of independent distributions, such as:

$$\begin{aligned} u(x) &= u_v(x) + q_s(x)\,, \\ d(x) &= d_v(x) + q_s(x)\,, \\ \bar{u}(x) &= \bar{d}(x) = s(x) = \bar{s}(x) = \ldots = q_s(x)\,. \end{aligned} \tag{2.18}$$

This model automatically satisfies the strangeness constraint while implicating constraints primarily on valence-quark distributions.

In a related scenario of quasi-elastic electron-deuterium scattering, we observe a pronounced peak in the structure function at $x = 1/2$. This outcome aligns with expectations since the deuteron, composed of two nucleon constituents, shares total momentum equally, with $M_N \approx 2M_d$ (N= p or n). In a simplistic three-quark model for nucleons, one would anticipate a similar peak at $x = \frac{1}{3}$ in both proton and neutron structure functions. However, the distribution does not show such behavior. Therefore, the deviation can be readily attributed to contributions from parton-sea. By contrasting the proton and neutron structure functions and canceling out the sea's influence, the data indeed reveals a broad peak at $x = \frac{1}{3}$.

This observation is in accordance with our isospin symmetric parton model and underlines the presence of the so-called Gottfried sum rule:

$$\int_0^1 \frac{dx}{x}[F_2^{ep}(x) - F_2^{en}(x)] = \frac{1}{3}\int_0^1 dx[u_v(x) - d_v(x)] = \frac{1}{3}\,. \tag{2.19}$$

Another interesting parameter is the ratio:

$$\frac{F_2^{en}(x)}{F_2^{ep}(x)} = \frac{4d_v(x) + u_v(x) + \sum_{sea}}{4u_v(x) + d_v(x) + \sum_{sea}}\,, \tag{2.20}$$

where $\sum_{sea}$ is the total sea contribution. This ratio should satisfy specific the bounds $\frac{1}{4} \leq F_2^{en}(x)/F_2^{ep}(x) \geq 4$, consistent with data, and tends to 1 at small x, suggesting that sea contributions dominate in that region.

The conservation of total proton momentum leads to the essential sum rule:

$$\int_0^1 dxx[u(x) + \bar{u}(x) + d(x) + \bar{d}(x) + s(x) + \bar{s}(x) + \dots] = 1 - \epsilon\,, \tag{2.21}$$

where ϵ is the fraction of momentum that is not carried by quarks. Empirical evidence suggests that $\epsilon \approx 1/2$ (at $Q^2 \sim 10 - 40GeV^2$), indicating that roughly half of the momentum is carried by gluons. This underscores the pivotal role of gluons in shaping proton structure, highlighting the limitations of the naive quark model, particularly at large Q^2.

Additionally, PDFs themselves cannot be directly measured but are determined through a combination of experimental data and theoretical calculations. Global fits to experimental data with DIS experiments, are used to extract PDFs at various energy scales, providing essential information.

2.2.1 Evolution equations

One of the most remarkable predictions of the quark-parton model is that the structure functions exhibit scaling behavior as $W_i(x, Q^2) \to F_i(x)$ in the Bjorken limit, where Q^2, and ν tend toward infinity while keeping x fixed, Eq. (1.18). This property is based on the assumption that partons' transverse momentum in the proton's infinite-momentum frame is small. However, in QCD, the emission of hard gluons from quarks violates this

assumption, resulting in logarithmic scaling violations, particularly at low values of x. This emission of gluons leads to the evolution of structure functions. As Q^2 increases, more gluons are emitted, subsequently splitting into $q\bar{q}$ pairs. This process leads to a softening of the initial quark momentum distributions and an increase in both the gluon density and the $q\bar{q}$ sea as x decreases. In the framework of QCD, this process is explained through scale-dependent parton distributions $f_a(x, \mu^2)$, where a represents either gluons (g) or quarks (q) and, μ is the scale associated with the probe Q^2.

This evolution in μ is described then by the DGLAP equations [42] which have the schematic form:

$$\begin{aligned} \frac{\partial q^{NS}}{\partial ln\mu^2} &= \frac{\alpha_s(\mu^2)}{2\pi} P_{qq} \otimes q^{NS} \,, \\ \frac{\partial}{\partial ln\mu^2} \begin{pmatrix} q^S \\ g \end{pmatrix} &= \frac{\alpha_s(\mu^2)}{2\pi} \begin{pmatrix} P_{qq} & 2N_f P_{qg} \\ P_{gq} & P_{gg} \end{pmatrix} \otimes \begin{pmatrix} q^S \\ g \end{pmatrix} \,, \end{aligned} \tag{2.22}$$

where $\otimes$ denotes a convolution operation:

$$C \otimes f = \int_x^1 \frac{dy}{y} C(y) f\left(\frac{x}{y}\right) \,, \tag{2.23}$$

also, P_{ab} describes the probability of a given parton splitting into two others. N_f is the number of active quark flavors, g represent the gluon distribution, meanwhile $q^{NS} = q_i - \bar{q}_i$ and $q^S = \sum(q_i + \bar{q}_i)$ represents the non-singlet and singlet quarks distributions respectively. The leading-order Altarelli-Parisi splitting functions [43] are as follows:

$$\begin{aligned} P_{qq} &= \frac{4}{3}\left[\frac{1+x^2}{1-x}_+\right] + 2\delta(1-x) \,, \\ P_{qg} &= \frac{1}{2}\left[x^2 + (1-x)^2\right] \,, \\ P_{gq} &= \frac{4}{3}\left[\frac{1+(1-x)^2}{x}\right] \,, \\ P_{gg} &= 6\left[\frac{1-x}{x} + x(1-x) + \frac{x}{(1-x)_+}\right] \,. \end{aligned} \tag{2.24}$$

Finally, the notation $[H(x)]_+$ defines a distribution in such a way that for any sufficiently regular test function $h(x)$: $h(x)[H(x)]_+ = (h(x) - h(1))H(x)$.

In these DGLAP equations, the initial PDFs cannot be predicted at a specific μ_0 beforehand. Thus, they must be measured at an initial scale μ_0 before QCD predictions can be compared to data at different scales μ. In general, all observables involving a hard hadronic interaction (such as structure functions) can be expressed as a convolution of calculable, process-dependent coefficient functions and these universal parton distributions.

2.3 Generalized Distribution Functions

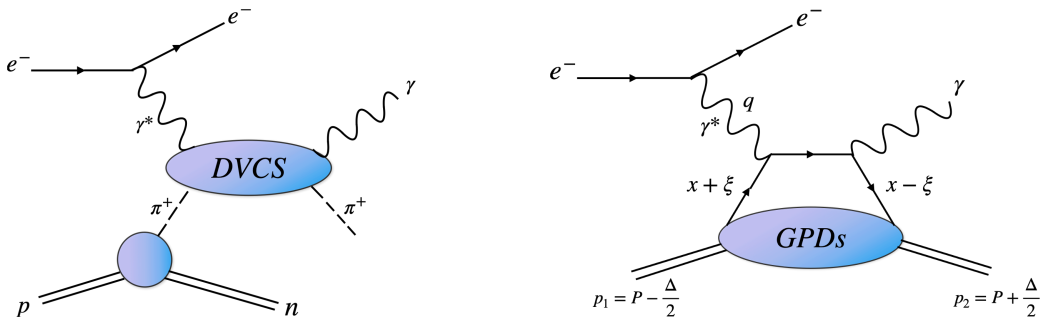

FIGURE 2.1: Left panel- Deeply virtual Compton scattering process of pion. Right panel- Quark GPD contibution to the DVCS.

The generalized parton distributions (GPDs) have emerged as a comprehensive tool to describe a three-dimensional image hadron structure probed in hard scattering processes [44–51]. These GPDs establish a connection between the electromagnetic form factors (EFFs) of hadrons, measured in elastic processes, and the longitudinal PDFs, which are probed in DIS experiments. In other words, GPDs provide a kaleidoscopic view of the 3D spatial structure of hadrons being a generalization of the EFFs and the PDFs. According to this, they are expressed as functions of the longitudinal momentum fraction x, the momentum transfer t, and the skewness variable ξ (representing longitudinal momentum transfer).

Experimental measurements of GPDs are achievable through processes like deeply virtual Compton scattering (DVCS), in which an electron scatters off a proton that carries a momentum p. This interaction results in the production of a photon in the final state in addition to a nucleon with momentum p', where $-t = \Delta^2 = (p - p')^2$. An example of a pion DVCS is illustrated in the Figure 2.1.

GPDs are determined through the Fourier transformation of nonlocal matrix elements associated with hadrons. In the context of this thesis, our primary emphasis will be on pseudoscalar mesons, then in this case, the corresponding quark GPD is as follows [48]:

$$H_M^q(x,\xi,t) = \int \frac{d\lambda}{2\pi} e^{ix\lambda} \langle p|\bar{\psi}^q\left(-\frac{\lambda n}{2}\right) \not{n} \psi^q\left(\frac{\lambda n}{2}\right)|p'\rangle\,, \tag{2.25}$$

where n is a light-like four-vector, such that $n^2 = 0$, and $n \cdot P = -m_M$ with $P = (p+p')/2$, and $p\,(p')$ the initial (final) meson momentum.

Lightfront quantization is a valuable method that enables us to represent any state of hadrons with a specific momentum using a Fock basis composed of N-particle partonic states. These states are characterized by lightfront wave functions (LFWFs), which encompass all the crucial nonperturbative aspects (we will delve deeper into these functions in Chapter 4). As a result, it becomes practical to describe GPDs in terms of these LFWFs. However, it is important to recognize that the partonic framework and the connection between GPDs and LFWFs may exhibit variations depending on the specific kinematic conditions.

In the DGLAP region, when $|x| > \xi$, the GPD can be seen as an overlap of LFWFs, particularly focusing on the same number of constituents. To illustrate, studying pseudoscalar mesons and just considering the valence contribution (i.e., the two-particle Fock state), in the DGLAP region, we can describe the GPD using the so-called overlap representation [48], namely:

$$\begin{aligned} H_{\rm M}^q(x,\xi,t) &= \int \frac{d^2k_\perp}{16\pi^3} \psi_{\rm M}^{q*}\left(x^-,(\mathbf{k}_\perp^-)^2\right)\psi_{\rm M}^q\left(x^+,(\mathbf{k}_\perp^+)^2\right)\,, \\ x^\pm &= \frac{x\pm\xi}{1\pm\xi} \quad , \quad \mathbf{k}_\perp^\pm = k_\perp \mp \frac{\Delta_\perp}{2}\frac{1-x}{1\pm\xi}\,. \end{aligned} \tag{2.26}$$

The momentum transfer is defined by $-t = \Delta^2 = (p-p')^2$; $\Delta_\perp^2 = \Delta^2(1-\xi^2) - 4\xi^2 m_{\rm M}^2$. In addition, the longitudinal momentum fraction transfer is $\xi = [-n\cdot\Delta]/[2n\cdot P]$. Both x and ξ have support on $[-1,1]$. The kinematical completion (the extension to the ERBL domain), required to fulfill the polinomiality property [48], can be achieved through the covariant extension from Refs. [52–55]. Notwithstanding, the GPD is even in ξ and only non-zero for the valence quark if $x > -\xi$ (the antiquark GPD is non-zero if $x < \xi$); hence, in this thesis, we shall restrain ourselves to $\xi \geq 0$. Notice again that Eq. (2.26) implies that the meson is described as a two-body Fock state. This

picture is then valid at the hadronic scale, in which the fully dressed quark/antiquark quasiparticles encode all the properties of the meson.

In the scenario where we approach the forward limit, with $\xi = 0$ and $t = 0$, x transforms into the Bjorken-x, leading to the simplification of the GPD into a PDF:

$$q_M(x) = H^q_M(x, 0, 0)\,. \tag{2.27}$$

For the corresponding antiquark, $\bar{h}_M$, at the hadronic sacale:

$$\bar{h}_M = q_M(1 - x)\,. \tag{2.28}$$

Furthermore, regardless of the specific value of ξ the computation of the electromagnetic pion form factor is achievable through:

$$F^q_{\mathrm{M}}(t) = \int_{-1}^{1} dx\; H^q_{\mathrm{M}}(x, \xi, t)\,. \tag{2.29}$$

We well delve into the extraction of this functions in the chapter 4.

2.4 Parton Distribution Amplitude

The Parton distribution amplitudes (PDAs) are analogous to wave functions in momentum space in the context of quantum mechanics, including all the properties demanded by a QFT. These functions enable us to study the moment distribution for dressed valence quarks within a hadron. PDAs are described in the light-cone formalism, where the eigenfunctions of the Hamiltonian are independent of the system's four-momentum.

The explicit definition of a PDA can be understood as a probability distribution for finding a valence quark-antiquark pair with momentum fractions x and $1 - x$, respectively, forming a bound state. Mathematically, this distribution is defined as the projection of the Bethe-Salpeter wave function, $\chi_M(k, P)$ (we will further explore this equation in Chapter 3), onto the light-cone. In the context of a pseudoscalar meson, the expression takes the form:

$$f_M \phi_M(x) = Tr_{CD} \int_{dk} \delta(n \cdot k - x n \cdot P) \gamma_5 \gamma \cdot n \chi_M(k, P)\,. \tag{2.30}$$

Here, f_M is the meson's decay constant, $\phi(x)$ corresponds to the PDA, and P is the total momentum of the meson such that $P^2 = -m_M^2$ (with m_M being the meson's mass). n is the light-front four-vector, satisfying $n^2 = 0$ and $n \cdot P = -m_M$. Lastly, $\int_{dk}$ represents a Poincaré-invariant four-dimensional integral.

Independent of the valence quarks constitution, in the asymptotic limit, when the scale $\mu \to \infty$, the PDA takes the form:

$$\phi^{CL}(x) = \phi(x, \mu \to \infty) = 6x(1-x)\,. \tag{2.31}$$

Furthermore, the Mellin moments of the distribution corresponding to the PDA are given by:

$$\langle x^m \rangle = \int_0^1 x^m \phi_M(x) dx\,, \tag{2.32}$$

where, once again it is essential to satisfy the normalization condition:

$$\langle x^0 \rangle = \int_0^1 dx \phi_M(x) = 1\,. \tag{2.33}$$

New facilities are nowadays discussed to test the behavior of hadrons at different energy scales in order to produce important quantum states for the Physics community such are the Goldstone bosons. Since pion and kaon pseudoscalar mesons are largely produced in high-energy reactions, one would naively expect that the kinematics of the constituent partons would be known at a certain level of accuracy. However, strong dynamics makes this statement hard to realize, since the separation of soft from hard interactions is not a simple task. Thus, as an alternative approach, the theoretical community is developing different effective theories to understand the full theory of hadrons and providing accurate phenomenological predictions. In fact there have been great predictions inspired by phenomenological approaches for instance, Schwinger-Dyson equations (SDEs) [26, 56–59], lattice-QCD [60], Non-relativistic QCD (nrQCD) [61], etc. In the following chapter we will focus on the Schwinger-Dyson equations to describe then the most fundamental particles and its interactions in the non perturbative regime.

Chapter 3

The Schwinger-Dyson and Bethe-Salpeter Approaches

The SDEs, named in honor of Julian Schwinger and Freeman Dyson, have earned a classic status since their introduction at the inception of quantum field theory. These non-perturbative equations form an infinite set of coupled integral equations that establish the connection between Green's functions in a quantum field theory. Consequently, they offer a comprehensive depiction of the theory, enabling the investigation of crucial aspects of QCD, such as dynamical chiral symmetry breaking (DCSB) and the confinement of quarks and gluons.

Deriving the SDEs can be accomplished through Feynman path integrals or via an intuitive approach involving perturbative diagrammatic expansion in powers of the α coupling. However, this yields an infinite series of coupled integral equations, necessitating truncation for practical purposes. The most widely known and systematic truncation is the perturbative approach. Despite its effectiveness, there are instances where this expansion is not viable due to α being close to or even exceeding 1. In such cases, non-perturbative methods become indispensable for truncating these infinite equations. Various truncation schemes exist, and we will explore some of these later.

On the other hand, as we already know QCD is a gauge theory, quarks are confined inside hadrons and their mass (principaly for the light quarks) is dynamically generated through their interactions with gluons which is visible from the mass function, this

can be understood through DCSB. Therefore, let us proceed with describing the quark SDEs and the Bethe-Salpeter equation corresponding to the mesons first using a general and intuitive approach.

It is important to note that the solutions to Dyson-Schwinger equations are obtained in Euclidean space. Consequently, the crucial question of how to convert the results between Euclidean space and Minkowskian space arises. In the following, we will use then Euclidean time. Further details are provided in Appendix B.

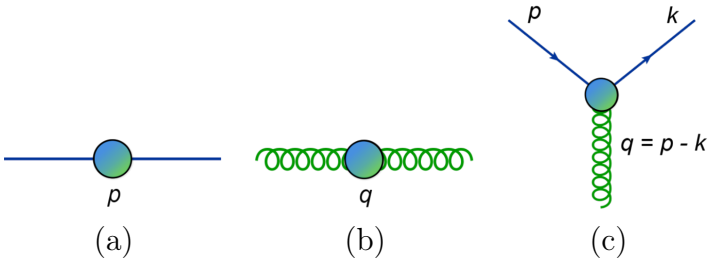

FIGURE 3.1: Representation of a dressed propagator and a vertex. (a) Dressed quark propagator, $S(p)$. (b) Dressed gluon propagator, $\Delta_{\mu\nu}(q)$. (c) Dressed quark-gluon vertex, $\Gamma^{\mu}(k,p)$.

Firstly, we present a schematic representation of the fully dressed propagators and vertex in Figure 3.1. The term "dressed" indicates that they include all possible corrections and have corresponding Feynman rules with additional factors compared to tree-level (or bare) propagators. Furthermore, each of these propagators and vertex obey their own SDE.

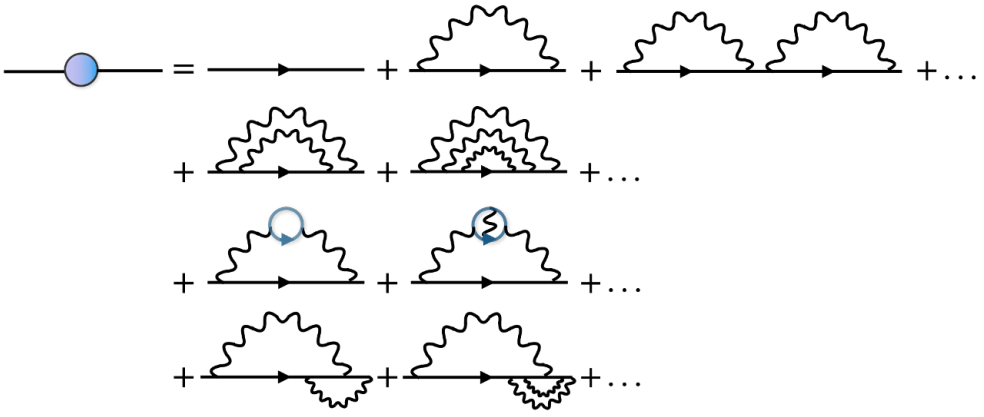

FIGURE 3.2: Corrections to the fermionic propagator.

The quark SDE, also known as the GAP equation, describes the dressed quark propagator, which can be derived by summing all conceivable perturbative corrections to the

bare fermionic propagator $S_0(p)$. In the context of QED interactions with the photon as the mediating gauge boson, there are four infinite series of corrections: re-corrections (combinations and repetitions of all correction types), corrections to the quark propagator, corrections to the photon propagator, and corrections to the quark-photon vertex. These components are visually depicted in Figure 3.2.

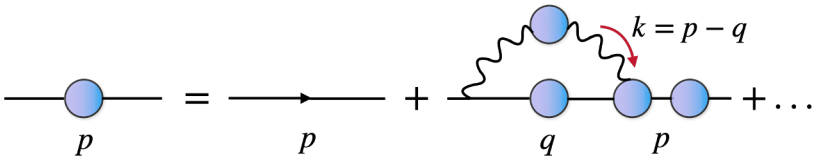

FIGURE 3.3: Complete fermionic propagator.

To simplify the representation, each type of correction can be denoted with a filled circle in its corresponding propagator or vertex, being the dressed propagators or vertex, leading to a reduced expression, as shown in Figure 3.3. Vertex corrections are displayed on one side to avoid redundancy.

This diagrammatic representation is mathematically expressed as:

$$\begin{aligned} iS(p) &= iS_0(p) + iS_0(p)\Sigma(p)iS_0(p) + iS_0(p)\Sigma(p)iS_0(p)\Sigma(p)iS_0(p) + ... \\ &= iS_0(p) + iS_0(p)\Sigma(p)\left[iS_0(p) + iS_0(p)\Sigma(p)iS_0(p) + ...\right] \\ &= iS_0(p) + iS_0(p)\Sigma(p)iS(p)\,, \end{aligned} \tag{3.1}$$

where $\Sigma(p)$ is named as the self energy, and $S_0(p)^{-1} = (i\not{p} + m_0)$ represents the bare fermionic propagator with m_0 the bare current quark mass as discussed in Chapter 1.

Multiplying the Eq. 3.1 on the right by $-iS^{-1}(p)$ and on the left by $S_0^{-1}(p)$, we obtain

$$S_0^{-1} = S^{-1}(p) + i\Sigma(p)\,, \tag{3.2}$$

from which it is evident that

$$S^{-1}(p) = S_0^{-1}(p) - i\Sigma(p)\,. \tag{3.3}$$

This corresponds to the GAP equation, and can also be represented diagrammatically as shown in Figure 3.4.

Similarly, we can extend this result to the exchanged QCD interaction by substituting the photon propagator with the gluon propagator. It is essential to note that unlike

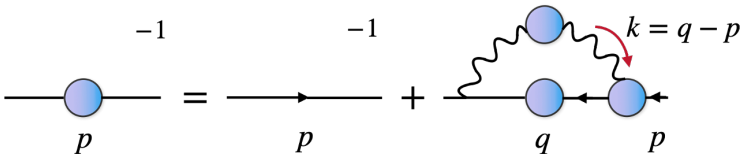

FIGURE 3.4: Quark Schwinger-Dyson equation.

the photon, the gluon interacts with itself through additional interactions adding many more Feynman diagrams. Nevertheless, when employing more sophisticated methods for calculations, they converge to the result obtained in Eq. (3.3).

3.1 Quark Schwinger-Dyson equation

One of the most studied SDE is the GAP equation (shown in Figure 3.4) which bounds the fully dressed gluon propagator, the fully dressed quark-gluon vertex and again the quark propagator. The quark SDE corresponding to Eq. (3.3) can be explicitly expressed as:

$$S^{-1}(p) = Z_2(i\gamma \cdot p + m_0) + \Sigma(p)\,, \tag{3.4}$$

where m_0 is the bare current quark mass, Z_2 is the quark renormalization constant and the self-energy has the explicit form:

$$\Sigma(p) = Z_{1f} g^2 C_f \int_\Lambda \frac{d^4q}{(2\pi)^4} \gamma^\mu S(q) \Gamma^\nu(l,k) D_{\mu\nu}(k)\,, \tag{3.5}$$

where,

- g is the strong coupling ($\alpha_{QCD} = g^2/(4\pi)$), the prefactor $C_f = 4/3$ comes from the color trace and the subscript Λ (the mass scale) indicates that the integral is regularised.
- $D_{\mu\nu}(k)$ is the dressed gluon propagator that depends on the gluon momentum $k = q - p$.
- Z_{1f} is the quark-gluon vertex renormalization constant. Both, Z_{1f} and Z_2 depend on the renormalization scale μ_R and on the regulator Λ.

- The dressed quark-gluon vertex $g\Gamma^\nu(l,k)$ depends on the average quark momentum $l = (q+p)/2$ and the gluon momentum k. It consists of 12 Lorentz-Dirac tensors:

$$\Gamma^\nu(l,k) = \sum_{j=1}^{4} \left(f_j^{(1)} i\gamma^\nu + f_j^{(2)} il^\nu + f_j^{(3)} ik^\nu \right) \tau_j(l,k)\,, \tag{3.6}$$

  where $f_j^m(l^2, l\cdot k, k^2, m^2)$ with $m = 1,2,3$ as Lorentz invariant functions and $\tau_j(l,k) = \{1, \not{k}, \not{l}, [\not{l}, \not{k}]\}$.

To ensure that the GAP equation can accurately reproduce perturbation theory, it must satisfy the following condition:

$$S^{-1}(p)|_{p^2=\mu_R^2} = i\gamma\cdot p + m_q(\mu_R)\,, \tag{3.7}$$

where, $m_q(\mu_R)$ is the renormalized current quark mass.

In QFT, the fundamental quantity characterizing a particle is its propagator. The counterparts of Eq. (3.10) for the propagators in QCD are the SDEs. Then, the most general form for the dressed quark propagator is

$$S(p) = \frac{-i\gamma\cdot pA(p^2,\mu_R^2) + B(p^2,\mu_R^2)}{A^2(p^2,\mu_R^2)p^2 + B^2(p^2,\mu_R^2)} = -i\gamma\cdot p\sigma_v(p^2,\mu_R^2) + \sigma_s(p^2,\mu_R^2)\,, \tag{3.8}$$

$$\equiv \frac{F(p^2,\mu_R^2)}{i\gamma\cdot p + M(p^2,\mu_R^2)}\,, \tag{3.9}$$

$$\Rightarrow \quad S^{-1}(p) = i\gamma\cdot pA(p^2,\mu_R^2) + B(p^2,\mu_R^2), \tag{3.10}$$

where, $A(p^2,\mu_R^2)$ and $B(p^2,\mu_R^2)$, or equivalently $\sigma_v(p^2,\mu_R^2)$ and $\sigma_s(p^2,\mu_R^2)$, or $F(p^2,\mu_R^2)$ and $M(p^2,\mu_R^2)$ are the dressing functions. Also, p^2 take values $p^2 \in \mathbb{C}$. Furthermore, as we already know the analytic structure of the propagators are more complex, hence, the functions $\sigma_v(p^2,\mu_R^2)$ and $\sigma_s(p^2,\mu_R^2)$ can also have poles in the complex plane of p^2, where the particles are on-shell ($p^2 = -m_q^2$).

The so-called renormalization of the wave function and the quark mass function are defined as $F(p^2,\mu_R^2) = 1/A(p^2,\mu_R^2)$ and $M(p^2,\mu_R^2) = B(p^2,\mu_R^2)/A(p^2,\mu_R^2)$ respectively. For a free spin-1/2 particle, the propagator simplifies to level tree according to $A(p^2,\mu_R^2) = 1$ and $B(p^2,\mu_R^2) = m_q(\mu_R)$. Using the renormalization conditions of

Eq. (3.7) one can relate $M(p^2, \mu_R^2)$ with $m_q(\mu_R)$ through

$$m_q(\mu_R) = M(\mu_R^2)\,. \tag{3.11}$$

To ensure multiplicative renormalization, the mass function is unaffected by the renormalization constant, setting it apart from the other dressing functions. That is, $M(p^2, \mu_R^2) = M(p^2)$.

Subsequently, in order to perform actual calculations, it becomes imperative to establish a truncation scheme, which will be discussed later. Prior to that, we shall present an overview of the equation governing quark-antiquark bound states, known as the Bethe-Salpeter equation.

3.2 Bethe-Salpeter equation

The BS equation provides a fully relativistic description of two-particle bound states, particularly relevant in the context of mesons. Independently formulated by several groups in the early 1950s [56, 57, 62–64], this equation, illustrated in Figure 3.5, represents a homogeneous integral equation that determines the BS amplitude (BSA). The explicit form of the BSE is given by

$$[\Gamma^{ab}_{\mathrm{M}}(p,P)]_{\alpha\beta} = \int \frac{d^4q}{(2\pi)^4} [\mathbf{K}]_{\alpha\gamma,\delta\beta} [\chi^{ab}_{\mathrm{M}}(q,P)]_{\gamma\delta}\,, \tag{3.12}$$

$$\chi^{ab}_{\mathrm{M}}(q,P) = S^a(q_+)\Gamma^{ab}_{\mathrm{M}}(q,P)S^b(q_-)\,, \tag{3.13}$$

where,

- $\Gamma^{ab}_{\mathrm{M}}(p,P)$ is the BSA of the meson (M) which represents the amputated and irreducible quark-meson vertex.
- $\chi^{ab}_{\mathrm{M}}(q,P)$ corresponds to the BS wave function (BSWF).
- $\mathbf{K}$ is the quark-antiquark irreducible kernel and the Greek subscripts are multi-indices in Dirac, color and flavor space. This must be determined consistently with the truncation of the gap equation.
- And again, $S(q_\pm)$ is the dressed quark propagator.

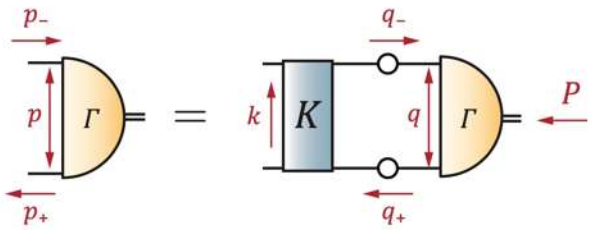

FIGURE 3.5: Bethe-Salpeter equation.

The kinematics for the BSA can be inferred from Figure 3.5. The amplitude depends on two independent momenta, the quark momenta p_+ and p_-, or equivalently the total meson momentum P and relative quark momentum p which are related by

$$p_\pm = p \pm \frac{P}{2} \quad \Leftrightarrow \quad \left.\begin{array}{ll} P & = p_+ - p_- \\ p & = \frac{p_+ + p_-}{2} \end{array}\right\} \quad \Rightarrow \quad p_\pm = p^2 + \frac{P^2}{4} \pm p \cdot P \,. \tag{3.14}$$

The analogous relations hold for the momenta inside the momentum loop, i.e., $q_\pm = q \pm P/2$. The total meson momentum is on-shell, i.e., $P^2 = -m_M^2$, where m_M is the mass of the meson M.

The BSA $\Gamma_{\rm M}(p, Q)$ has a Dirac, flavor and color part:

$$\Gamma_{\rm M}(p, Q) = Spin \otimes Flavor \otimes Color \,. \tag{3.15}$$

Specifically, we use the notations Γ_5 for pseudoscalars (PS), Γ_μ for vectors (V), Γ_1 for scalars, and $\Gamma_{5\mu}$ for pseudovectors or axial-vectors (AV), each representing different meson types with distinct transformation properties corresponding to their respective quantum numbers. The tensor structure of the BSA is thus dependent on the meson type, reflecting these diverse characteristics.

Consider, for instance, the pion, a PS meson with quantum numbers $J^{PC} = 0^{-+}$. In this case, the spin part of the Bethe-Salpeter amplitude (BSA) is represented by a matrix in Dirac space, relying on four linearly independent Dirac tensors ($f_1 + f_2 i\not{P} + f_3(p \cdot P) i\not{p} + f_4[\not{p}, \not{P}]$). These are associated with corresponding dressing functions $f_i(p^2, z, P^2 = -m_M^2)$. The complete BSA for a PS meson is expressed as follows:

$$\Gamma_5^{ab}(p, P) = \gamma_5[iE_5(p, P) + \gamma \cdot P F_5(p, P) + \gamma \cdot p\, p \cdot P G_5(p, P) + p_\alpha \sigma_{\alpha\beta} P_\beta H_5(p, P)] \,. \tag{3.16}$$

Similarly, the corresponding antimeson possesses a BSA given by:

$$\bar{\Gamma}_5^{ba}(p,P) = [C^{-1}\Gamma_5^{ab}(-p,P)C]^T\,. \tag{3.17}$$

The issue of normalizing the Bethe-Salpeter wave function is also worth mentioning. A well-defined normalization condition has been elegantly derived by Lurié et al. [65], and in a covariant form the canonical normalization condition is [66]:

$$\begin{aligned} 2P_\mu = &\frac{\partial}{\partial P_\mu}\left\{\int \frac{dq^4}{2\pi^4} tr_{CD}\left[\bar{\Gamma}_{\rm M}^{ba}(q,-K)S^a(q_+)\Gamma_{\rm M}^{ab}(q,K)S^b(q_-)\right]\right\} \\ &+ \frac{\partial}{\partial P_\mu}\left[\int \frac{dq^4}{2\pi^4}\int \frac{dk^4}{2\pi^4} tr_{CD}\left([\bar{\chi}_{\rm M}^{ba}(k,-K)]_{\beta\alpha}[\mathbf{K}]_{\alpha\gamma,\delta\beta}[\chi_{\rm M}^{ab}(q,K)]_{\delta\gamma}\right)\right], \end{aligned} \tag{3.18}$$

where $K^2 = P^2 = -m_{\rm M}^2$. This condition ensures that the Bethe-Salpeter amplitude accurately describes a meson with unit probability.

To solve the Bethe-Salpeter equation (BSE), one must possess knowledge of the quark-antiquark kernel $\mathbf{K}$. This kernel encompasses the sum of all conceivable $q\bar{q}$ interactions between quarks. When formulating such a kernel, it is crucial to exercise caution and ensure that fundamental properties, such as the Ward-Takahashi Identities (WTI) [67], are satisfied, and that the model remains consistent with the gap equation.

In the subsequent section, we will introduce a well-established truncation scheme that addresses these concerns.

3.3 Truncation scheme

As mentioned earlier, the quark-gluon vertex and the gluon propagator are governed by their own SDE, forming an infinite set of coupled equations that require a feasible treatment. To manage this complexity, a practical approach is to truncate the equations systematically by introducing an *Ansatz* for the quark-gluon vertex and the gluon propagator, effectively decoupling the infinite tower.

First, considering the gluon propagator, for convenience we work in Landau gauge [68, 69] ($\xi = 0$), where the gluon propagator is given by

$$D_{\mu\nu}(k) = (\delta_{\mu\nu} - \frac{k_\mu k_\nu}{k^2})\frac{Z(k^2)}{k^2}\,, \tag{3.19}$$

and $Z(k^2)$ is the gluon dressing function, which serves to model the non-perturbative behavior of the propagator at small k^2 values while preserving the perturbative behavior at large k^2 values. The Landau gauge serves as the fixed point within the renormalization group [68, 69]. Additionally, it effectively removes any corrections to the longitudinal component of the gluon propagator at all orders. Besides, it allows one to model the quark-gluon vertex without adding an explicit dependence on the gauge parameter.

Several models have been proposed for the gluon propagator in the infrared region [70], and significant progress has been made in our understanding of it [71–73]. The dressing function is bounded and exhibits a maximum at $k^2 = 0$, gradually decreasing along the space-like axis. Just like quarks, gluons dynamically acquire mass in the infrared, with this mass falling in the range of hundreds of MeVs.

Conversely, the quark-gluon vertex necessitates a tensor structure comprising 12 components. Researchers worldwide have made extensive efforts to construct this quark-gluon vertex [74–77]. A crucial requirement is that it accurately reproduces all perturbative predictions in the ultraviolet regime and adheres to constraints in the infrared region.

Considering these crucial considerations, the "Rainbow-Ladder truncation" emerges as a plausible *Ansatz* that consistently truncates both the gap equation and the Bethe-Salpeter equation.

Rainbow-Ladder truncation

We consider the "rainbow-ladder" approximation, where the dressed quark-gluon vertex is assumed to be bare:

$$\Gamma^\nu(l,k) = f(k^2)\gamma^\nu\,, \tag{3.20}$$

where the dressing function $f(k^2)$ depends on the gluon momentum only, which is

$$\alpha(k^2) = \frac{g^2}{4\pi}\frac{Z_{1f}}{Z_2^2}Z(k^2)f(k^2)\,. \tag{3.21}$$

Subsequently, we have the Maris-Tandy (MT) model [66, 78] for the coupling constant $\alpha(k^2)$ given by:

$$\alpha(k^2) = \pi\eta^7 x^2 e^{-\eta^2 x} + \frac{2\pi\gamma_m\left(1-e^{-k^2/\Lambda_t^2}\right)}{ln\left[e^2-1+\left(1+k^2/\Lambda_{QCD}^2\right)^2\right]}\,, \qquad x=\frac{k^2}{\Lambda^2}\,. \tag{3.22}$$

Here, we set specific parameters for the two terms: for the ultraviolet part, $\Lambda_t = 1$ GeV, $\Lambda_{QCD} = 0.234$ GeV, and $\gamma_m = 12/25$; whereas for the infrared part, $\Lambda = 0.72$ GeV and $\eta = 1.8$.

The MT model offers a commendable description of the properties of PS and V mesons. However, it has certain limitations. An alternative model that possesses the advantageous features of the MT model while avoiding its disadvantages is the Qin-Chang (QC) model. However, within the scope of the particular objectives of this study, there is no need to explore this more sophisticated alternative model. Consequently, we can proceed with confidence to address the gap and BSE equation using the MT model.

3.4 Numerical results

3.4.1 Solving the quark SDE

To solve the gap equation, we incorporate our truncation scheme and the general equation of the quark propagator, Eq. (3.10), into the quark SDE, Eq. (3.4). Subsequently, we multiply and divide the left-hand side of the equation by the complex conjugate of $A(q^2)i\gamma\cdot q + B(q^2)$ to facilitate the application of the trace operation, resulting in:

$$B(p^2) = Z_2 Z_m m + \frac{4}{3}Z_2^2\int\frac{d^4q}{(4\pi)^4}\frac{4\pi\alpha(k^2)}{k^2}\frac{3B(q^2)}{[A(q^2)q^2+B^2(q^2)]}\,. \tag{3.23}$$

Alternatively, prior to applying the trace operation, we can multiply by $i\not{p}$ to simplify the calculations and obtain:

$$A(p^2) = Z_2 + \frac{4}{3}Z_2^2 \int \frac{d^4q}{(4\pi)^4} \frac{4\pi\alpha(k^2)}{p^2k^2} \frac{A(q^2)q^2}{[A(q^2)q^2 + B^2(q^2)]} \left[q\cdot p + \frac{2}{k^2}(p\cdot k)(q\cdot k) \right] . \tag{3.24}$$

On the other hand, the integral is given by

$$\int \frac{d^4q}{(4\pi)^4} = \frac{1}{2}\int_0^{L^2} dq^2 \frac{q^2}{(2\pi)^4} \int_{-1}^{1} dz\sqrt{1-z^2} \int_{-1}^{1} dy \int_0^{2\pi} d\phi \,. \tag{3.25}$$

Here, L represents the cutoff in the system, and we employ hyperspherical variables:

$$q^\mu = \sqrt{q^2} \begin{bmatrix} \sqrt{1-z^2}\sqrt{1-y^2}sin\phi \\ \sqrt{1-z^2}\sqrt{1-y^2}cos\phi \\ \sqrt{1-z^2}y \\ z \end{bmatrix} , \quad p^\mu = \sqrt{p^2} \begin{bmatrix} 0 \\ 0 \\ 0 \\ 1 \end{bmatrix} . \tag{3.26}$$

Notably, the only Lorentz invariants in the system are p^2, q^2, and $p\cdot q = \sqrt{p^2}\sqrt{q^2}z$, resulting in the two integrations over the variables y and ϕ becoming trivial. Hence, only the integrations over q^2 and z remain. Additionally, the squared gluon momentum is expressed as:

$$k^2 = p^2 + q^2 - 2p\cdot q = p^2 + q^2 - 2pqz \,, \tag{3.27}$$

where $q = \sqrt{q^2}$ and $p = \sqrt{p^2}$.

The self-energy integrals are logarithmically UV-divergent when the cutoff L is sent to infinity, necessitating renormalization. Therefore, we impose the following conditions:

$$A(\mu^2) = 1, \;\; B(\mu^2) = m_q \,. \tag{3.28}$$

Here, m_q denotes the renormalized current-quark mass at some arbitrary renormalization point $p^2 = \mu^2$. Evaluating Eqs. (3.23) and (3.24) at μ^2, we can derive:

$$Z_2 = \frac{-1 + \sqrt{1 + 4\sum A(\mu^2)}}{2\sum A(\mu^2)}\,, \tag{3.29}$$

$$Z_m = \frac{m_q - Z_2^2 \sum B(\mu^2)}{Z_2 m_q}\,, \tag{3.30}$$

where, $\sum A(\mu^2)$ is the self-energy of the Eq. (3.24) evaluated in μ^2 and the same for $\sum B(\mu^2)$ respect the Eq. (3.23).

Integration method

To solve the quark SDE as described above and determine $A(p^2)$ and $B(p^2)$ as $M(p^2) = B(p^2)/A(p^2)$ we used Gaussian quadrature which tells us that we can solve the integrals using an approximation by sums like

$$\int_a^b g(x) f(x) dx \approx \sum_{i=1}^{n} w_i f(x_i)\,, \tag{3.31}$$

where w_i is the weight. The function $g(x)$ appears only on the left-hand side. It allows to make the quadrature exact for polynomials up to order $2n-1$ times the function $g(x)$. The values of the positions x_i and of the weights w_i depend on the choice of $g(x)$. For example, for $g(x) = 1$ it is called a Gauss-Legendre quadrature since it is based on Legendre polynomials. This implies that the choice of $g(x)$ also determines the values of the limits, a and b. For Gauss-Legendre they are set to $a = -1$ and $b = 1$. Therefore, an integral with different limits must be transformed to this interval. In principle, any transformation of an interval $z \in [a, b]$ that transforms this interval into $x \in [-1, 1]$ is possible.

For the integrals that we need to solve it is necessary to take for q the Gauss-Legendre quadrature and for the integration in z a Gauss-Chebyshev quadrature.

$g(x)$	Polynomials	Boundaries
1	Legendre	$[-1, 1]$
$1/\sqrt{1-x^2}$	Chebyshev first kind	$[-1, 1]$

For integrands for which the integration variable stretches over several orders of magnitude a logarithmic transformation is advantageous. Then, the change ($x \in [-1, 1]$ and $z \in [a, b]$):

$$z = \frac{(b-a)x + a + b}{2} \quad \Rightarrow \quad dz = \frac{(b-a)}{2} x \,, \tag{3.32}$$

allows to have a general integral as

$$\int_a^b dz f(z) = \frac{(b-a)}{2} \sum_i^n w_i f(z_i) \quad , z_i = z(x_i) \,, \tag{3.33}$$

where the Jacobian can be taken into account directly in the weights. Therefore, we can take

$$x = A + B \ln z \,, \tag{3.34}$$

$$z = e^{(z-A)/B} \,, \tag{3.35}$$

where the coefficients A and B are determined by the conditions $x(a) = -1$ and $x(b) = 1$ and the Jacobian:

$$dz = \frac{1}{B} e^{(z-A)/B} dx \,. \tag{3.36}$$

Now, we can continue with the mass function.

Mass function

Initially, we solved Eqs. (3.23) and (3.24) by considering only the first term of Eq. (3.22), which corresponds to the infrared part without the ultraviolet component. In this approach, renormalization was unnecessary, leading to $Z_2 = Z_m = 1$. Subsequently, using the quark masses provided in Table 3.1, we obtained the left panel of Figure 3.6.

Next, we extended the calculation to include both terms of Eq.(3.22), and we evaluated Eqs. (3.29) and (3.30) at $\mu = 19$ GeV. The resulting values were used to construct the right panel of Figure 3.6, where, once again, we employed the current quark masses from Table 3.1.

	Up	Down	Strange	Charm	Bottom	Top
Current Mass [GeV] (m_q)	0.0023	0.0048	0.095	1.275	4.18	173.07

TABLE 3.1: Current Masses of the quarks

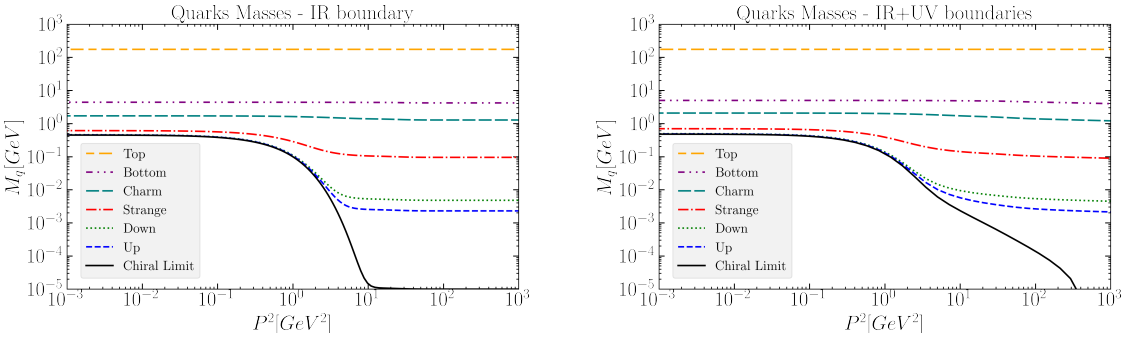

FIGURE 3.6: Quark mass function for different flavors as a function of the momentum P^2. The current masses of table 3.1 were used. Right panel- Mass function using the ultraviolet and infrared part in the Maris-Tandy model. Left panel- Mass function using only the infrared part in Maris-Tandy model.

Scalar and vector sigma fits

From Eq. (3.10) we observe that the quark propagator can be expressed in a scalar term and other vector term, where

$$\sigma_v = \frac{A(p^2)}{A^2(p^2)p^2 + B^2(p^2)}\,, \qquad \sigma_s = \frac{B(p^2)}{A^2(p^2)p^2 + B^2(p^2)}\,. \tag{3.37}$$

These terms were extracted from the program as shown in Figure 3.7, where we also made a fit of the data whit the complex plane.

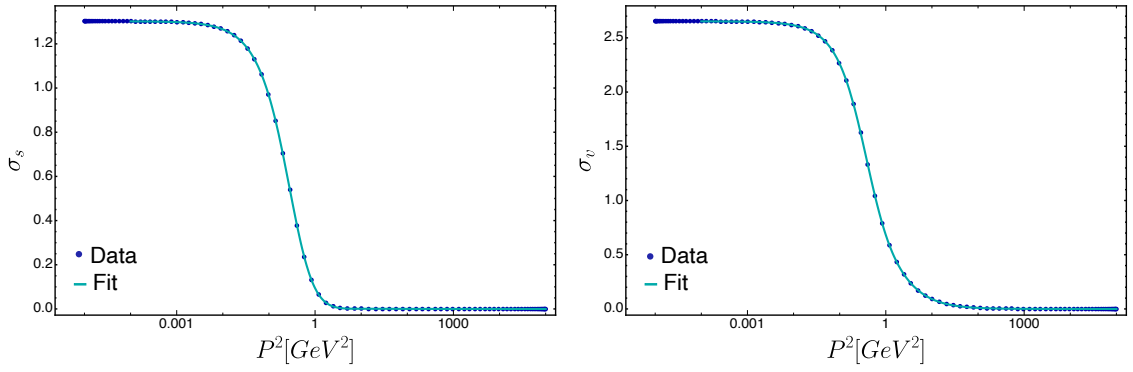

FIGURE 3.7: Right panel- $\sigma_s(p^2)$. Left panel- $\sigma_v(p^2)$.

We can observe that the use of only the infrared part in the Maris-Tandy model is a very good approximation since in effect we can see how the quarks acquire mass dynamically, which is thanks to the DCSB. However, for greater precision in the mass function and in specific the chiral limit where $m_q = 0$ is required to take into account the ultraviolet part as well.

3.4.2 Solving the BS equation

Resuming the BSE:

$$[\Gamma^{ab}_{\rm M}(p,P)]_{\alpha\beta} = \int \frac{d^4q}{(2\pi)^4}[\mathbf{K}]_{\alpha\gamma,\delta\beta}[\chi^{ab}_{\rm M}(q,P)]_{\gamma\delta}\,, \tag{3.38}$$

$$\chi^{ab}_{\rm M}(q,P) = S^a(q_+)\Gamma^{ab}_{\rm M}(q,P)S^b(q_-)\,. \tag{3.39}$$

It is necessary to mention that the interaction kernel's dependence on the truncation scheme is established through the following relation:

$$\left[\Sigma(p^+)\gamma_5 + \gamma_5\Sigma(p_-)\right] = \int \frac{d^4q}{(2\pi)^4}[\mathbf{K}]_{\alpha\gamma,\delta\beta}\left[\gamma_5 S(q_-) + S(q_+)\gamma_5\right]\,, \tag{3.40}$$

which is a corollary of the axial-vector WTI [67]. This guarantees that, in the chiral limit, the ground state PS mesons remain massless, despite the considerable enhancement of quark mass functions in the infrared (i.e. pions are the Goldstone bosons). In the case of explicit chiral symmetry breaking, it also establishes a precise connection between the PS meson mass, weak decay constant, current quark masses and the residue at the PS meson pole in the PS vertex [66].

Now, considering our focus on pions in the calculations of the BSE, the rainbow-ladder truncation satisfies the following constraints for the kernel in the BSE:

$$\mathbf{K}_{\alpha\gamma,\delta\beta} = Z_2^2\frac{4\pi\alpha(k^2)}{k^2}(t_a)_{AC}(t_a)_{DB}(i\gamma^\mu)_{\alpha\gamma}T_k^{\mu\nu}(i\gamma^\nu)_{\delta\beta}\,. \tag{3.41}$$

Here, Z_2 denotes the quark renormalization constant, while k_μ represents the gluon momentum. Working in Landau gauge, the transverse projector $T_{\mu\nu} = \delta_{\mu\nu} - k^\mu k^\nu/k^2$ is utilized. Additionally, the generators of $SU(3)_c$ in the fundamental representation are denoted as $t_a = \lambda_a/2$, where the λ_a correspond to the eight Gell-Mann matrices as

previously discussed in Chapter 1. The MT model, represented by $\alpha(k^2)$, is defined in a previous section, as seen in Eq. (3.22).

Regarding the flavor aspect in Eq. (3.15), it is worth noting that the rainbow-ladder kernel is flavor-independent and, taking advantage of our focus on pions, we can capitalize on isospin symmetry for the flavor part. Therefore, the flavor matrices for pions remain the same on both sides of the BSE, we can conveniently omit them.

On the other hand, concerning the color part in Eq. (3.15), as the pion is a color singlet, its color matrix becomes $\delta_{AB}/\sqrt{3}$. To conveniently maintain color normalization of 1, we include a factor of 1/3. Thus, the color factors of the BSE can be combined, resulting in:

$$(t_a)_{AC}(t_a)_{DB}\frac{\delta_{CD}}{\sqrt{3}} = \frac{1}{\sqrt{3}}\sum_{a=1}^{8}(t_a^2)_{AB} = \frac{4}{3}\frac{\delta_{AB}}{\sqrt{3}}\,. \tag{3.42}$$

In summary, the Dirac part of the BSE becomes:

$$\Gamma_\pi(p,P) = -\frac{4}{3}\int\frac{d^4q}{(2\pi)^4}Z_2^2\frac{4\pi\alpha(k^2)}{k^2}T_k^{\mu\nu}\gamma^\mu S(q_+)\Gamma_\pi(q,P)S(q_-)\gamma^\nu\,. \tag{3.43}$$

Similarly, as in the quark SDE, the integral measure is given

$$\int\frac{d^4q}{(4\pi)^4} = \frac{1}{2}\int_0^{L^2}dq^2\frac{q^2}{(2\pi)^4}\int_{-1}^{1}dz'\sqrt{1-z'^2}\int_{-1}^{1}dy\int_0^{2\pi}d\phi\,, \tag{3.44}$$

where L serves as the cutoff in the system, and we use the hyperspherical variables:

$$P^\mu = im_\pi\begin{bmatrix}0\\0\\0\\1\end{bmatrix},\; q^\mu = \sqrt{q^2}\begin{bmatrix}\sqrt{1-z'^2}\sqrt{1-y^2}sin\phi\\ \sqrt{1-z'^2}\sqrt{1-y^2}cos\phi\\ \sqrt{1-z'^2}y\\ z'\end{bmatrix},\; p^\mu = \sqrt{p^2}\begin{bmatrix}0\\0\\\sqrt{1-z^2}\\z\end{bmatrix}. \tag{3.45}$$

The only Lorentz invariants in the system are $P^2 = -m_M^2$, p^2, q^2, $p\cdot P \propto z$, $q\cdot P \propto z'$ and $p\cdot q \propto y$, so the integration over ϕ become trivial and we can set $\phi = 0$ right away.

We have all the necessary components to solve Eq. (3.43). By expressing Eq. (3.15) as

$$\Gamma_\pi(p,P) = \sum_{i=1}^{4}f_i(p^1,z)t_i(p,P)\,, \tag{3.46}$$

and substituting this into the BSE, we can project out the f_i on the left-hand side by contracting the equation with the charge-conjugate basis elements $\bar{t}_i$. Since the t_i are not orthonormal, we have

$$H_{ij}(p^2, z) = \frac{1}{4} Tr\left\{\bar{t}_i(p, P) t_j(p, P)\right\} \neq \delta_{ij} \,. \tag{3.47}$$

As a result, the BSE transforms into

$$H_{ij}(p^2, z) f_j(p^2, z) = \int_q K_{ij} f_j(q^2, z') \,, \tag{3.48}$$

$$K_{ij} = Z_2^2 \frac{16\pi}{3} \frac{\alpha(k^2)}{k^2} T_k^{\mu\nu} \frac{1}{4} Tr\left\{\bar{t}_i(p, P)\gamma^\mu S(q_+) t_j(q, P) S(-q_-)\gamma^\nu\right\} \,. \tag{3.49}$$

The matrices H and K are known, leading to a homogeneous linear integral equation for the f_i.

This approach allows us to numerically solve the quark SDE and the BSE, generating grids of numerical estimates for the quantities A, B, E_π, F_π, and G_π of the Eqs. (3.24, 3.23, 3.16). Within this scheme, H_π is usually neglected as it does not significantly contribute. However, these numerical grids might not be well-suited for future non-perturbative calculations of hadronic functions. To address this, parameterizations have been developed that enable interpolation within these grids for both the quark propagator and the BSAs.

3.5 Analytic parametrizations

These parameterizations are commonly referred as Perturbation Theory Integral Representations (PTIR) [79–82], as they exhibit similarities to expressions found in perturbation loop computations.

For the quark propagator, a typical parameterization involves the utilization of complex conjugate poles:

$$S(q) = \sum_{j=1}^{N} \left(\frac{z_j}{i\gamma \cdot q + m_j} + \frac{z_j^*}{i\gamma \cdot q + m_j^*} \right) \,, \tag{3.50}$$

where m_j and z_j are parameters determined from the numerical solutions. It is essential that at least one parameter m_j possesses a nonzero imaginary part, ensuring that the propagator avoids having poles on the real axis and maintains confinement characteristics.

Specifically, the dress functions are given by:

$$\sigma_v(q) = \sum_{j=1}^{N} \left(\frac{z_j}{q^2 + m_j^2} + \frac{z_j^*}{q^2 + m_j^2} \right) \ , \ \sigma_s(q) = \sum_{j=1}^{N} \left(\frac{z_j m_j}{q^2 + m_j^2} + \frac{z_j^* m_j^*}{q^2 + m_j^2} \right) \ , \tag{3.51}$$

wich meets that $S(q) = -i\gamma \cdot q\sigma_v(q^2) + \sigma_s(q^2)$, and it exhibits good fits for $N \geq 2$. An appealing feature of this approach is that, by considering space-like moments, it prevents the generation of on-shell quarks.

For parameterizing the BSAs, one effective technique is employing the Nakanishi integral representation (NIR) [83] or a similar form. This method involves expressing the BSAs as a functional form resembling the tree-level quark propagator, integrated over a spectral density as follows:

$$\mathcal{F}_{\mathrm{M}}(p, P) = \mathcal{F}^{IR}(p, P) + \mathcal{F}^{UV}(p, P) \, , \tag{3.52}$$

$$\mathcal{F}^{k}(p, P) = \int_{-1}^{1} dz \rho(z) \int_{0}^{\infty} d\Lambda (\Lambda - \Lambda_c) \frac{1}{(p^2 + zp \cdot P + \Lambda^2)^n} \ , \ (k = IR, UV) \tag{3.53}$$

where, $\mathcal{F}_{\mathrm{M}}(p, P)$ is the meson BSA, $\mathcal{F}^{k}(p, P)$ are the infrared or ultraviolet BSAs, $\rho(z)$ is the spectral density, Λ_c is a mass scale, and n is some suitable power.

Utilizing the Nakanishi representation, we can construct an illuminating Algebraic Model (AM) for both the quark propagator and the Bethe-Salpeter amplitude, as we will explore further. However, before delving into that, let's consider a model based on a vector $\times$ vector treatment of the SDEs named Contact Interaction (CI). This model not only incorporates confinement but also ensures the satisfaction of the axial vector WTI and at low energy the Goldberger-Treiman relations [84].

Both models offer the advantage of significant algebraic simplicity, enabling for example, straightforward calculations of EFFs even at high virtualities of the squared probe photon's momentum. This feature makes them valuable tools for the analysis of hadrons. In the upcoming sections, we will delve into the broader applications and scope of both models.

3.6 Contact Interaction model

We already mentioned that CI is a symmetry-preserving vector $\times$ vector interaction based on a gluon propagator that does not depend on momentum. CI describes four quarks interacting at a single point and was initially proposed in [84] for calculating the pion EFF. Since then, CI has been extensively utilized in various studies, including the investigation of EFFs and TFFs of mesons in Refs. [85–89].

One significant observation is that EFFs obtained from CI tend to be harder compared to those derived from full QCD predictions. Nevertheless, the results serve as a benchmark for comparison with more sophisticated QCD-based SDE results and the AM, providing insights into the correct pattern of DCSB and the large Q^2 evolution of the EFFs, which emerges from asymptotic QCD where Q^2 greatly exceeds any other relevant mass scale in the problem.

Then in CI, it is assumed that quarks interact not through massless vector-boson exchange but via the CI approach, where the gluon propagator is frozen in a manner consistent with the infrared properties of QCD. Therefore, the gluon propagator looks like

$$g^2 D_{\mu\nu}(k) = 4\pi \hat{\alpha}_{\rm IR} \delta_{\mu\nu} \,, \tag{3.54}$$

where $\delta_{\mu\nu}$ is the Kronecker delta. The parameter $\hat{\alpha}_{\rm IR}$ is defines as $\hat{\alpha}_{\rm IR} = \alpha_{\rm IR}/m_g^2$, with the scale m_g added for dimensional reasons and it is interpreted as the infrared gluon mass scale generated dynamically within QCD [84, 90, 91]. The current accepted value for m_g is $500\,,\mathrm{MeV}$ [92–95]. In the CI gap equation, the effective coupling that appears is $\hat{\alpha}_{\rm IR}$ instead of $\alpha_{\rm IR}$.

Here, $\alpha_{\rm IR}/\pi$ is chosen to be 0.36 to ensure $\hat{\alpha}_{\rm IR}$ retains the same value as in all related previous works [84, 91, 96, 97]. In addition, the interaction vertex remains bare, represented by $\Gamma^\nu(q,p) = \gamma^\nu$.

3.6.1 Gap equation

To calculate the gap equation in the CI treatment, we can use the *Ansätze* recently shown in Eqs. (3.4) and (3.5) and choosing $Z_{1f} = Z_2 = 1$ we will have

$$S^{-1}(p) = (i\gamma \cdot p + m_0) + \frac{1}{3\pi^2 m_g^2}\int_q^\Lambda \gamma^\mu S(q)\gamma_\mu \,, \tag{3.55}$$

where we have made the notation change $\int \frac{d^4q}{4\pi^2} \to \int_q^\Lambda$. Then substituting the Eq. (3.9) and multiplying by $\gamma \cdot p$ we will obtain:

$$\begin{aligned}\frac{ip^2}{F(p^2)} + \frac{M(p^2)}{F(p^2)}\gamma \cdot p = ip^2 + m_0\gamma \cdot p + \frac{1}{3\pi^2 m_g^2}\Bigg[\int_q^\Lambda \gamma_\mu \frac{-i\gamma \cdot p\gamma \cdot qF(q^2)}{q^2 + M^2(q^2)}\gamma_\mu \\ + \int_q^\Lambda \gamma_\mu \frac{\gamma \cdot pM(q^2)}{q^2 + M^2(q^2)}\gamma_\mu\Bigg] \,.\end{aligned} \tag{3.56}$$

Upon performing the substitution $q \to -q$, it becomes apparent that the first integral becomes an odd function, prompting us to set it equal to zero. Furthermore, when we take the trace of the resulting equation, it becomes evident that $F(p^2)$ simplifies to 1. Consequently, this allows us to determine the function $M(p^2)$ through

$$Tr\left[M(p^2)\right] = Tr\left[m_0 + \frac{1}{3\pi^2 m_g^2}\int_q^\Lambda \frac{\gamma \cdot pM(q^2)}{q^2 + M^2(q^2)}\gamma_\mu\gamma_\mu\right] \,. \tag{3.57}$$

Considering that $d^4q = q^3 dq \sin^2\theta\, d\theta \sin\phi\, d\phi\, d\psi$ with $\theta, \phi = [0, \pi]$ and $\psi = [0, 2\pi]$, therefore

$$\begin{aligned}\int d^4q &= \int_0^\infty dq q^3 \int_0^\pi \sin^2\theta d\theta \int_0^\pi \sin\phi d\phi \int_0^{2\pi} d\psi \\ &= \frac{1}{2}\int_0^\infty dq^2 q^2 \left(\frac{\pi}{2}\right)(2)(2\pi) \\ &= \pi^2 \int_0^\infty dq^2 q^2 \,.\end{aligned} \tag{3.58}$$

Utilizing the above integral and introducing the change of variable $s = q^2$, with the awareness that $M(p^2) = M_q$ constitutes a solution to the gap equation, we arrive at:

$$M_q = m_0 + \frac{M_q}{3\pi^2 m_g^2}\int_0^\infty ds \frac{s}{s + M_q^2} \,. \tag{3.59}$$

Subsequently, we proceed with the regularization of proper time, for which:

$$\int_a^b dx e^{-x(s+M_q)} = \frac{e^{-a(s+M_q)} - e^{-b(s+M_q)}}{s+M_q^2}\,. \tag{3.60}$$

Then,

$$\frac{1}{s+M_q^2} = \int_0^\infty d\tau e^{-\tau(s+M_q^2)} \Longrightarrow \int_{\tau_{UV}^2}^{\tau_{IR}^2} d\tau e^{-\tau(s+M_q^2)} = \frac{F(s)}{s+M_q^2}\,, \tag{3.61}$$

where $\tau_{UV}^2 = 1/\Lambda_{UV}^2$, $\tau_{IR}^2 = 1/\Lambda_{IR}^2$ are the infrared and ultraviolet regulators. Thus,

$$F(s) = e^{-(s+M_q^2)r_{UV}^2} - e^{-(s+M_q^2)r_{IR}^2}\,, \tag{3.62}$$

and substituting the Eq. (3.61) in Eq. (3.59) we see that

$$M_q = m_0 + \frac{M_q}{3\pi^2 m_g^2}\int_0^\infty ds \frac{s}{s+M_q^2}\left[e^{-(s+M_q^2)r_{UV}^2} - e^{-(s+M_q^2)r_{IR}^2}\right]. \tag{3.63}$$

Now, making the change of variable $s + M_q^2 = s'$ we will have the integral in the following form

$$\begin{aligned}\int_0^\infty ds \frac{s}{s+M_q^2}\left[e^{-(s+M_q^2)r_{UV}^2} - e^{-(s+M_q^2)r_{IR}^2}\right] &= \int_{M_q^2}^\infty ds' \frac{s'-M_q^2}{s'}\left[e^{-s'r_{UV}^2} - e^{-s'r_{IR}^2}\right] \\ &= \int_{M_q^2}^\infty ds'\left[e^{-s'r_{UV}^2} - e^{-s'r_{IR}^2}\right] - M_q^2\left[\int_{M_q^2}^\infty ds' \frac{1}{s'} e^{-s'r_{UV}^2} - \int_{M_q^2}^\infty ds' \frac{1}{s'} e^{-s'r_{IR}^2}\right].\end{aligned} \tag{3.64}$$

Performing again another change of variable $s' r_{UV}^2 = t$ we would have that the first integral would result:

$$\begin{aligned}\int_{M_q^2}^\infty ds'\left[e^{-s'r_{UV}^2} - e^{-s'r_{IR}^2}\right] &= \int_{M_q^2 r_{UV}^2}^\infty dt r_{UV}^{-2} e^{-t} - \int_{M_q^2 r_{IR}^2}^\infty dt r_{IR}^{-2} e^{-t} \\ &= \frac{1}{r_{UV}^2} e^{-M_q^2 r_{UV}^2} - \frac{1}{r_{IR}^2} e^{-M_q^2 r_{IR}^2}\,,\end{aligned} \tag{3.65}$$

the second integral:

$$\begin{aligned}-M_q^2 \int_{M_q^2}^\infty ds' \frac{1}{s'} e^{-s'r_{UV}^2} &= -M_q^2 \int_{M_q^2 r_{UV}^2}^\infty \frac{dt}{t} e^{-t} \\ &= -M_q^2 \Gamma(0, M_q^2 r_{UV}^2)\,,\end{aligned} \tag{3.66}$$

and the third integral:

$$M_q^2 \int_{M_q^2}^{\infty} ds' \frac{1}{s'} e^{-s' r_{IR}^2} = M_q^2 \int_{M_q^2 r_{IR}^2}^{\infty} \frac{dt}{t} e^{-t} = M_q^2 \Gamma(0, M_q^2 r_{IR}^2) \,. \tag{3.67}$$

We have taken into account the incomplete gamma-function:

$$\Gamma(\alpha, y) = \int_y^{\infty} dt t^{\alpha-1} e^{-t} \,. \tag{3.68}$$

Subsequently, naming the complete integral Eq. (3.64) as $\mathcal{C}(M^2, \tau_{IR}^2, r_{UV}^2)$ we will have

$$\mathcal{C}(M_q^2, \tau_{IR}^2, r_{UV}^2) = \frac{1}{r_{UV}^2} e^{-M_q^2 r_{UV}^2} - \frac{1}{r_{IR}^2} e^{-M_q^2 r_{IR}^2} - M_q^2 \Gamma(0, M_q^2 r_{UV}^2) + M_q^2 \Gamma(0, M_q^2 r_{IR}^2) \,, \tag{3.69}$$

Thus, the Eq. (3.63) would end up as:

$$M_q = m_0 + \frac{M_q}{3\pi^2 m_g^2} \mathcal{C}(M_q^2, \tau_{IR}^2, r_{UV}^2) \,. \tag{3.70}$$

From this equation, it becomes evident that we can once again deduce the outcomes of dynamic mass generation from the mass function derived through the CI approach. Table 3.2 provides an overview of the generated masses M_q from the current masses m_q as given in Eq. (3.70). For more details on these results, see [28].

TABLE 3.2: Current (m_q) and dressed (M_q) masses for quarks in GeV.

$m_u = 0.007$	$m_s = 0.17$	$m_c = 1.08$	$m_b = 3.92$
$M_u = 0.367$	$M_s = 0.53$	$M_c = 1.52$	$M_b = 4.75$

We report results for PS mesons using the parameter values listed in Tables 3.3, 3.2, whose variation with quark mass was dubbed as *heavy parameters* in Ref. [91]. In this approach, the coupling constant and the ultraviolet regulator vary as a function of the quark mass. This behavior was first suggested in Ref. [98] and later adopted in several subsequent works [85, 91, 97, 99, 100].

TABLE 3.3: Ultraviolet regulator and coupling constant for different combinations of quarks in PS mesons. $\hat{\alpha}_{\rm IR} = \hat{\alpha}_{\rm IRL}/Z_H$, where $\hat{\alpha}_{\rm IRL} = 4.57$ is extracted from the best-fit to data as explained in Ref. [85]. $\Lambda_{\rm IR} = 0.24$ GeV is a fixed parameter.

quarks	Z_H	$\Lambda_{\rm UV}$ [GeV]	$\hat{\alpha}_{\rm IR}$
u, d, s	1	0.905	4.57
c, u, s	3.034	1.322	1.50
c	13.122	2.305	0.35
b, u	11.273	3.222	0.41
b, s	17.537	3.574	0.26
b, c	30.537	3.886	0.15
b	129.513	7.159	0.035

3.6.2 BSE in the CI treatment

We once again examine Eq. (3.12) corresponding to the BSE governing a bound state, and regarding, the BSA for PS mesons that is described by Eq.(3.16). Within the framework of the CI model, the general decomposition of the BSA for PS and scalar (S) mesons ($q\bar{h}$) takes the following form:

$$\begin{aligned} \Gamma_{PS}(P) &= i\gamma_5\, E_{PS}(P) + \frac{1}{2M_R}\gamma_5\gamma\cdot P\, F_{PS}(P)\,, \\ \Gamma_{S}(P) &= I_D\, E_S(P)\,. \end{aligned} \tag{3.71}$$

Observe that $E_i(P)$ and $F_i(P)$, where $i = PS, S$, represent the BSAs for the respective meson being examined. Here, P signifies the total momentum of the meson, I_D stands for the identity matrix, and $M_R = M_q M_{\bar{h}}/[M_q + M_{\bar{h}}]$ denotes the reduced mass of the system. The labels q and $\bar{h}$ which denote the valence quark and antiquark flavors are in general different but might also be the same.

Among the *Ansätze* of the CI model, a kernel that fulfills all the requisite symmetric properties to accurately describe the interaction between quarks and antiquarks in QCD is

$$\mathcal{K} = \frac{4}{3m_g^2}\gamma_\mu\gamma_\nu\delta_{\mu\nu}\,. \tag{3.72}$$

From here, this approach also facilitates the numerical solution of the BSE, yielding grids of numerical estimates for the scalar functions $E_i(P)$ and $F_i(P)$, integral components essential for EFF calculations. Nevertheless, these grids might prove inadequate for other non-perturbative function computations. Hence, the development of parameterizations to interpolate within these grids becomes necessary.

3.6.3 The quark-photon vertex for the CI treatment

The quark-photon vertex (QPV), denoted by $\Gamma^\gamma_\mu(k_+, k_-, M_{f_1})$, is related to the quark propagator through the following vector Ward-Takahashi identity:

$$iP_\mu \Gamma^\gamma_\mu(k_+, k_-, M_{f_1}) = S^{-1}(k_+, M_{f_1}) - S^{-1}(k_-, M_{f_1})\,. \tag{3.73}$$

Without loss of generality, we have made the change from q to f_1 to avoid confusing notations of quarks.

This identity is crucial for a sensible study of a bound-state's EFF. It is determined through the following inhomogeneous BSE,

$$\Gamma^\gamma_\mu(Q, M_{f_1}) = \gamma_\mu - \frac{16\pi\hat{\alpha}_{\rm IR}}{3}\int \frac{d^4q}{(2\pi)^4}\gamma_\alpha \chi_\mu(q_+, q, M_{f_1})\gamma_\alpha\,, \tag{3.74}$$

where $\chi_\mu(q_+, q, M_{f_1}) = S(q+P, M_{f_1})\Gamma_\mu(Q)S(q, M_{f_1})$.

Owing to the momentum-independent nature of the interaction kernel, the general form of the solution is

$$\Gamma^\gamma_\mu(Q, M_{f_1}) = f\gamma^L_\mu(Q)P_L(Q^2, M_{f_1}) + \gamma^T_\mu(Q)P_T(Q^2, M_{f_1}), \tag{3.75}$$

where $\gamma^L_\mu + \gamma^T_\mu = \gamma_\mu$ and

$$\gamma^T_\mu(Q) = \gamma_\mu - \frac{\gamma\cdot Q}{Q^2}\,Q_\mu\,. \tag{3.76}$$

Inserting this general form into Eq. (3.74), one readily obtains (on simplifying notation)

$$P_L = 1\,, \quad P_T = \frac{1}{1 + K_\gamma(Q^2, M_{f_1})}, \tag{3.77}$$

with

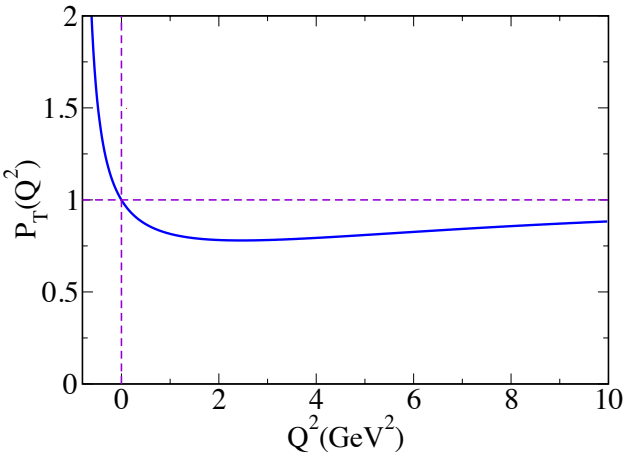

FIGURE 3.8: Dressing function of the transverse quark-photon vertex, $P_T(Q^2)$, in Eq. (3.77). The dashed lines are only representations of the axes zero and one.

$$K_\gamma(Q^2, M_{f_1}) = \frac{4\hat{\alpha}_{\rm IR}}{3\pi}\int_0^1 d\alpha\, \alpha(1-\alpha)Q^2\, \bar{\mathcal{C}}_1(\omega)\,, \tag{3.78}$$

where

$$\bar{\mathcal{C}}_1(z) = -\frac{d}{dz}\mathcal{C}(z) = \Gamma(0, z\,\tau_{\rm UV}^2) - \Gamma(0, z\,\tau_{\rm IR}^2) \tag{3.79}$$

and

$$\omega = \omega(M_{f_1}^2, \alpha, Q^2) = M_{f_1}^2 + \alpha(1-\alpha)Q^2\,. \tag{3.80}$$

One can clearly observe from Figure 3.8 that $P_T(Q^2) \to 1$ when $Q^2 \to \infty$, yielding the perturbative bare vertex γ_μ as expected.

3.7 An Algebraic model

Utilizing a suitable representation grounded in NIR, a profound algebraic model emerges for both the quark propagator and the BSA. The strategy for the BSA of PS mesons entails prioritizing the dominant term of Eq. (3.16), focusing on its diagonal element. Concerning the quark propagators, the algebraic model uses one of the building blocks of the parameterisation in Eq. (3.50) leveraging the effective quark mass.

It's important to note that, as elucidated earlier, a pivotal concept within QCD is the dynamic generation of masses. Nonetheless, when working within the framework of the algebraic model, our scope is restricted to the mass generated post DCSB, a phenomenon occurring in the realm of lower momentum regimes.

Hence, the algebraic model derived from phenomenological considerations and characterizing the quark propagator and the BSA of a pseudoscalar meson is expressed as [27]:

$$S_{q(\bar{h})}(k) = \left[-i\gamma\cdot k + M_{q(\bar{h})}\right]\Delta\left(k^2; M^2_{q(\bar{h})}\right), \tag{3.81}$$

$$n_{\mathrm{M}}\Gamma_{\mathrm{M}}(k,p) = i\gamma_5\int_{-1}^{1} dw\,\rho_{\mathrm{M}}(w)\left[\hat{\Delta}\left(k_w^2;\Lambda_w^2\right)\right]^{\nu}. \tag{3.82}$$

Herein, we have the expressions $\Delta(a,b) = (a+b)^{-1}$, $\hat{\Delta}(a,b) = b\Delta(a,b)$, and $k_w = k + (w/2)p$. In this context, $\nu = 1+\delta$ serves as a parameter governing the asymptotic behavior of the BSA, where δ represents an anomalous dimension. The constituent mass scale for a given quark or antiquark flavor, q or $\bar{h}$, is denoted by $M_{q(\bar{h})}$, while n_{M} represents a normalization constant. Importantly, the function $\rho_{\mathrm{M}}(w)$ is regarded as a spectral density, whose form determines the pointwise behavior of the BSA, having a significant influence on meson observables. In the forthcoming chapter, we will delve into the extraction of the spectral density function in the algebraic model. Lastly, $\Lambda_w^2 \equiv \Lambda^2(w)$ is defined as follows:

$$\Lambda_w^2 \equiv M_q^2 - \frac{1}{4}\left(1-w^2\right)m_{\mathrm{M}}^2 + \frac{1}{2}\left(1-w\right)\left(M_{\bar{h}}^2 - M_q^2\right). \tag{3.83}$$

In contrast to similar models [52–55, 101–106] that have been effectively employed to compute an array of GPD-related distributions, we have introduced a modification by advancing from Λ to Λ_w, thereby encompassing a w-dependence. Taking into account the effectiveness of previous models, we highlight several significant differences that lead to the simplification of pertinent integrals and the derivation of concise algebraic expressions that connect diverse distributions:

- We retain the constant term inherited from the original models and set it to M_q.

- A term linear in w is introduced, representing the sole term lacking symmetry under $w \leftrightarrow -w$. This asymmetry enables the examination of mesons composed of quarks with differing flavors and is accompanied by the multiplicative factor of $(M_{\bar{h}}^2 - M_q^2)$. For cases where quark-antiquark pairs share the same flavor, this term, by its construction, does not contribute.

- Additionally, a quadratic term in w^2 is incorporated, with its coefficient proportionate to m_M^2. The coefficients for each power of w are meticulously selected to ensure the fulfillment of the following condition:

$$|M_{\bar{h}} - M_q| \leq m_{\mathrm{M}} \leq M_{\bar{h}} + M_q \tag{3.84}$$

  as a prerequisite for the positivity of $\Lambda^2(w)$. This condition is underpinned by the fact that the minimum of Eq. (3.83) corresponds to:

$$w_0 = \frac{M_{\bar{h}}^2 - M_q^2}{m_{\mathrm{M}}^2}\,, \tag{3.85}$$

  resulting in:

$$\Lambda^2(w_0) = \frac{2\left(M_{\bar{h}}^2 - M_q^2\right) m_{\mathrm{M}}^2 - m_{\mathrm{M}}^4 - \left(M_{\bar{h}}^2 - M_q^2\right)^2}{4m_{\mathrm{M}}^2}\,. \tag{3.86}$$

Should quark and antiquark possess the same flavor, the left side of the inequality Eq. (3.84) is inherently satisfied. We assume isospin symmetry, denoting $M_u = M_d$. However, for other instances, such as in the case of kaons or heavy-light mesons, careful consideration is needed when establishing the ratio $M_{\bar{h}}/M_q$, with realistic solutions of the quark SDE often providing valuable reference points [107]. It is noteworthy that $m_{\mathrm{M}} < M_{\bar{h}} + M_q$ is consistently met for Nambu-Goldstone bosons. Suitable values for the constituent masses can be chosen to ensure this inequality for ground state PS mesons.

3.7.1 BSE in the AM treatment

Combining Eqs. (3.13), (3.81), (3.82), the BSWF acquires the following Nakanishi integral representation (NIR):

$$n_{\rm M}\chi_{\rm M}(k_-,P)=\mathcal{M}_{q,\bar{h}}(k,P)\int_{-1}^{1}dw\,\tilde{\rho}^{\nu}_{\rm M}(w)\mathcal{D}^{\nu}_{q,\bar{h}}(k,P)\,, \tag{3.87}$$

where the profile function, $\tilde{\rho}^{\nu}_{\rm M}(w)$, has been defined in terms of the spectral density as

$$\tilde{\rho}^{\nu}_{\rm M}(w)\equiv\rho_{\rm M}(w)\Lambda_w^{2\nu}\,. \tag{3.88}$$

The function $\mathcal{M}_{q,\bar{h}}(k=p+P,P)$ characterizes $\chi_M(k,P)$ having the entire tensor structure of it. Then, $\mathcal{M}_{q,\bar{h}}(k,P)$ is defined as follows:

$$\mathcal{M}_{q,\bar{h}}(k,P)\equiv-\gamma_5\big[M_q\gamma\cdot P+\gamma\cdot k(M_{\bar{h}}-M_q)+\sigma_{\mu\nu}k_\mu P_\nu-i\,(k\cdot p+M_qM_{\bar{h}})\big]\,. \tag{3.89}$$

Due to the trace over Dirac indices, *cf.* Eq. (4.1), the last two terms containing an even number of γ-matrices in the above Eq. (3.89) do not contribute to the leading-twist light-front wave function (LFWF) and, consequently, the PDA, that is that, they do not contribute to the work of this thesis. The function $\mathcal{D}^{\nu}_{q,\bar{h}}(k,P)$ is a product of quadratic denominators,

$$\mathcal{D}^{\nu}_{q,\bar{h}}(k,P)\equiv\Delta\left(k^2,M_q^2\right)\Delta\left(k^2_{w-1},\Lambda^2_w\right)^{\nu}\Delta\left(p^2,M^2_{\bar{h}}\right)\,. \tag{3.90}$$

Feynman parametrization enables us to combine the denominators in Eq. (3.90) into a single one. Then a suitable change of variables and a subsequent rearrangement in the order of integration yields the expression:

$$n_{\rm M}\chi_{\rm M}(k_-,P)=\mathcal{M}_{q,\bar{h}}(k,P)\int_0^1 d\alpha\mathcal{F}_{\rm M}(\alpha,\sigma^{\nu+2})\,, \tag{3.91}$$

$$\begin{aligned}\mathcal{F}_{\rm M}(\alpha,\sigma^{\nu+2})=\nu(\nu+1)\Big[&\int_{-1}^{1-2\alpha}dw\int_{\frac{2\alpha}{w-1}+1}^{1}d\beta\\&+\int_{1-2\alpha}^{1}dw\int_{\frac{2\alpha+(w-1)}{w+1}}^{1}d\beta\Big]\frac{(1-\beta)^{\nu-1}\tilde{\rho}^{\nu}_{\rm M}(w)}{\sigma^{\nu+2}}\,,\end{aligned} \tag{3.92}$$

where $\sigma = (k-\alpha P)^2 + \Lambda^2_{1-2\alpha}$, and $\alpha,\ \beta$ are Feynman parameters. Since only $(1-\beta)^{\nu-1}$ depends on β, integration over $d\beta$ can be performed directly, thus yielding

$$\mathcal{F}_{\rm M}(\alpha,\sigma^{\nu+2}) = 2^\nu(\nu+1)\Big[\int_{-1}^{1-2\alpha} dw \left(\frac{\alpha}{1-w}\right)^\nu + \int_{1-2\alpha}^{1} dw \left(\frac{1-\alpha}{1+w}\right)^\nu\Big]\frac{\tilde{\rho}^\nu_{\rm M}(w)}{\sigma^{\nu+2}}\,. \tag{3.93}$$

In the section 4.3, we will explain how this extra algebraic integration allows us to completely derive $\tilde{\rho}^\nu_{\rm M}(w)$ in terms of the PDA.

3.7.2 The quark-photon vertex for the AM treatment

The interaction of a quark with an electromagnetic probe is encoded in the fully-dressed QPV, Γ_μ. It is convenient to express the latter in its unamputated version, which reads:

$$\chi^q_\mu(k_f,k_i) = S_q(k_f)\Gamma_\mu(k_f,k_i)S_q(k_i)\,. \tag{3.94}$$

We thus adopt the following *Ansatz* for χ^q_μ:

$$\begin{aligned}
\chi^q_\mu(k_f,k_i) &= T^{(1)}_\mu \Delta_{k^2\sigma_v} + T^{(2)}_\mu \Delta_{\sigma_v} + T^{(3)}_\mu \Delta_{\sigma_s}\,, \\
T^{(1)}_\mu &= \gamma_\mu\,, \\
T^{(2)}_\mu &= \not{k}_f\gamma_\mu\ \not{k}_i + \alpha_q(\not{k}_f\gamma_\mu\ \not{k}_i - \not{k}_i\gamma_\mu\ \not{k}_f)\,, \\
T^{(3)}_\mu &= i(\not{k}_f\gamma_\mu + \gamma_\mu\ \not{k}_i) \\
&\quad + i\alpha_q(\not{k}_f\gamma_\mu + \gamma_\mu\ \not{k}_i - \not{k}_i\gamma_\mu - \gamma_\mu\ \not{k}_f)\,;
\end{aligned} \tag{3.95}$$

here $\Delta_F = [F(k_f^2) - F(k_i^2)]/[k_f^2 - k_i^2]$ and $\sigma_{v,s}$ are the quark propagator dressing functions [108]:

$$\sigma_s(p^2) = M(p^2)\sigma_v(p^2) = \frac{Z(p^2)M(p^2)}{p^2+M^2(p^2)}\,. \tag{3.96}$$

In Ref. [109], $\alpha_q \neq 0$ was introduced momentum redistribution factor owing to the impossibility to simultaneously conserve the vector and axial-vector currents. As long as α_q is asymptotically damped, one will be able to recover the tree level vertex, $\Gamma_\mu \to \gamma_\mu$. In our case, this factor is expressed as

$$\alpha_q = \alpha_q^{(0)}\ \exp[-Q^2/(2m_q^2)]\,. \tag{3.97}$$

It is worth mentioning that *Ansatz* has shown its robustness in the computation of the pion EFF [110] and all two-photon TFFs involving ground-state neutral pseudoscalar mesons, [109, 111–113]. Furthermore, having been derived from the so-called gauge-technique [114], the construction in Eq. (3.95) fulfills crucial mathematical requirements [115, 116]: it is free of kinematic singularities, the free-field limit is properly recover, and satisfies its corresponding Ward-Green-Takahashi identity.

The latter is a key point in the present approach, since it enable us to express the QPV dressing functions in terms of those of the quark propagator. Thus, within the present AM, the Eq. (3.95) can be expressed in a rather simple way:

$$\chi^q_\mu(k_f, k_i) = \frac{\sum_{j=1}^{3} T^{(j)}_\mu X_j}{[k_f^2 + m_q^2][k_i^2 + m_q^2]}\,, \tag{3.98}$$

with $X_1 = m_q^2\,,\ X_2 = -1\,,\ X_3 = -m_q$.

Finally, it is important to highlight that this construction of the QPV introduces an extra parameter to determine, $\alpha_q^{(0)}$.

With these components at our disposal, we can conduct a variety of calculations. On one hand, we can scrutinize the vertex corresponding to processes like $\mathrm{M}\gamma\mathrm{M}$ to access the EFF or $\gamma\mathrm{M}\gamma$ to access the TFF, something know by us as the triangle diagram approximation. Simultaneously, using the previous components, by projecting the BSWF onto the light cone, we gain access to a diverse spectrum of non-perturbative functions such as the Light-Front Wave Functions (LFWFs), GPDs, PDFs, and EFFs, among others. This comprehensive suite of derived functions provides us with the necessary tools to unveil a wealth of information, facilitating a deeper comprehension of the internal structure of PS mesons. The upcoming chapter will delve into the intricacies of the light cone formalism, providing a more profound exploration of these concepts.

Chapter 4

Pseudo-scalar mesons through an AM in the LC formalism

Most physical observables associated with mesons can be calculated by combining our knowledge of their BSA and the quark propagator [117, 118]. In principle, this can be achieved through a rigorous computation involving the quark propagator SDE and the BSE in close connection with full QCD [58]. However, computing a multitude of experimentally interesting quantities such as EFFs [109–112, 119–122], PDAs, PDFs [123–129], and, especially, GPDs [54, 55, 103–105], remains a highly complex endeavor.

Nevertheless, our understanding of the intricate relationship between the quark propagator and the meson BSA has allowed us to develop a simple and effective Algebraic Model that can provide reliable predictions and facilitate algebraic manipulations. In this chapter, we apply the previously introduced AM to pseudo-scalar mesons, expressing it in terms of a form-invariant spectral density. A notable feature of this AM is that the spectral density is explicitly formulated in terms of the leading-twist PDA, eliminating the need for ad hoc assumptions about the spectral density. In this chapter, we will start then with the data-driven approach by proposing an Ansatz for the quark propagator and the BSA in terms of a spectral density function that remains invariant for all ground-state pseudo-scalar mesons. The BSWF can then be readily constructed, and its projection onto the light front yields the sought-after LFWF. Integrating this over the transverse momentum squared ($k_\perp^2$) provides access to the valence-quark PDA. Leveraging our current comprehensive knowledge of the PDAs of pseudo-scalar mesons [82, 127], we determine the model's parameters. We employ the

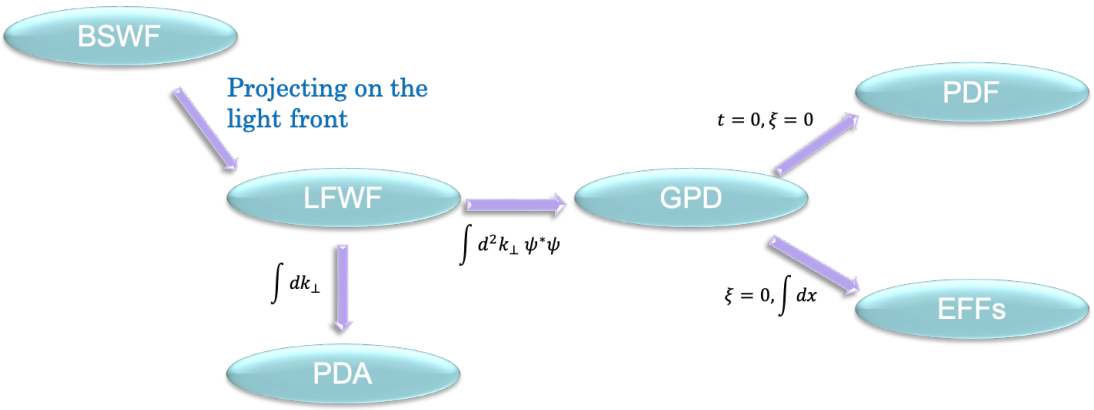

FIGURE 4.1: Potentialities through the overlap representation.

overlap representation of the LFWF [46] to compute the GPDs of pion, kaon, η_c, and η_b. From this three-dimensional knowledge of these mesons, various limits and projections allow us to deduce PDFs, FFs, and the GPDs impact parameter space (IPS-GPDs), which are then compared to existing experimental data.

In summary, we will observe how the light-cone formalism allows us to establish relationships between these functions, providing a comprehensive understanding of hadrons, as depicted in the figure 4.1. We commence by describing the BSE using our innovative AM.

4.1 Computing the LFWF and the PDA

For a quark q within a pseudo-scalar meson M, the leading twist (2 particle) light-front wave function, $\psi^q_{\rm M}$, can be obtained via the light-front projection of the meson's BSA as:

$$\psi^q_{\rm M}\left(x, k^2_\perp\right) = \mathrm{tr} \int_{dk_\parallel} \delta^x_n(k_{\rm M})\gamma_5\gamma\cdot n\, \chi_{\rm M}(k_-, P)\,, \tag{4.1}$$

where $\delta^x_n(k_{\rm M}) = \delta(n\cdot k - x\, n\cdot P)$; n is a light-like four-vector, such that $n^2 = 0$ and $n\cdot P = -m_{\rm M}$; a mentioned before, x corresponds to the light-front momentum fraction carried by the quark. The trace is taken over color and Dirac indices. The notation

$\int_{dk_\parallel} \equiv \int \frac{d^2k_\parallel}{\pi}$ has been employed and the 4-momentum integral is defined as usual:

$$\int \frac{d^4k}{(2\pi)^4} = \left[\frac{1}{16\pi^3}\int d^2k_\perp\right]\left[\frac{1}{\pi}\int d^2k_\parallel\right] . \tag{4.2}$$

The moments of the distribution are:

$$\langle x^m\rangle_{\psi^q_{\rm M}} = \int_0^1 dx\, x^m\, \psi^q_{\rm M}\left(x,k^2_\perp\right) = {\rm tr}\frac{1}{n\cdot P}\int_{dk_\parallel}\left[\frac{n\cdot k}{n\cdot P}\right]^m \gamma_5\gamma\cdot n\chi_{\rm M}(k_-,P) . \tag{4.3}$$

From Eqs. (3.91)-(4.3), one arrives at

$$\begin{aligned}\langle x^m\rangle_{\psi^q_{\rm M}} &= \int_0^1 d\alpha\alpha^m\left[\frac{12}{n_{\rm M}}\frac{\mathcal{Y}_{\rm M}(\alpha,\sigma_\perp^{\nu+1})}{\nu+1}\right] , \\ \mathcal{Y}_{\rm M}(\alpha,\sigma_\perp^{\nu+1}) &= \mathcal{F}_{\rm M}(\alpha,\sigma_\perp^{\nu+1})(\alpha M_{\bar h}+(1-\alpha)M_q) ,\end{aligned} \tag{4.4}$$

where $\sigma_\perp = k^2_\perp + \Lambda^2_{1-2\alpha}$. Uniqueness of the Mellin moments, Eqs. (4.3)-(4.4), implies the connection between the Feynman parameter α and the momentum fraction x; therefore one can identify the LFWF as

$$\psi^q_{\rm M}(x,k^2_\perp) = \left[\frac{12}{n_{\rm M}}\frac{\mathcal{Y}_{\rm M}(x,\sigma_\perp^{\nu+1})}{\nu+1}\right] . \tag{4.5}$$

Notice that the above expression resembles the one derived, for instance, in [103, 104, 106]. However, the crucial difference is the w-dependent definition of Λ_w, Eq. (3.83). As mentioned before, its particular form enables additional simplicity and allows amicable algebraic manipulation as will be evident shortly.

Integrating out the $k_\perp$ dependence of $\psi^q_{\rm M}(x,k_\perp)$ yields the PDA,

$$f_{\rm M}\phi^q_{\rm M}(x) = \frac{1}{16\pi^3}\int d^2k_\perp \psi^q_{\rm M}\left(x,k^2_\perp\right) , \tag{4.6}$$

where $f_{\rm M}$ is the leptonic decay constant of the meson. From Eqs. (3.93) and (4.5), it is seen that the only term in the above equation that depends on $k_\perp$ is $1/\sigma_\perp^{\nu+1}$, then

$$\frac{1}{16\pi^3}\int d^2k_\perp\frac{1}{\sigma_\perp^{\nu+1}} = \frac{1}{8\pi^2}\int dk_\perp\frac{k_\perp}{(k^2_\perp+\Lambda^2_{1-2\alpha})^{\nu+1}} = \frac{1}{16\pi^2}\frac{1}{\nu\Lambda^{2\nu}_{1-2\alpha}} . \tag{4.7}$$

Combining Eqs. (4.5)-(4.7) we arrive at the following algebraic relation between $\psi_{\rm M}(x,k_\perp^2)$ and $\phi_{\rm M}(x)$:

$$\psi^q_{\rm M}(x,k_\perp^2) = 16\pi^2 f_{\rm M} \frac{\nu \Lambda_{1-2x}^{2\nu}}{(k_\perp^2+\Lambda_{1-2x}^2)^{\nu+1}} \phi^q_{\rm M}(x) \; . \tag{4.8}$$

The compact result above is a merit of the AM we have put forward. Throughout this manuscript, we shall employ dimensionless and unit normalized PDAs, $\int_0^1 dx \phi^q_{\rm M}(x) = 1$. The resulting PDA and LFWF are expressed in a quasiparticle basis at an intrinsic scale, intuitively identified with some hadronic scale, ζ_H, for which the valence degrees of freedom fully express the properties of the hadron under study. Most results herein are quoted at ζ_H (unless specified otherwise). However, for the sake of simplicity, the label ζ_H shall be omitted. It is worth reminding that the quark and antiquark PDA are connected via momentum conservation,

$$\phi^q_{\rm M}(x;\zeta_H) = \phi^{\bar{h}}_{\rm M}(1-x;\zeta_H) \; , \tag{4.9}$$

a constricted and firm connection that prevails even after evolution [41, 130, 131].

Some practical corollaries of the AM and Eq. (4.8):

- Given a particular form of $\phi^q_{\rm M}(x)$, the $\psi^q_{\rm M}(x,k_\perp^2)$ can be obtained quite straightforwardly.
- As long as we have reliable access to $\phi^q_{\rm M}(x)$, there is no actual need to construct the profile function $\tilde{\rho}^\nu(w)$ (although it can be properly identified).
- It also works the other way around. A sensible choice of $\tilde{\rho}^\nu_{\rm M}(w)$ and model parameters yields algebraic expressions for both $\phi^q_{\rm M}(x)$ and $\psi^q_{\rm M}(x,k_\perp^2)$.
- In fact, the present AM can be reduced to the toy model employed in Refs. [53, 101, 102] with appropriate substitutions. It also faithfully reproduces the results obtained from the more sophisticated *Ansatz* in Ref. [103–105].
- The degree of factorizability of the LFWF is clearly exposed through Eqs. (3.83) and (4.8).

Regarding the last point let us consider the chiral limit ($m_{\rm M} = 0$, $M_q = M_{\bar{h}}$), then $\Lambda^2_{1-2x} = M_q^2$ and

$$\psi^q_{\rm M}(x,k^2_\perp) = \left[16\pi^2 f_{\rm M} \frac{\nu M_q^{2\nu}}{(k^2_\perp + M_q^2)^{\nu+1}}\right] \phi^q_{\rm M}(x)\,. \tag{4.10}$$

The bracketed term no longer depends on x; hence, the x and $k_\perp$ dependence of $\psi_{\rm M}(x,k^2_\perp)$ has been completely factorized. Conversely, as captured by Eq. (4.8), a non-zero meson mass and quark/antiquark flavor asymmetry, namely $m^2_{\rm M} \neq 0$ and $(M^2_{\bar{h}} - M^2_q) \neq 0$, yield a LFWF which correlates x and $k^2_\perp$. So one should expect an increasingly dominant role of x and $k^2_\perp$ correlations in heavy-quarkonia and heavy-light systems. Notably, a soft Q^2-dependence might also be introduced in the definition of the PDA [132, 133], Eq. (4.6), producing the following compact expression:

$$\begin{aligned}\phi(x;Q^2) \;&=\; \left(1 - \frac{\Lambda^{2\nu}_{1-2x}}{\left[Q^2 + \Lambda^2_{1-2x}\right]^\nu}\right)\phi(x) \\ &\overset{\nu=1}{\to} \left(\frac{Q^2}{Q^2+\Lambda^2_{1-2x}}\right)\phi(x)\,.\end{aligned} \tag{4.11}$$

Clearly, $\phi(x;Q^2\to\infty) = \phi(x)$, which is the limit we take for the sake of the discussion.

4.2 Extracting the spectral density

From Eqs. (3.93), (4.4)-(4.6), it is possible to derive the relation between the PDA and the spectral density ρ_M:

$$\begin{aligned}\varphi(y) = \frac{1}{2\nu F_N}\left[\int_{-1}^{y} dw \left(\frac{1-y}{1-w}\right)^\nu + \int_y^1 dw \left(\frac{1+y}{1+w}\right)^\nu\right]\tilde{\rho}^\nu_{\rm M}(w) \\ \times \frac{[(1+y)M_q + (1-y)M_{\bar{h}}]}{\Lambda^{2\nu}_y}\,,\end{aligned} \tag{4.12}$$

where the variable $y = 1-2x$ has been introduced and we have used the definitions $\varphi(y) \equiv \phi^q_M(\frac{1}{2}(1-y))$ and $F_N = \frac{4}{3}\pi^2 f_{\rm M} n_{\rm M}$. The above integral equation can be inverted to a differential equation by differentiating three times, with respect to y, and summing up the resulting equations. This procedure yields an expression for $\rho_{\rm M}$ in terms of

derivatives of φ:

$$\eta_N \, \rho_{\rm M}(y) = \lambda_\nu^{(2)}(y)\varphi''(y) + \lambda_\nu^{(1)}(y)\varphi'(y) + \lambda_\nu^{(0)}(y)\varphi(y)\,, \tag{4.13}$$

where η_N is a normalization factor such that $\int_{-1}^{1} \rho_{\rm M}(y)dy = 1$. While the other quantities are

$$\lambda_\nu^{(2)}(y) = -\frac{1-y^2}{\chi_+}\,, \tag{4.14}$$

$$\lambda_\nu^{(1)}(y) = 2\frac{\nu y}{\chi_+} - 2\frac{\chi_-}{\chi_+^2} + \frac{\nu\chi_-}{\Lambda_y^2}\,, \tag{4.15}$$

$$\begin{aligned}\lambda_\nu^{(0)}(y) = \big\{&2\nu\chi_+^2\Lambda_y^2\left(\chi_+^2 - 2\left(1+(1-\nu)y^2+\nu\right)\Lambda_y^2\right)\\ &+4y(1-\nu)\left(2\Lambda_y^2 - \nu\chi_+^2\right)\Lambda_y^2\chi_+\chi_-\\ &-\left(\nu(1-\nu)\chi_+^4 + 2\nu\chi_+^2\Lambda_y^2 - 8\Lambda_y^4\right)\chi_-^2\big\}/\Theta_y\,,\end{aligned} \tag{4.16}$$

with the definitions $\chi_\pm = (1-y)M_{\bar h} \pm (1+y)M_q$ and $\Theta_y = -4\,(1-y^2)\,\chi_+^3\Lambda_y^4$. By setting $\nu = 1$, $\lambda_\nu^{(1,0)}$ are reduced to

$$\lambda_1^{(1)}(y) = 2\frac{y}{\chi_+} - 2\frac{\chi_-}{\chi_+^2} + \frac{\chi_-}{\Lambda_y^2}\,, \tag{4.17}$$

$$\lambda_1^{(0)}(y) = -\frac{\left(\chi_+^2 - 4\Lambda_y^2\right)\left(\chi_+^2 - \chi_-^2\right)}{2\,(1-y^2)\,\chi_+^3\Lambda_y^2}\,. \tag{4.18}$$

Furthermore, in the chiral limit:

$$\lambda_1^{(2)} = -\frac{(1-y^2)}{2M_q}\,,\ \lambda_1^{(1)} = \lambda_1^{(0)} = 0\,, \tag{4.19}$$

ensuring that our model recovers known result [110]:

$$\begin{aligned}\phi_{\rm M}^q(x) = \phi_{asy}(x) \ &= \ 6x(1-x)\\ &\iff \rho_{\rm M}(w) = \rho_{asy}(w) := \frac{3}{4}(1-w^2)\,.\end{aligned} \tag{4.20}$$

Beyond the chiral limit, but still keeping the most natural choice $\nu = 1$, the corresponding pion and kaon spectral densities are plotted in Figura 4.2. The input PDAs, parametrized according to Eqs. (4.51), are displayed in the upper panel of Figura 4.8.

Though for the purposes of this work (namely computing LFWFs, GPDs and distributions derived therefrom) the determination of $\rho_{\rm M}$ is not required at all, it is worth

stressing that the AM we have introduced enables a straightforward derivation of the spectral density from the prior knowledge of the PDA, thus avoiding the need of assuming a particular *ad hoc* representation for $\rho_{\rm M}$. This shall be useful for future explorations that require the explicit knowledge of the BSWF, and hence of the spectral density.

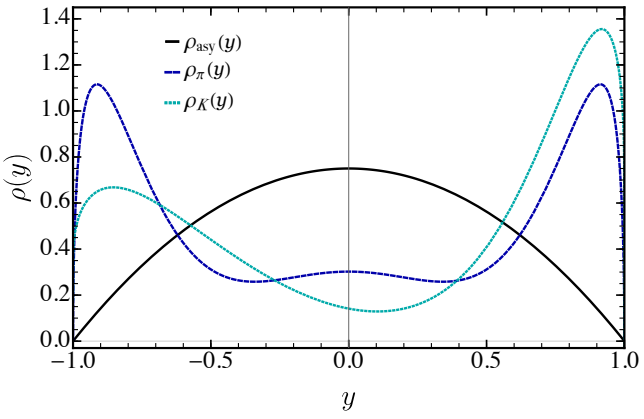

FIGURE 4.2: Spectral density for the pion (dashed-blue line), the kaon (dashed-cyan line) and the one produced by $\phi_{asy}(x)$ in the chiral limit. We fix $\nu = 1$ for the three cases. The parameters chosen correspond to the ones in Table 4.1.

In the next section, we shall exploit the virtues of Eq. (4.8) to compute the pseudo-scalar meson GPDs in the overlap representation.

4.3 Sketching the pseudo-scalar mesons 3D structure

4.3.1 GPDs

Remembering the Eq. (2.26) in Chapter 2, the valence quark GPD can be obtained from the overlap representation of the LFWF [48]:

$$H^q_{\rm M}(x,\xi,t) = \int \frac{d^2k_\perp}{16\pi^3} \psi^{q*}_{\rm M}\left(x^-,(\mathbf{k}^-_\perp)^2\right)\psi^q_{\rm M}\left(x^+,(\mathbf{k}^+_\perp)^2\right) ,$$
$$x^\pm = \frac{x\pm\xi}{1\pm\xi} \quad , \quad \mathbf{k}^\pm_\perp = k_\perp \mp \frac{\Delta_\perp}{2}\frac{1-x}{1\pm\xi} . \tag{4.21}$$

We now work out the expression for the valence quark GPD in detail by substituting Eq. (4.8) in Eq. (2.26) remembering all the kinematic in the DGLAP region

$$H^q_{\rm M}(x,\xi,t) = (16\pi^2 f_{\rm M}\nu)^2 \phi^q_{\rm M}(x^+)\phi^q_{\rm M}(x^-)\Lambda^{2\nu}_{1-2x^+}\Lambda^{2\nu}_{1-2x^-} \times \int \frac{d^2k_\perp}{16\pi^3}\frac{1}{((\mathbf{k}^-_\perp)^2+\Lambda^2_{1-2x^-})^{\nu+1}}\frac{1}{((\mathbf{k}^+_\perp)^2+\Lambda^2_{1-2x^+})^{\nu+1}} \,. \tag{4.22}$$

As usual, integration on $k_\perp$ can be performed by introducing Feynman parametrization and a suitable change of variables, such that the integral in Eq. (4.22) becomes

$$\frac{2\pi}{16\pi^3}\frac{\Gamma(2\nu+2)}{\Gamma^2(\nu+1)}\int_0^1 du u^\nu(1-u)^\nu \int_0^\infty dk_\perp \frac{k_\perp}{(k^2_\perp+\mathbb{M}^2(u))^{2\nu+2}} = \frac{1}{16\pi^2}\frac{\Gamma(2\nu+1)}{\Gamma^2(\nu+1)}\int_0^1 du \frac{u^\nu(1-u)^\nu}{[\mathbb{M}^2(u)]^{2\nu+1}} \,, \tag{4.23}$$

where the function $\mathbb{M}^2(u)$ depends on the model parameters, as well as the kinematic variables $x,\ \xi,\ t$. It acquires the form $\mathbb{M}^2(u) = c_2u^2 + c_1u + c_0$, where

$$\begin{aligned} c_2 &= \frac{(1-x)^2}{(1-\xi^2)^2}t \,, \\ c_1 &= -\frac{(1-x)^2}{(1-\xi^2)^2}t + \Lambda^2_{1-2x^+} - \Lambda^2_{1-2x^-} \,, \\ c_0 &= \Lambda^2_{1-2x^-} \,. \end{aligned} \tag{4.24}$$

Thus the GPD can be conveniently expressed as

$$H^q_{\rm M}(x,\xi,t) = \mathcal{N}\phi^q_{\rm M}(x^+)\phi^q_{\rm M}(x^-)\Lambda^{2\nu}_{1-2x^+}\Lambda^{2\nu}_{1-2x^-}\frac{\Gamma(2\nu+2)}{\Gamma^2(\nu+1)}\int_0^1 du\frac{u^\nu(1-u)^\nu}{[\mathbb{M}^2(u)]^{2\nu+1}} \,. \tag{4.25}$$

Notice that, in the chiral limit, $\mathbb{M}^2(u)$ reduces to

$$\mathbb{M}^2(u) = -t\,u(1-u)\frac{(1-x)^2}{(1-\xi^2)^2} + M_q^2 \,, \tag{4.26}$$

and so the integration on du in Eq. (4.25) can be carried out algebraically for specific values of $\nu > -1$. In particular, $\nu = 1$ recovers the results in [53–55, 101, 102]. Beyond

the chiral limit, an algebraic expression is found for $t = 0$:

$$H^q_{\rm M}(x,\xi,0) = \mathcal{N}\phi^q_{\rm M}(x^+)\phi^q_{\rm M}(x^-)\frac{\Lambda^{2\nu}_{1-2x^+}}{\Lambda^{2\nu}_{1-2x^-}}\frac{\Gamma(2\nu+2)}{\Lambda^2_{1-2x^-}} \times {}_2\tilde{F}_1\left(1+\nu, 1+2\nu, 2\nu+2, 1-\frac{\Lambda^2_{1-2x^+}}{\Lambda^2_{1-2x^-}}\right), \tag{4.27}$$

where ${}_p\tilde{F}_q(u,v,w,z)$ is the regularized hypergeometric function. Conversely, taking $\xi = 0$, an expansion of $\mathbb{M}^2(u)$ around $-t \approx 0$ yields an algebraic solution for Eq. (4.25):

$$H^q_{\rm M}(x,0,t) \overset{t\to 0}{\approx} \mathcal{N}\frac{[\phi^q_{\rm M}(x)]^2}{\Lambda^2_{1-2x}}\left[1 - c^{(1)}_\nu (1-x)^2\left(\frac{-t}{\Lambda^2_{1-2x}}\right) + ...\right], \tag{4.28}$$

$$c^{(1)}_\nu = \frac{(1+\nu)(1+2\nu)}{2(3+2\nu)}, \quad \mathcal{N} = \left[\int_0^1 dx\, \frac{\phi^2_{\rm M}(x)}{\Lambda^2_{1-2x}}\right]^{-1}.$$

In the next section we will focus on the *forward limit* of the GPD ($t = 0$, $\xi = 0$) which defines the valence quark PDF. For the time being, we can make an insightful connection with light-front holographic QCD (LFHQCD) approach Ref. [134, 135], recalling the following representation for the zero-skewness valence quark GPD therein:

$$H^q_{\rm M}(x,0,t) = q_{\rm M}(x)\,\exp[t\hat{f}^q_{\rm M}(x)], \tag{4.29}$$

where $\hat{f}^q_{\rm M}$ is some profile function to be determined. An expansion around $-t \approx 0$ of this expression, and a subsequent comparison with Eq. (4.28), enable us to identify

$$\hat{f}^q_{\rm M}(x) = \frac{c^{(1)}_\nu (1-x)^2}{\Lambda^2_{1-2x}}. \tag{4.30}$$

The parametric representation of the GPD in Eq. (4.29) provides a fair approximation of the zero-skewness GPD in Eq. (4.25) except for intermediate values of momentum transfer. It is also useful in extracting insights concerning the IPS-GPDs, as will be addressed below.

We now proceed to discuss the derivation of PDFs, FFs and IPS-GPDs, as inferred from the knowledge of the GPDs in the DGLAP kinematic region.

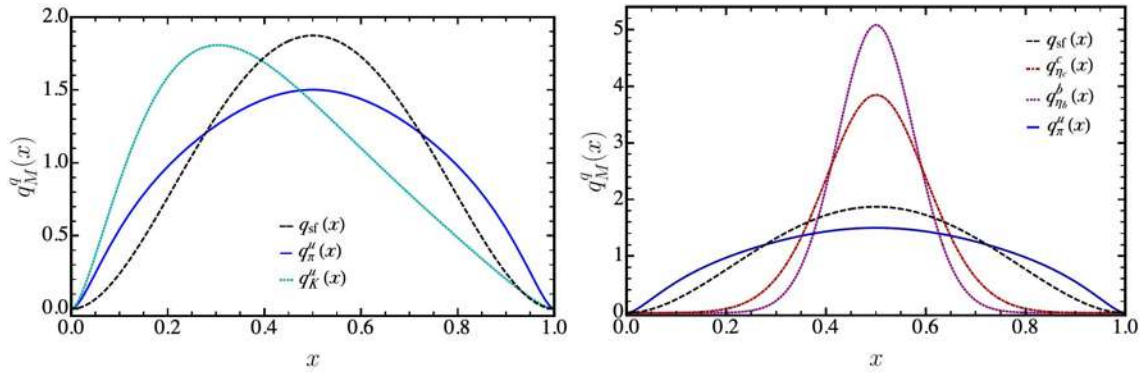

FIGURE 4.3: Valence quark PDFs at ζ_H. Left panel- The solid (blue) line corresponds to valence quark PDF of pion and the dotted (cyan) line corresponds to the valence light-quark PDF in kaon. Right panel- The dot-dashed (red) line corresponds to the valence quark PDF of η_c, the dotted (purple) line corresponds to valence quark PDF of η_b, again the solid (blue) line corresponds to the valence quark PDF of pion. For all these panels, the dashed (black) line corresponds to the parton like profile $q_{sf}(x) = 30x^2(1-x)^2$.

4.3.2 PDFs

The first term of the Taylor expansion in Eq. (4.28) corresponds to the valence quark PDF, namely

$$q_{\rm M}(x) \equiv H^q_{\rm M}(x,0,0) = \mathcal{N}\frac{[\phi^q_{\rm M}(x)]^2}{\Lambda^2_{1-2x}}\,, \tag{4.31}$$

where $q_{\rm M}(x)$ is unit normalized. Recalling that the distributions have been derived at ζ_H, the corresponding antiquark PDF is simply obtained as

$$\bar{h}_{\rm M}(x;\zeta_H) = q_{\rm M}(1-x;\zeta_H)\,. \tag{4.32}$$

Furthermore, the factorization properties of the LFWF in the chiral limit yields the simple relation:

$$q_{\rm M}(x;\zeta_H) = \frac{[\phi^q_{\rm M}(x;\zeta_H)]^2}{\int_0^1 dx\,[\phi^q_{\rm M}(x;\zeta_H)]^2}, \tag{4.33}$$

thus stressing that the degree of factorizability of the AM is manifest via the quantity Λ^2_{1-2x}. As long as we have $m^2_{\rm M} \approx 0$ and also $(M_h^2 - M_q^2) \approx 0$, a factorized LFWF will produce sensible results. This is the case of the SDE results from Refs. [126, 127], in which Eq. (4.33) was employed to compute the kaon PDF from its PDA. For the purpose of this work, factorizability will not be assumed and we shall consider the more

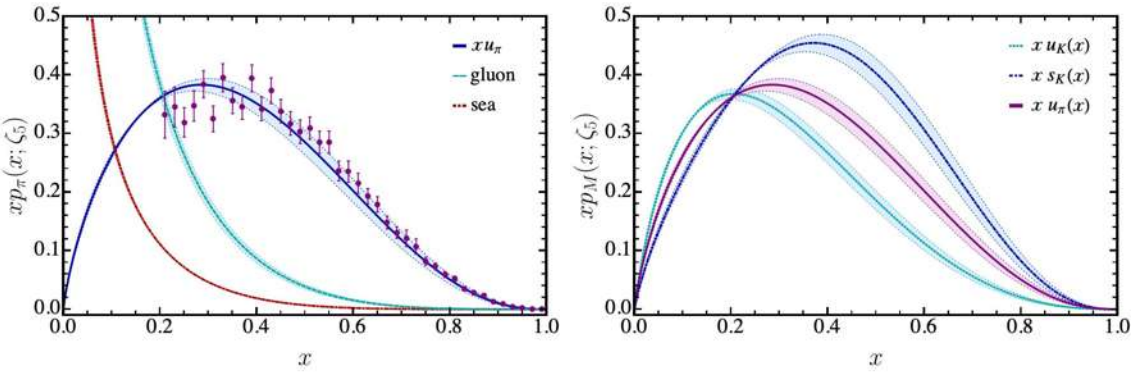

FIGURE 4.4: Evolved PDFs at $\zeta_5 := 5.2$ GeV. Left panel- The plots correspond to the evolved pion PDF. The solid blue line corresponds to the u valence-quark, the dashed cyan line corresponds to the gluon contribution and the dot-dashed red line corresponds to sea contribution. The data from [136], is rescaled according to the ASV analysis in [137]. Right panel- The dotted cyan line corresponds to u-in-K valence-quark PDF, the dot-dashed blue line is the analogous for the $\bar{s}$ quark and the solid purple line corresponds to the u valence-quark in the pion. The error bands account for the variation of the initial scale, $\zeta_H = 0.33\,(1 \pm 0.1)$ GeV.

general case, Eq. (4.31). The set of relations described in this Section also shows that if the input PDA behaves like $\phi(x \to 1) \sim (1-x)$ (as prescribed by QCD, [130]), the PDF will exhibit the large-x behavior $q_{\rm M}(x;\zeta_H) \sim (1-x)^2$. Finally, it is worth recalling that neither Eq. (4.33) nor Eq. (4.32) remain valid for $\zeta > \zeta_H$, due to the evolution equations obeyed by the PDFs [42, 43, 138, 139].

All distributions described so far have been obtained from the LFWF at the hadron scale, ζ_H; as described before, at this low-energy scale, the fully dressed quasiparticles (valence-quarks) express all hadron properties. This is also the case of the valence-quark PDF which, computed at ζ_H, entails that all the hadron's momentum is carried by the fully-dressed valence quarks. From the experimental point of view, the access and interpretation of PDFs and GPDs at ζ_H imply certain technical and conceptual complications [140]; only above certain energies, typically the mass of the proton, parton distributions can be properly extracted. In particular, experimental data for the case of the pion is only available at $\zeta = \zeta_5 := 5.2$ GeV [137, 141] (the same for the $u_K(x)/u_\pi(x)$ ratio [142]), whereas $\zeta = \zeta_2 := 2$ GeV is a typical scale for lattice QCD and phenomenological fits [143–145]. To produce a consistent picture when evolving the hadronic scale PDF, we shall follow the all orders scheme introduced in Refs. [124–127, 146] for pion and kaon PDFs, extended to their GPDs in Ref. [103, 104], and employed recently in the calculation of the proton PDFs as well [147]. This

scheme is based upon the assumption that an effective charge $\hat{\alpha}$ allows all beyond leading-order effects to be absorbed within it, thus arriving at a leading-order-like DGLAP evolution equation. Notably, if the evolution is performed via the computation of several Mellin moments, it is not necessary to specify the pointwise behavior of the effective charge [104] (assuming its existence would be sufficient). To evolve the distributions directly, the exercise we carry out in this section, we take $\hat{\alpha}$ from Ref. [127], which implies setting $\zeta_H = 0.33(1\pm0.1)$ GeV. In Section V, we present numerical results for evolved pion and kaon PDFs for specific model inputs described therein.

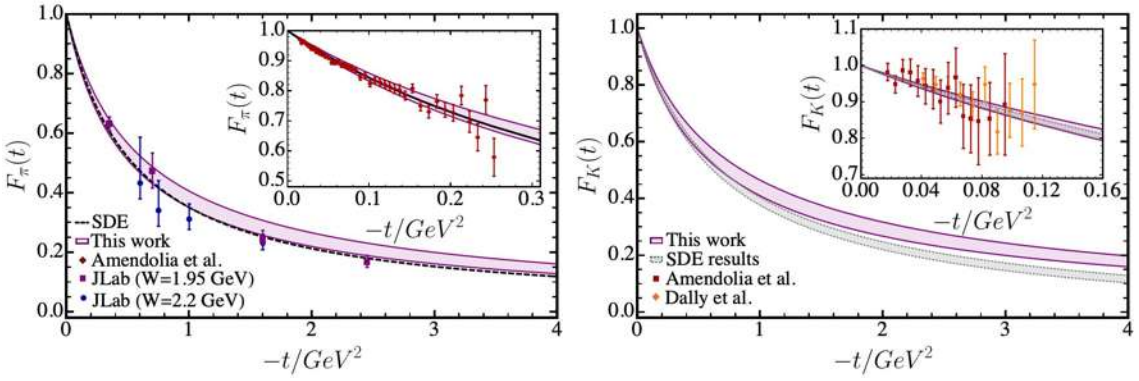

FIGURE 4.5: Pion and kaon electromagnetic FFs. Left panel- The (purple) band represents our pion results with the model parameters described in Section V. The band width accounts for a 5% variation of the benchmark charge radius in Table 1. Dashed (black) line is the SDE result for the pion [110]. Right panel- It shows analogous results for the kaon FF. Diamonds, rectangles and circles represent the experimental data from Refs. [11, 13, 14]. Lower (gray) band is the SDE result for the kaon [148].

4.3.3 EFFs

The contribution of the q quark to the meson's elastic electromagnetic form factor (EFF) is obtained from the zeroth moment of the GPD:

$$F^q_{\rm M}(t) = \int_{-1}^{1} dx\; H^q_{\rm M}(x,\xi,t), \tag{4.34}$$

an analogous expression holds for the antiquark $\bar{h}$, such that the complete meson EFF reads

$$F_{\rm M}(t) = e_q F^q_{\rm M}(t) + e_{\bar{h}} F^{\bar{h}}_{\rm M}(t)\ , \tag{4.35}$$

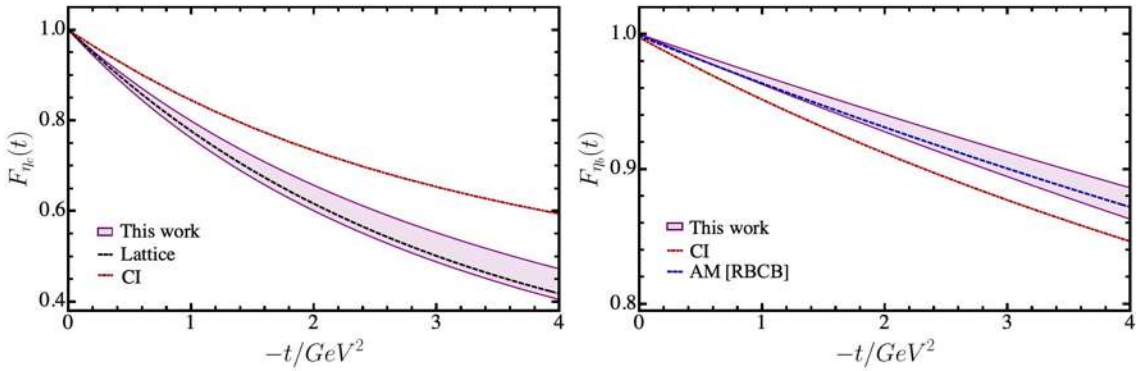

FIGURE 4.6: η_c and η_b electromagnetic FFs. Left panel- The purple band represents our η_c results with the model parameters described in Section V. The band width accounts for a 5% variation of the benchmark charge radius in Table 1. Right panel- Analogous results for η_b. For comparison, we have included lattice QCD results from Refs. [149, 150], as well as SDE-driven predictions in the contact interaction (CI) model and a former algebraic model for heavy quarkonia [85, 99].

where $e_{q,\bar{h}}$ are the valence-constituent quarks electric charges in units of the positron charge. Due to polynomiality properties of the GPD, the EFF does not depend on ξ, therefore one can simply take $\xi \to 0$:

$$F^q_{\rm M}(t) = \int_0^1 dx\; H^q_{\rm M}(x,0,t)\;. \tag{4.36}$$

A Taylor expansion around $t \approx 0$ yields to the Eq. (2.13)

$$F^q_{\rm M}(t) \overset{t\to 0}{\approx} 1 - \frac{(r^q_{\rm M})^2}{6}(-t) + \dots\;, \tag{4.37}$$

$$(r^q_{\rm M})^2 \;=\; -6\frac{dF^q_{\rm M}(t)}{dt}\bigg|_{t=0}\;, \tag{4.38}$$

where $r^q_{\rm M}$ denotes the contribution of the quark q to the meson charge radius, $r_{\rm M}$. Comparing the above equations with the integration of Eq. (4.28) on x, one obtains a semi-analytical expression for $r^q_{\rm M}$:

$$(r^q_{\rm M})^2 = 6\int_0^1 dx\; \hat{f}^q_{\rm M}(x) q_{\rm M}(x)\;, \tag{4.39}$$

showing the charge radius is tightly connected with the hadronic scale PDF (and thus with the corresponding PDA). The antiquark result is obtained analogously. This

contribution to $r_{\rm M}$ reads:

$$(r_{\rm M}^{\bar{h}})^2 = 6 \int_0^1 dx\ \hat{f}_{\rm M}^{\bar{h}}(x) q_{\rm M}(1-x)\ , \tag{4.40}$$

where $\hat{f}_{\rm M}^{\bar{h}}(x)$ is defined in analogy to its quark counterpart in Eq. (4.30),

$$\hat{f}_{\rm M}^{\bar{h}}(x) = \frac{c_\nu^{(1)}(1-x)^2}{\Lambda_{2x-1}^2}\ . \tag{4.41}$$

Summing up the quark and antiquark contributions, the meson charge radius reads:

$$r_{\rm M}^2 = e_q (r_{\rm M}^q)^2 + e_{\bar{h}} (r_{\rm M}^{\bar{h}})^2\ . \tag{4.42}$$

Clearly, in the isospin symmetric limit, $e_q + e_{\bar{h}} = 1$ yields $F_{\rm M}(t) = F_{\rm M}^q(t)$ and so $r_{\rm M} = r_{\rm M}^q$. For the neutral pseudo-scalars, in the isospin symmetric limit, $e_q + e_{\bar{h}} = 0$ implies $F_{\rm M}$ would be strictly zero, producing $r_{\rm M} = 0$; thereby we focus only on the individual flavor contribution ($F_{\rm M} \to F_{\rm M}^q$) in such cases (*e.g.* heavy quarkonia). Finally, note that if the charge radius is known, then Eqs. (4.39- 4.42) can be employed to fix the model parameters.

4.3.4 Impact parameter space GPD

The IPS-GPD can be obtained straightforwardly by carrying out the Fourier transform of the zero-skewness GPD, $H_{\rm M}^q(x,0,t)$:

$$u_{\rm M}(x, b_\perp^2) = \int_0^\infty \frac{d\Delta}{2\pi} \Delta J_0(b_\perp \Delta) H_{\rm M}^u(x,0,t), \tag{4.43}$$

where J_0 is the cylindrical Bessel function. This distribution is interpreted as the probability density of finding a parton with momentum fraction x at a transverse distance $b_\perp$ from the centre of transverse momentum of the meson under study. It is extracted in its totality by the GPD's properties in the DGLAP region. Exploiting the representation of the GPD from Eq. (4.29), we can obtain an analytic expression:

$$u_{\rm M}^q(x, b_\perp^2) = \frac{q_{\rm M}(x)}{4\pi \hat{f}_{\rm M}^q(x)} \exp\left[-\frac{b_\perp^2}{4\hat{f}_{\rm M}^q(x)}\right]\ . \tag{4.44}$$

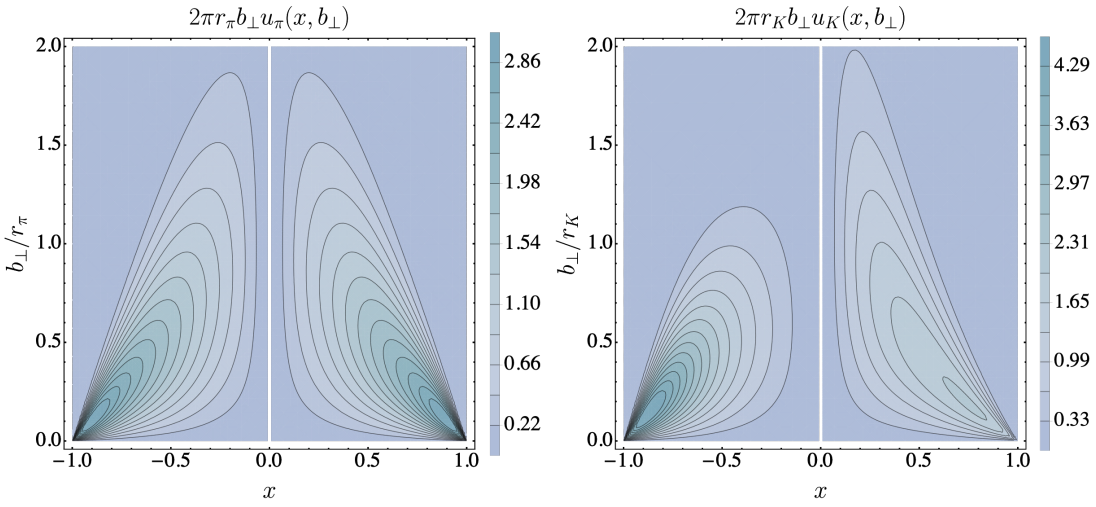

FIGURE 4.7: Impact parameter space GPDs. The quark lies in the $x > 0$ domain, while the antiquark in $x < 0$. Left panel- pion results using the inputs from Section V. Right panel- analogous results for the kaon. The conspicuous asymmetry in this case is due to the larger s-quark mass: the s-quark plays a larger role in determining the center of transverse momentum.

Containing an explicit dependence on the PDF, Eq. (4.44) reveals a clear interrelation between the momentum and spatial distributions. In fact, the PDF is recovered from

$$q_{\rm M}(x) = 2\pi \int_0^\infty db_\perp \, b_\perp q(x, b_\perp) \, . \tag{4.45}$$

Furthermore, considering the mean-squared transverse extent (MSTE),

$$< b_\perp^2(x) >_{\rm M}^q \; = \; \frac{1}{r_{\rm M}} \int_0^\infty db_\perp \, \mathbf{b}_{\rm M}^q(x, b_\perp) \, b_\perp^2 \, , \tag{4.46}$$

$$\mathbf{b}_{\rm M}^q(x, b_\perp) := 2\pi r_{\rm M} b_\perp u_{\rm M}^q(x, b_\perp) \, . \tag{4.47}$$

the IPS-GPD defined in Eq. (4.44) yields the plain relation:

$$< b_\perp^2(x) >_{\rm M}^q = 4 \int_0^1 dx \, \hat{f}_{\rm M}^q(x) q_{\rm M}(x) \, . \tag{4.48}$$

Integrating over x, and comparing with Eq. (4.42), one is left with a compact expression for the expectation value:

$$< b_\perp^2 >_{\rm M}^q = \frac{2}{3} r_{\rm M}^2 \left[\frac{(r_{\rm M}^q)^2}{e_q (r_{\rm M}^q)^2 + e_{\bar{h}} (r_{\rm M}^{\bar{h}})^2} \right] \; ; \tag{4.49}$$

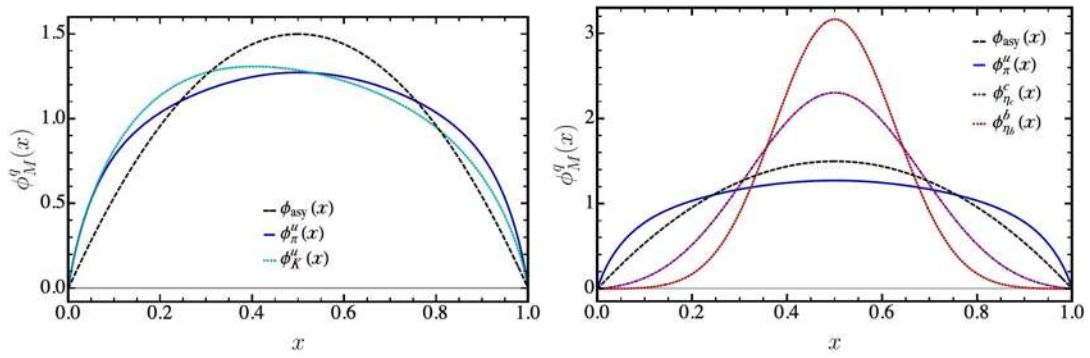

FIGURE 4.8: Left panel- pion and kaon PDAs at ζ_H. Right panel- the corresponding ones for η_c and η_b. The distributions were obtained within the SDE formalism in Refs. [82, 127], and parameterized according to Eqs. (4.51). For comparison, the asymptotic distribution, $\phi_{asy}(x) = 6x(1-x)$, is also shown.

i.e. the expectation value of the MSTE of the valence quark is directly correlated with the meson charge radius. In the isospin symmetric limit, the following expected result [103, 104] is recovered:

$$< b_\perp^2 >_{\rm M}^q = \frac{2}{3} r_{\rm M}^2 \, . \tag{4.50}$$

Interestingly, in the chiral limit, all the algebraic expressions form this Section, valid only at ζ_H, become plainly analogous to those from the factorized *Gaussian model* in [103, 104].

In the following section we shall provide a collection of results for the distributions discussed so far, using SDE predictions as model inputs.

4.4 Computed distributions

Now that we have shown a variety of algebraic results for different distributions of partons (and some other quantities), we will particularize the inputs of the AM. The starting point is Eq. (4.8), which directly relates the leading-twist LFWF with the PDA such that, with the prior knowledge of $\phi^q_{\rm M}(x)$, the LFWF is derived straightforwardly; the produced physical picture would be valid at ζ_H. Given the robustness of the SDE formalism to compute PDAs, we shall employ predictions obtained within this framework as model inputs [82, 127]. The specific set of PDAs we consider is the

following ($\bar{x} = 1 - x$):

$$\begin{aligned}
\phi_\pi^u(x) &= 20.226\, x\bar{x}\,[1 - 2.509\sqrt{x\bar{x}} + 2.025 x\bar{x}]\,, \\
\phi_K^u(x) &= 18.04\, x\bar{x}\,[1 + 5x^{0.032}\bar{x}^{0.024} - 5.97 x^{0.064}\bar{x}^{0.048}]\,, \\
\phi_{\eta_c}^c(x) &= 9.222\, x\bar{x}\exp\left[-2.89(1 - 4x\bar{x})\right]\,, \\
\phi_{\eta_b}^b(x) &= 12.264\, x\bar{x}\exp[-6.25(1 - 4x\bar{x})]\,.
\end{aligned} \tag{4.51}$$

The expressions above properly capture our contemporary knowledge of such distri-

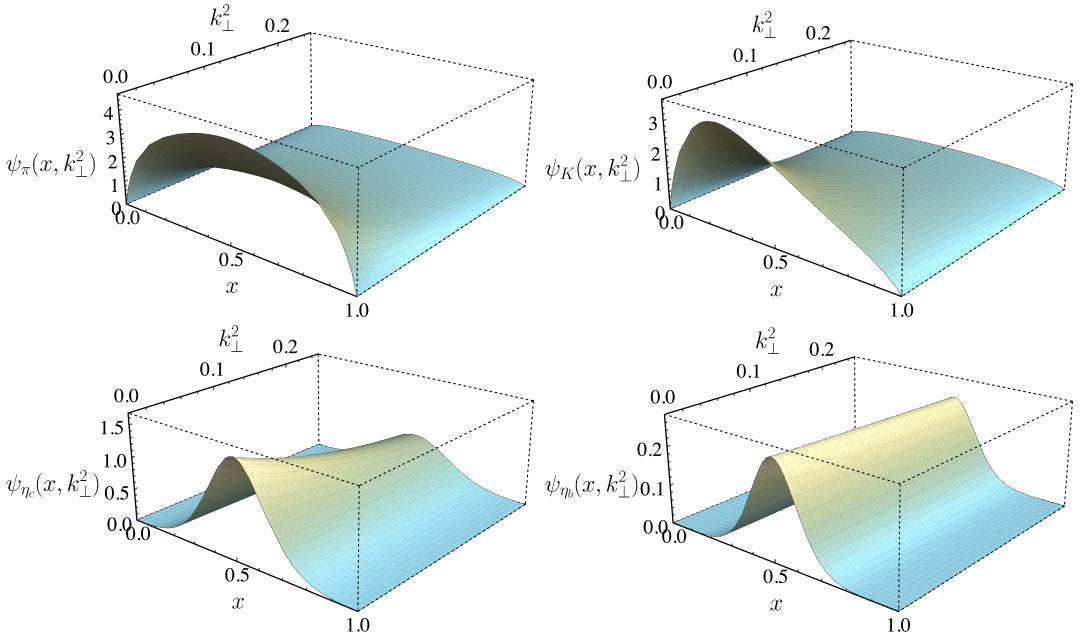

FIGURE 4.9: LFWFs of the pion, kaon, η_c and η_b obtained from Eq. (4.8) and the inputs described in Section V. Herein we have depicted $\psi_{\rm M}(x, k_\perp^2) \to \psi_{\rm M}(x, k_\perp^2)/(16\pi^2 f_{\rm M})$. Mass units in GeV.

butions, namely, the soft endpoint behavior and the dilation/compression with respect to the asymptotic distribution [130]:

$$\phi_{asy}(x) = 6x(1 - x)\,. \tag{4.52}$$

As can be seen in Fig. 4.8, pion and kaon PDAs are dilated with respect to $\phi_{asy}(x)$, while those containing heavy quarks are narrower. As noted for the kaon, the asymmetry between the s and u-quark masses produces a skewed distribution, while the rest of the PDAs are symmetrical.

The remaining ingredients are the parameter ν and the constituent masses M_q. Regarding the former, $\nu = 1$ is a natural choice since it yields the correct asymptotic behavior of the BSWF [117]. Concerning the values of the constituent masses, we shall employ available experimental [151], SDE [110, 120–122, 152] and lattice QCD [149, 150] results on the charge radii as benchmarks, and determine M_q via Eq. (4.42). Table 4.1 collects the constituent quark masses that define our AM and the corresponding charge radii.

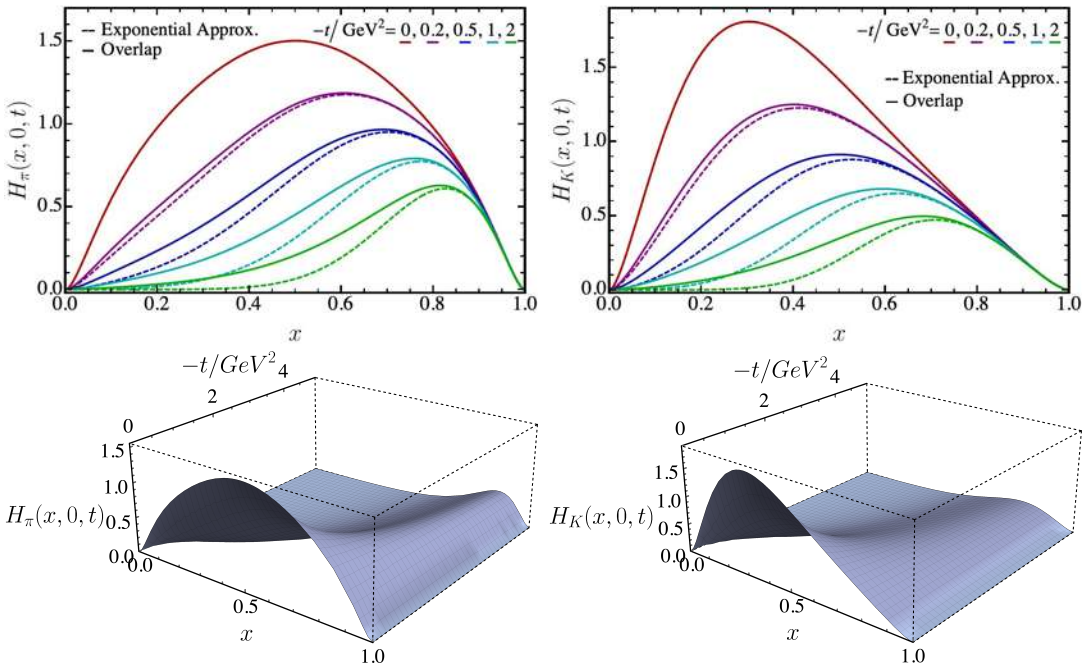

FIGURE 4.10: Zero-skewness valence quark GPDs for pion (left) and kaon (right), employing the model inputs described in Section 4.4. Upper panel- A comparison between the GPDs obtained directly from Eq. (4.25) (solid lines) and those produced by the algebraic representation in Eq. (4.29) (dashed lines). Lower panel- Equivalent three-dimensional picture, resulting from Eq. (4.25). Mass units in GeV.

TABLE 4.1: Model inputs: meson and quark masses (in GeV). M_q values are fixed via Eq. (4.42) using the quoted charge radii. In the case of η_c and η_b, we quote $r_{\mathrm{M}}^q = r_{\mathrm{M}}^{\bar{h}}$ rather than r_{M}, which is strictly zero. The list of distribution amplitudes entering the relevant equations are found in Eq. (4.51).

Meson	m_{M}	r_{M} (in fm)	Quark	M_q
π^+	0.14	0.659 [110, 151]	u	0.317
K^+	0.49	0.600 [120–122]	s	0.574
η_c	2.98	0.255 [149, 150]	c	1.65
η_b	9.39	0.088 [152]	b	5.09

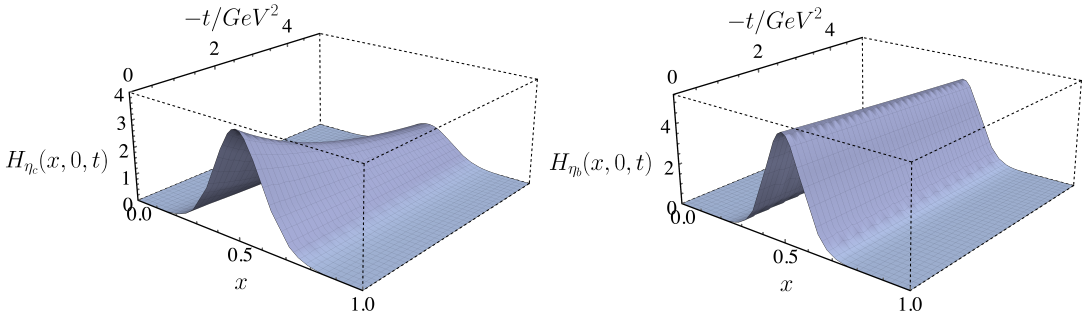

FIGURE 4.11: Valence quark GPDs obtained from Eq. (4.25) for $\xi = 0$ employing the model inputs described in Section 4.4. Left panel- η_c GPD. Right panel- η_b GPD. Mass units in GeV.

With the AM fully determined, the produced LFWFs are shown in Fig. 4.9. It is clear that the heavier mesons exhibit a much slower damping as $k_\perp^2$ increases. Furthermore, just as the PDAs, the LFWFs as a function of x are found to be more compressed in this case.

The valence-quark GPDs are then obtained appealing to the overlap representation of the LFWF, Eqs. (2.26,4.25). Pion and kaon results are shown in the bottom panel of Figure 4.10, while those of η_c and η_b can be found in Figure 4.11. The GPDs for the heavier mesons naturally have a narrower profile along the x-axis and are harder along the $-t$-axis. Moreover, the upper panel of Figure 4.10 also displays a comparison between the GPDs obtained directly from Eq. (4.25) and the approximate representation of (4.29). The derived valence quark PDFs are found in Figure 4.3. As one would expect from Eq. (4.31), the characteristic features exhibited by the PDAs, of dilation and narrowness, are filtered into PDFs. To emphasize it, we notice that the plots in the above mentioned figure display the scale-free parton-like profile

$$q_{sf}(x) = 30x^2(1-x)^2 \,. \tag{4.53}$$

Given our preferred value $M_s \approx 1.8\, M_u$, the s-in-K momentum fraction at the hadronic scale is $< x;\zeta_H >_K^s = 0.55$, about 4% larger than typical values [126, 127]. The pion and kaon PDFs are then evolved from the hadronic scale, $\zeta_H = 0.33(1 \pm 0.1)$ GeV, to the experimentally accessible scale of $\zeta_5 := 5.2$ GeV. The evolution procedure is detailed, for instance, in Refs. [104, 146]. Fig. 4.4 displays the outcome. In the top panel of this figure, the valence quark as well as gluon and sea quark pion PDFs are shown. At the evolved scale, we find typical values of momentum fraction distribution in pion [126, 127]: $< x;\zeta_H >_\pi^{\rm val} = 0.41(4)$, $< x;\zeta_H >_\pi^{\rm sea} = 0.14(2)$, $< x;\zeta_H >_\pi^{\rm glue} = 0.45(3)$.

The bottom panel of Fig. 4.4 compares the valence quark PDFs in pion and kaon. Then again, our choice of M_s produces a slightly larger momentum fraction for the s valence-quark at such scale, $< x; \zeta_5 >_K^s = 0.25$, and a smaller one for the u quark, $< x; \zeta_5 >_K^u = 0.17$. Concerning the large-$x$ exponents of the valence quark distributions, we find that

$$u_{\pi,K}(x \to 1; \zeta_5) \sim (1-x)^{\beta_{eff}} \ , \ \beta_{eff} \approx 2.8, \tag{4.54}$$

where β_{eff} must be interpreted as an effective exponent rather than that obtained from the known evolution equations of $\beta(\zeta_H)$ [127, 153]. Moreover, the x-domain of applicability and interpretation of $\beta(\zeta_H)$ is not without its ambiguities and requires special care [154]. The electromagnetic FFs are displayed in Figs. (4.5, 4.6). As can be noted therein, pion and kaon FFs agree with the available experimental data [11, 13, 14] and previous SDE calculations [110, 148]. The η_c FF is compared with lattice QCD [149, 150] and SDE results in the contact interaction (CI) model [99]. Similarly, the η_b result is contrasted with CI model results and with previous determinations with an AM for heavy quarkonia [85]. Both η_c and η_b form factors show a satisfactory compatibility with earlier reliable predictions.

The IPS-GPDs are derived from the approximate LFHQCD-inspired parametrization of the GPD, introduced in [135] and quoted in Eq. (4.29). For illustrative purposes, we have considered the convenient representation of Eq. (4.47), which produces the pion and kaon results shown in Fig. 4.7. The quark region is identified with $x > 0$, while the antiquark lies in the $x < 0$ domain. The symmetry in the pion case is a natural consequence of the isospin symmetry, whereas the contraction on the s-in-K distribution is a result of M_s being larger than M_u. In fact, as the constituent quark mass becomes larger, it is expected that the quark plays an increasingly major role in determining the center of transverse momentum; furthermore, the distributions become narrower and the maximums become larger. Given the compact representation of the IPS-GPDs, the values $(x^{\max}, b_\perp^{\max})_{\rm M}^q$ where $\mathbf{b}_{\rm M}^q(x, b_\perp)$ acquires its global maximum, can be readily identified:

$$b_\perp^{\max} = \sqrt{2\hat{f}_{\rm M}^q(x^{\max})} \ , \tag{4.55}$$

and $x^{\max}$ is the real-valued solution of

$$q_{\rm M}(x) f'(x) - 2q'_{\rm M}(x) f(x) = 0 \ . \tag{4.56}$$

It is thus clear that a constant PDF yields the point particle limit $(|x^{\max}|, b_\perp^{\max})_{\rm M}^q \to$

$(1, 0)$. The location of the maximum and its value are reported in Table 4.2 for different mesons. Finally, according to Eq. (4.49) and our model inputs, we report the expectation values of the MSTE for the kaon:

$$< b_\perp^2 >_{\rm M}^u = 0.76\, r_K^2 \ , \ < b_\perp^2 >_{\rm M}^s = 0.47\, r_K^2 \ ; \tag{4.57}$$

while for the heavy quarkonia and pion in isospin symmetric case we can infer the result from Eq. (4.50).

TABLE 4.2: Global maximum $\mathcal{I}_{\rm M}^q := \max[\mathbf{b}_M^q(x, b_\perp)]$ and its location $(x^{\rm max}, b_\perp^{\rm max}/r_{\rm M})$.

Meson	$(x^{\rm max}, b_\perp^{\rm max}/r_{\rm M})_{\rm M}^q$	$\mathcal{I}_{\rm M}^q$	$(x^{\rm max}, b_\perp^{\rm max}/r_{\rm M})_{\rm M}^h$	$\mathcal{I}_{\rm M}^h$
π	(0.90, 0.10)	3.19	(-0.90, 0.10)	3.19
K	(0.76, 0.18)	2.03	(-0.88, 0.14)	4.79
η_c	(0.53, 0.56)	3.99	(-0.53, 0.56)	3.99
η_b	(0.52, 0.60)	4.90	(-0.52, 0.60)	4.90

For the pion and kaon, one can visually verify these tabulated results in Fig. (4.7). This completes the presentation of computed results.

Chapter 5

The triangle diagram approximation

The calculation of the EFF and TFF of scalar and pseudoscalar mesons can also be developed by using the triangle diagram approximation, which requires the knowledge of some ingredients previously seen in Chapter 3 such as the dressed quark propagator, the Bethe-Salpeter amplitude and the quark-photon vertex. Once these elements are known, the standard application of Feynman rules to the MγM−vertex is implemented in order to compute EFF and γMγ for the determination of TFF. First, we perform the calculation using CI and then compare using the AM.

5.1 The EFFs in the triangle diagram approach

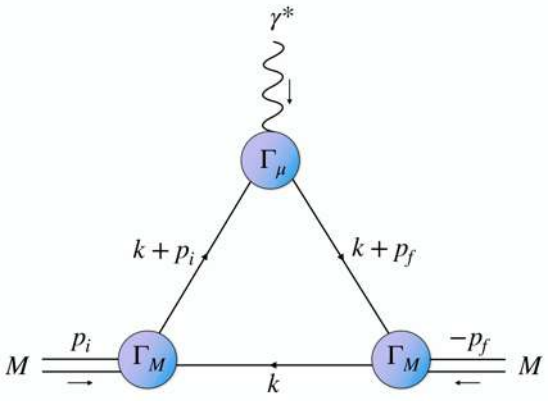

FIGURE 5.1: Triangle diagram of the EFF in an impulse approximation of a MγM vertex.

Considering the previous ingredients, we can now proceed to the analytic computation of the EFF and TFF in the AM. In order to compute the EFF of a meson we consider the diagram in Figure 5.1 which represents the interaction between a meson and a photon.

Accordingly, the contribution of the direct interaction between the photon and the quark q to the EFF is given by

$$K_\mu F_{\rm M}^q(Q^2) = N_c \,{\rm tr} \int \frac{d^4k}{(2\pi)^4} \chi_\mu^q(k+p_f, k+p_i)\Gamma_{\rm M}(k_i,p_i) S_{\bar{h}}(k) \Gamma_{\rm M}(k_f,p_f)\,, \qquad (5.1)$$

where Q is the incoming photon momentum and the remaining trace is over spinor indices. Furtheremore, the incoming and outgoing meson momentum are denoted by $p_{f,i} = K \pm Q/2$, while the relative moments of the quark-meson-antiquark vertex are $k_{f,i} = k + p_{f,i}/2$, such that $K \cdot Q = 0$ and $p_{f(i)}^2 = K^2 + Q^2/2 = -m_M^2$. Hence, the total EFF of the meson would be,

$$F_{\rm M}(Q^2) = e_q F_{\rm M}^q(Q^2) + e_{\bar{h}} F_{\rm M}^{\bar{h}}(Q^2)\,, \qquad (5.2)$$

where, $e_{q(\bar{h})}$ is the quark(antiquark) electric charge [1].

5.2 The TFFs in the triangle diagram approach

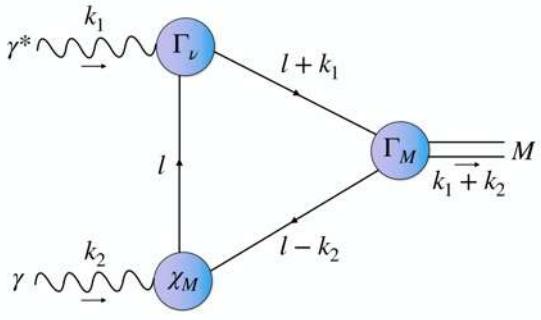

FIGURE 5.2: Triangular diagram for TFF of pseudoscalar mesons in the AM.

The other important observable in hadron physics is TFF. Additionally, in order to constraint the parameter space of the AM, it is important to compute analytically

[1] For neutral mesons composed of same flavored quarks, the total EFF is simply $F_{\rm M} = F_{\rm M}^q$.

the $\gamma\mathrm{M}\gamma$ vertex in our approach. The interaction vertex that describes the $\gamma\gamma^* \to \mathrm{M}$ transition, depicted in Figure 5.2, is described by a single form factor, G_{M},

$$\begin{aligned}\mathcal{T}_{\mu\nu}(k_1,k_2) &= \mathcal{T}_{\mu\nu}(k_1,k_2) + \mathcal{T}_{\nu\mu}(k_2,k_1) \\ &= \frac{e^2}{4\pi^2}\epsilon_{\mu\nu\alpha\beta}k_{1\alpha}k_{2\beta}G_{\mathrm{M}}(k_1^2,k_2^2,k_1\cdot k_2)\,, \end{aligned} \tag{5.3}$$

where the momentum of the meson is $P = k_1 + k_2$, with k_1 and k_2 the incoming photon momenta. It is worth mentioning that in this work we only calculate the TFFs of the mesons: π, η_c and η_b; In this sense, and considering the isospin symmetry for pion and the equal flavors of the valence quarks of η_c and η_b, we have a single TFF instead of two as for the EFF equation. On the other hand, the matrix element obtained by standard Feynman rules of Figure 5.2 is,

$$\mathcal{T}_{\mu\nu}(k_1,k_2) = \mathrm{tr}\int_l i\mathcal{Q}\chi_\mu(l,l+k_1)\Gamma_\pi(l+k_1,l-k_2)S(l-k_2)i\mathcal{Q}\Gamma_\nu(l-k_2,l)\,, \tag{5.4}$$

where $\mathcal{Q} = \mathrm{diag}[e_q, e_h]$. Also, the momentum of the real and virtual photons are $k_1^2 = Q^2$, $k_2^2 = 0$, where it must be fulfilled that $2k_1\cdot k_2 = -(m_{\mathrm{M}}^2 + Q^2)$.

5.3 EFFs of scalar and pseudo-scalar mesons in a CI treatment

To carry out the following calculations, the Contact Interaction model will be used.

5.3.1 Scalar mesons

Recall that an S meson is a 0^{++} state. It can be considered as the chiral partner of the PS meson Figure 5.3. We work under the assumption that all states are purely quark-antiquark states. Then, for example, the states π and σ get transformed into each other through the following chiral transformation:

$$q \to \mathrm{e}^{-i\gamma_5\frac{\tau}{2}\cdot\boldsymbol{\theta}}q\,. \tag{5.5}$$

The explicit expression for the EFFs for S mesons with mass M_M constituted from a

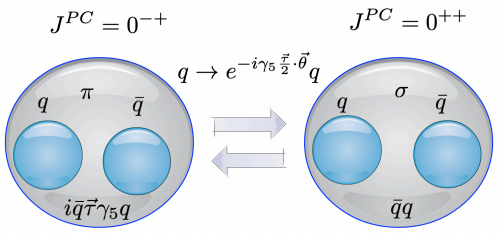

FIGURE 5.3: The S meson, e.g., σ is viewed as the parity partner of the pion π. Note that the scalars in this thesis only refer to their quark-antiquark content.

TABLE 5.1: Ultraviolet regulator and the coupling constant for different combinations of quarks in S mesons. As before, $\hat{\alpha}_{\rm IR} = \hat{\alpha}_{\rm IRL}/Z_H$, where $\hat{\alpha}_{\rm IRL} = 4.57$ is extracted from a best-fit to data as explained in Ref. [85]. $\Lambda_{\rm IR} = 0.24$ GeV.

quarks	Z_H	$\Lambda_{\rm UV}$ [GeV]	$\hat{\alpha}_{\rm IR}$
u, d, s	1	0.905	4.57
c, u	3.034	1.322	1.50
c, s	3.034	2.222	1.50
c	13.122	2.305	0.35
b, u	18.473	10.670	0.25
b, s	29.537	11.064	0.15
b, c	34.216	14.328	0.13
b	127.013	26.873	0.036

quark q and an antiquark $\bar{h}$ is given by Eq. (5.2) with

$$F^{S,q} = P_T(Q^2) E_S^2 T_{EE}^S(Q^2)\,, \tag{5.6}$$

where

$$T_{EE}^S(Q^2) = -\frac{3}{4\pi^2}\left[\int_0^1 d\alpha\, \overline{\mathcal{C}}_1(\omega_1) + 2\int_0^1 d\alpha\, d\beta\, \alpha\, \mathcal{A}_{EE}^S\, \overline{\mathcal{C}}_2(\omega_2)\right], \tag{5.7}$$

with

$$\mathcal{A}_{EE}^S = \alpha M_q - 2(1-\alpha) M_q M_{\bar{h}} + (\alpha - 2) M_{\bar{h}}^2 + \alpha M_M^2\,. \tag{5.8}$$

Note the close resemblance between T_{EE}^S and T_{EE}^{PS}. As expected, there are only sign differences between the two due to the presence, or absence, of the γ^5 matrix. In Table 5.1, we present the parameters used for S mesons in order to compute the masses,

TABLE 5.2: Computed values of the S mesons masses and BSAs in the CI model, see [91] for comparison, using the parameters listed in Tables 3.2 and 5.1.

	Mass [GeV]	E_S	m_S^{exp} [GeV]	error [%]
$u\bar{d}$	1.22	0.66	–	–
$u\bar{s}$	1.38	0.65	–	–
$s\bar{s}$	1.46	0.64	–	–
$c\bar{u}$	2.31	0.39	2.30	0.19
$c\bar{s}$	2.42	0.42	2.32	3.54
$u\bar{b}$	5.30	1.53	–	–
$s\bar{b}$	5.64	0.26	–	–
$c\bar{b}$	6.36	1.23	6.71	5.26
$c\bar{c}$	3.33	0.16	3.42	2.73
$b\bar{b}$	9.57	0.69	9.86	2.95

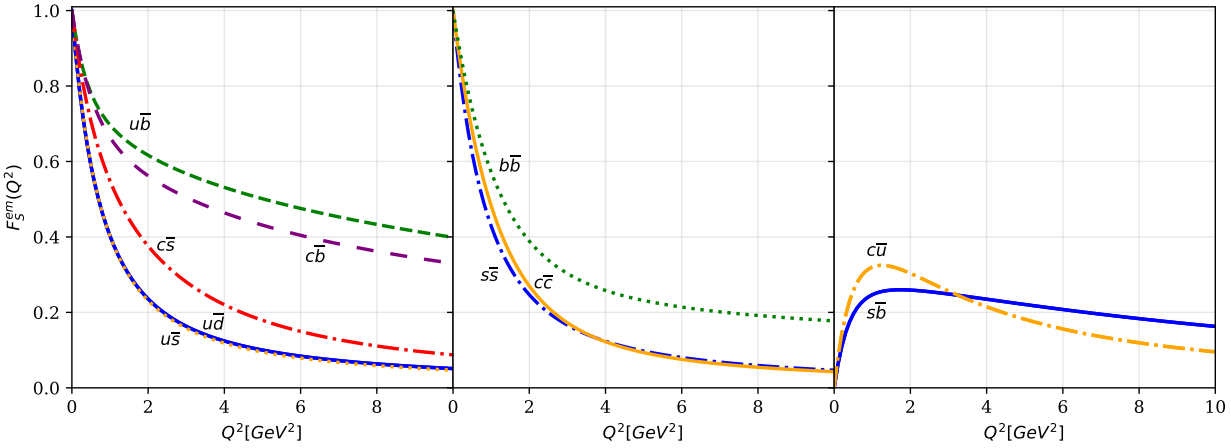

FIGURE 5.4: EFFs for S mesons in the CI model. Left panel: electrically charges mesons composed of quarks of different flavors. Central panel: quarkonia including a hypothetical ground state *strangeonium* ($s\bar{s}$). Right panel: electrically neutral mesons composed of quarks of different flavors. EFFs of electrically neutral but flavored mesons have been normalized to $F^S(0) = 0$.

amplitudes and charge radii. We enlist the masses and BSAs of S mesons in Table 5.2 while the EFFs are depicted in Figure 5.4. On the right and central panels we present the results for neutral mesons while the left panel displays the EFFs of charged mesons.

TABLE 5.4: Parameters for the fit in Eq. (5.9) for S mesons.

	a_S	b_S	c_S	d_S
$u\bar{d}$	0.286	0.003	1.543	0.617
$u\bar{s}$	0.266	0.002	1.486	0.629
$s\bar{s}$	0.217	0.001	1.271	0.542
$c\bar{u}$	0.759	−0.005	0.680	0.641
$c\bar{s}$	0.004	0.001	0.783	0.047
$u\bar{b}$	0.984	0.001	1.619	0.087
$s\bar{b}$	0.210	0.001	0.175	0.115
$c\bar{b}$	0.289	0.001	0.743	0.026
$c\bar{c}$	0.217	0.001	0.860	0.673
$b\bar{b}$	0.269	0.000	1.607	0.020

We emphasize that for electrically neutral but flavored S mesons, we normalize the EFFs to zero at $Q^2 = 0$, while for flavorless mesons, the normalization is $F^S(0) = 1$ to be consistent with the definition employed in Eq. (5.2). We again perform a fit in the range $Q^2 \in [0, 8M_M^2]$, where M_M is the mass of the S meson. All the curves are faithfully reproduced by the following choice:

$$F^S(Q^2) = \frac{e_M + a_S\, Q^2 + b_S\, Q^4}{1 + c_S\, Q^2 + d_S\, Q^4}\,, \tag{5.9}$$

where $e_M := F^S(Q^2 = 0)$ is the electric charge of the meson and a_S, b_S, c_S, d_S are the parameters of the fit. These values for S mesons are listed in Table 5.4. Based on these numbers, we can immediately infer the large Q^2 behavior of these EFFs. The coefficient $b_S \approx 0$ for all S mesons under consideration. Therefore, the EFFs for S mesons fall as $1/Q^2$ for large Q^2.

We present the numerical values of the charge radii for S mesons in Table 5.5. We must reiterate that for the S mesons there are no reported measurements of their charge radii. Theoretical results are also scarce for any direct and meaningful comparison. It is worth mentioning again that the internal structure of scalar mesons is not well-established. Our results are based on considering them as effective quark-antiquark states.

We would like to remind the reader that we again allow for a 5% variation in the charge radii of S mesons. However, in Figure 5.4, we present the EFFs only for their

TABLE 5.5: The charge radii for S mesons. All quantities are reported in fm.

	$u\bar{d}$	$u\bar{s}$	$s\bar{s}$	$c\bar{u}$	$c\bar{s}$	$u\bar{b}$	$s\bar{b}$	$c\bar{b}$	$c\bar{c}$	$b\bar{b}$
Our Result	0.55	0.54	0.50	0.47	0.44	0.42	0.41	0.40	0.43	0.39

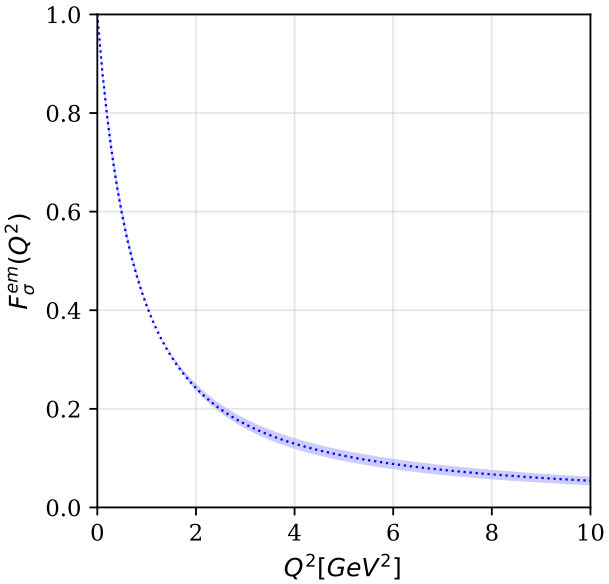

FIGURE 5.5: EFF for σ-meson. The central curve is obtained using the $\Lambda_{\rm UV}$ value from Table 5.1 while the band represents a 5% variation in the charge radius.

central values for visual clarity, refraining from showing the corresponding band to avoid possible overlapping. However, in Figure 5.5, we depict a representative plot with a 5% variation in the charge radius for the lightest scalar meson, σ, alone. Other mesons have similar bands. Finally, in Figure 5.6, we plot the charge radii, extracted from the EFFs, as a function of the S meson mass. In general, the charge radii decrease when the S meson masses increase just as we observed for the PS mesons.

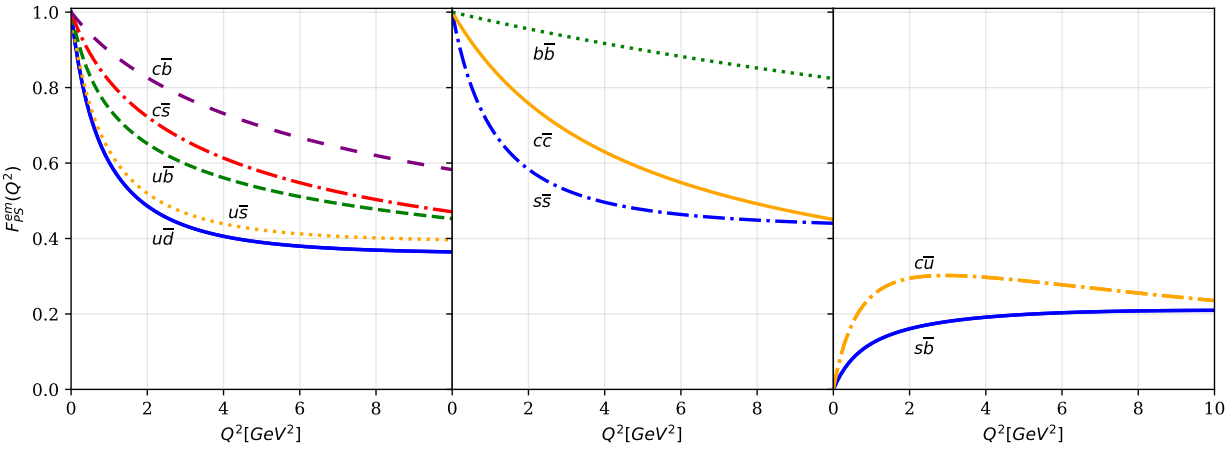

FIGURE 5.7: EFFs of PS mesons in a CI model. Left panel: electrically charged mesons composed of quarks of different flavors. Central panel: quarkonia including a hypothetical ground state *strangeonium* ($s\bar{s}$). Right panel: electrically neutral mesons composed of quarks of different flavors.

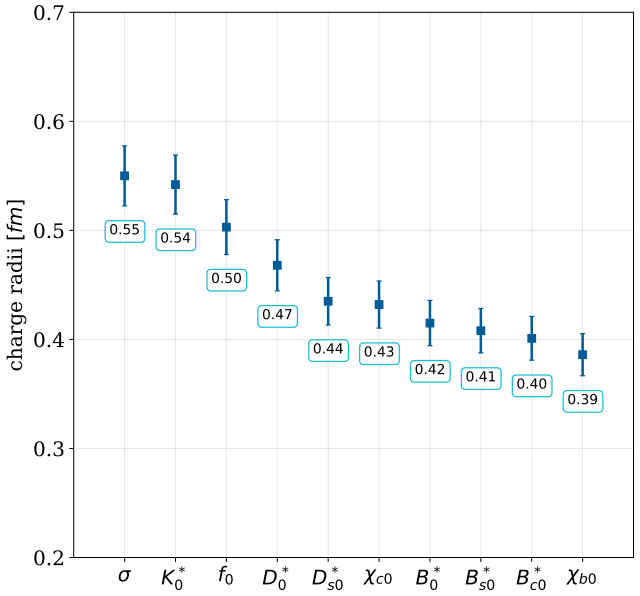

FIGURE 5.6: Charge radii of S mesons.

5.3.2 Pseudo-scalar mesons

We start with a detailed discussion and results on the ground state PS mesons. These are negative parity, zero angular momentum 0^{-+} states and occupy a special role in hadron physics. Simultaneously these are the simplest bound states of a quark and antiquark and also emerge as Goldstone bosons associated with DCSB. Pions are the lightest hadrons and are produced copiously in collider machines at all energies. The pion cloud effect substantially contributes to several static and dynamical hadron properties. Therefore, understanding their internal structure has been of great interest both for experimenters and theoreticians. The study of PS mesons is crucial in understanding the capabilities and limitations of the CI model employed in this work to reproduce and predict phenomenological results. Being the Goldstone bosons associated with DCSB, their analysis requires care in treating the associated subtleties. From Eqs. (3.71), we can see that the BSA of PS mesons is the only one to be composed of two terms, necessary to ensure the axial vector Ward-Takahashi identity and the Goldberger-Treiman relations are exactly satisfied. In this thesis, we extend and expand the work presented in [84, 85, 99] and compute the EFFs of a larger number of PS mesons composed of qq, qQ and QQ quarks. With straightforward algebraic manipulations:

$$F^{PS,q} = P_T(Q^2)\left[E_{PS}^2 T_{EE}^{PS}(Q^2) + E_{PS}F_{PS}T_{EF}^{PS}(Q^2) + F_{PS}^2 T_{FF}^{PS}(Q^2)\right], \tag{5.10}$$

where

$$\begin{aligned}
T_{EE}^{PS}(Q^2) &= \frac{3}{4\pi^2}\left[\int_0^1 d\alpha\, \overline{\mathcal{C}}_1(\omega_1) + 2\int_0^1 d\alpha\, d\beta\, \alpha\, \mathcal{A}_{EE}^{PS}\, \overline{\mathcal{C}}_2(\omega_2)\right], \\
T_{EF}^{PS}(Q^2) &= -\frac{3}{2\pi^2}\frac{1}{M_R}\int_0^1 d\alpha\, d\beta\, \alpha\left[\mathcal{A}_{EF}^{(1)}\, \overline{\mathcal{C}}_1(\omega_2) + (\mathcal{A}_{EF}^{(2)} - \omega_2 \mathcal{A}_{EF}^{(1)})\, \overline{\mathcal{C}}_2(\omega_2)\right], \\
T_{FF}^{PS}(Q^2) &= \frac{3}{4\pi^2}\frac{1}{M_R^2}\int_0^1 d\alpha\, d\beta\, \alpha\left[\mathcal{A}_{FF}^{(1)}\, \overline{\mathcal{C}}_1(\omega_2) + (\mathcal{A}_{FF}^{(2)} - \omega_2 \mathcal{A}_{FF}^{(1)})\, \overline{\mathcal{C}}_2(\omega_2)\right],
\end{aligned} \tag{5.11}$$

and

$$\begin{aligned}
\omega_1 &= \omega_1(M_q, \alpha, Q^2) = M_q^2 + \alpha\, Q^2(1-\alpha), \\
\omega_2 &= \omega_2(M_q, M_{\bar{h}}, \alpha, \beta, M_M) \\
&= \alpha\, M_q^2 + (1-\alpha)M_{\bar{h}}^2 - \alpha(1-\alpha)\, M_M^2 + \alpha^2\, \beta\, (1-\beta)\, Q^2, \\
\bar{\mathcal{C}}_2(z) &= (\exp(-z\,\tau_{\rm uv}) - \exp(-z\,\tau_{\rm ir}))/(2z).
\end{aligned} \tag{5.12}$$

The coefficients $\mathcal{A}_i$ are given by the following expressions:

$$\begin{aligned}
\mathcal{A}_{EE}^{PS} &= \alpha(M_q^2+M_M^2) + 2(1-\alpha)M_q M_{\bar{h}} + (\alpha-2)M_{\bar{h}}^2\,,\\
\mathcal{A}_{EF}^{(1)} &= M_q + M_{\bar{h}}\,,\\
\mathcal{A}_{EF}^{(2)} &= 2M_q^2 M_{\bar{h}} - \alpha M_q(4(\alpha-1)M_M^2 + \alpha Q^2)\\
&\quad + M_{\bar{q}}(2(\alpha-1)^2 M_M^2 + \alpha Q^2(2\alpha(\beta-1)\beta+\alpha-1))\,,\\
\mathcal{A}_{FF}^{(1)} &= (3\alpha-2)M_M^2 + \alpha Q^2\,,\\
\mathcal{A}_{FF}^{(2)} &= 2\alpha((\alpha-1)^2 M_M^4 + \alpha M_M^2 Q^2(3\alpha\beta^2 - 3\alpha\beta + \alpha - 2\beta^2 + 2\beta - 1))\\
&\quad + 2\alpha M_M^2 M_q^2 - 2M_q M_{\bar{h}}(2(\alpha-1)M_M^2 + \alpha Q^2)\,.
\end{aligned}$$

The resulting EFFs for charged as well as neutral mesons are shown in Figure 5.7. For the practical utility and intuitive understanding of their low and large Q^2 behavior, we perform an interpolation for PS mesons EFF in the range $Q^2 \in [0, 8M_M^2]$. We adopt the following functional form:

$$F^{PS}(Q^2) = \frac{e_M + a_{PS}\,Q^2 + b_{PS}\,Q^4}{1 + c_{PS}\,Q^2 + d_{PS}\,Q^4}\,, \tag{5.13}$$

where $e_M := F^{PS}(Q^2 = 0)$ is the electric charge of the meson and $a_{PS}, b_{PS}, c_{PS}, d_{PS}$ are the fitted coefficients. The best fit corresponds to the values listed in Table 5.6. The fit of Eq. (5.13) resonates with our observation that the EFFs of PS mesons tend to constant values for large Q^2 when it becomes by far the largest energy scale in the problem. It is a straightforward consequence of CI treatment, and it is characteristic of a point-like interaction which leads to harder EFF. However, the heavy as well as heavy-light mesons approach a constant value much slower than the light ones. This comparative large Q^2 behavior of EFFs owes itself to the fact that Q^2 becomes larger than all other energy scales at much higher values.

Once again, the behavior of the form factors at the other extreme, $Q^2 \simeq 0$ allows us to extract charge radii, Eq (2.13). For $c\bar{u}$ and $s\bar{b}$ states, which are normalized to $F^M(0) = 0$, we define r_M^2 with a positive sign in the above equation. The charge radii set the trend for the subsequent evolution of the form factors as a function of Q^2, specially for its small and intermediate values. Figure 5.8 depicts charge radii for all the PS mesons studied, allowing for a 5% variation around the central value. With this permitted spread in the charge radii, one can obtain a band for the Q^2 evolution of the EFFs. To avoid over-crowding, we have avoided depicting such a band for each EFF.

TABLE 5.6: Parameters from the fit of Eq. (5.13) for PS mesons

	a_{PS}	b_{PS}	c_{PS}	d_{PS}
$u\bar{d}$	0.330	0.029	1.190	0.068
$u\bar{s}$	0.335	0.029	1.092	0.065
$s\bar{s}$	0.328	0.040	0.874	0.092
$c\bar{u}$	0.616	−0.001	1.370	0.109
$c\bar{s}$	0.615	0.028	0.897	0.111
$u\bar{b}$	1.143	0.033	1.921	0.146
$s\bar{b}$	0.218	0.000	0.840	0.009
$c\bar{b}$	0.333	0.003	0.493	0.021
$c\bar{c}$	1.778	0.057	1.994	0.334
$b\bar{b}$	0.099	0.000	0.127	0.002

However, the right Figure 5.9 shows a representative plot for the pion permitting a 5% variation in its charge radius in conjunction with the available experimental results.

Finally we list the central values of all ground state PS mesons charge radii in Table 5.7, along with a direct comparison with available experimental observations, lattice results and the SDE findings. Moreover, we also report the transition charge radii of light PS mesons and flavorless neutral heavy PS mesons to two photons invoking the following analytical parameter fit [112]:

$$r_M^t = \frac{r_0}{1 + (M_M/m_t)\ln(1 + M_M/m_t)}\,, \tag{5.14}$$

where $r_0 = 0.67$ fm and $m_t = 1.01$ GeV. It also yields reasonable results for the π point (mass = 0.139 GeV) and the K point (mass = 0.493 GeV) as they are made of light quarks. But we cannot expect it to serve exactly as it is for mesons with vastly off-balanced quark masses. However, if CI results were to follow this formula, we would only need to assign $r_0 = 0.458$ fm. The last row of Table 5.7 lists the resulting values which we denote as $r_M^t(CI)$. Let us now summarize our findings and make explicit comparisons with related works:

- As desired, pion EFF and its charge radius agree with the first results employing the CI [84]. As an add-on, in this thesis we allow for a 5% variation of the pion charge radius to see its effect on the evolution of the EFF as a function

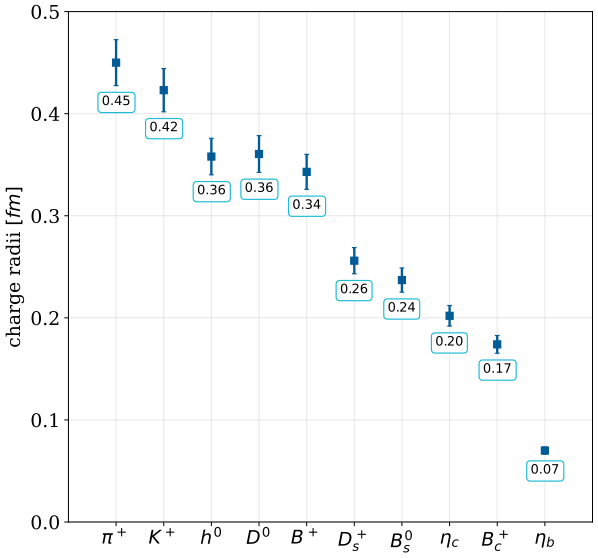

FIGURE 5.8: Charge radii of ground state PS mesons in the CI.

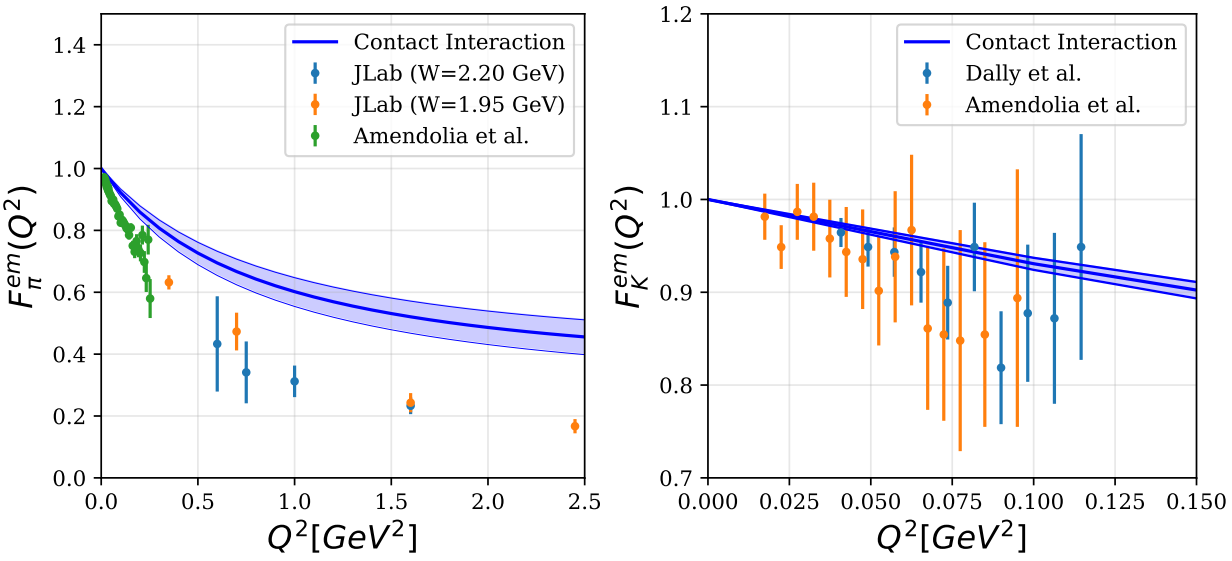

FIGURE 5.9: Left panel. EFF for π-meson. The central curve is obtained using the $\tau_{\rm UV}$ value from the Table 3.3. The filled band allows for a 5% variation in the charge radius. Dots represent the experimental data from Refs. [11, 13, 14]. Right panel. EFF for K-meson. The central curve of the (blue) band is obtained by using the $\Lambda_{\rm UV}$ value from Table 3.3. The filled (blue) band allows for a 5% variation in the charge radius. The experimental data is from Ref. [11].

of Q^2, Figure 5.9. A small variation of the initial slope of the curve $Q^2 \simeq 0$ opens a noticeable spread for large Q^2 but keeps the qualitative and quantitative behaviour fully intact.

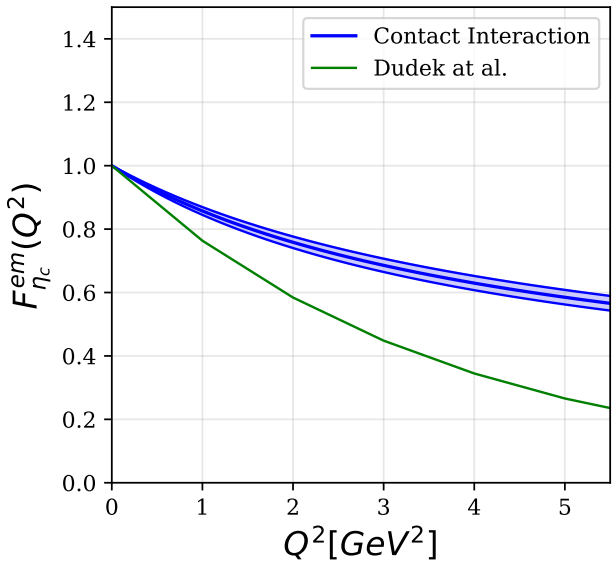

FIGURE 5.10: EFF for η_c-meson. The lower (green) solid curve is the lattice result, Ref. [150]. The central curve of the (blue) band is obtained using the $\Lambda_{\rm UV}$ value from Table 3.3. The filled (blue) band allows for a 5% variation in the charge radius.

- In the right panel of Figure 5.9, we draw kaon EFF over the range of Q^2 values where (relatively poor) experimental observations are available. Although large error bars prevent us from commenting decisively on the validity of the CI but we expect it will yield harder results as compared to precise experimental measurements whenever these results will become available. Our reported value of its charge radius is an indication of this behavior.

- As depicted in Table 5.7, pion and kaon charge radii [121, 149, 155–158] are known experimentally and through lattice and SDE studies. As CI EFFs come out to be harder than *full* QCD predictions, we expect our PS mesons charge radii to undershoot the exact results. This is precisely what we observe for the pion and the kaon. The percentage relative difference between the experimental value and our calculation for the pion charge radius is approximately 32%, while for the kaon charge radius is slightly less, 25%. Similar difference between the SDE and the CI results for heavy quarkonia is observed: For η_c, it is 20% while for η_b is is 22%, not too dissimilar. This comparatively analogous behavior augments our expectation that we will be in the same ballpark for the PS mesons whose charge radii are neither known experimentally as yet nor lattice offers any results.

- There are no experimental or lattice (to the best of our knowledge) results available for $c\bar{u}$, $c\bar{s}$, $u\bar{b}$, $s\bar{b}$ and $c\bar{b}$ mesons for comparison. However, the general trend of

TABLE 5.7: The charge radii of PS meson systems, calculated with the CI model, refined SDE studies, lattice QCD and extraction from data, in a hybrid model (HM), light-front framework (LFF) and a QCD potential model (PM). In the two rows after the experimental results, we also provide the best fit results for the transition charge radii of PS mesons to $\gamma\gamma^*$, Eq. (5.14) and the same fit adapted to the CI. All results are presented in fm.

	$u\bar{d}$	$u\bar{s}$	$s\bar{s}$	$c\bar{u}$	$c\bar{s}$
Our Result	0.45	0.42	0.36	0.36	0.26
SDE [121, 155]	0.676 ± 0.002	0.593 ± 0.002	-	-	-
Lattice [149, 156, 157]	0.648 ± 0.141	0.566 (extracted)	-	-	-
Exp. [158]	0.659 ± 0.004	0.560 ± 0.031	-	-	-
r_M^t [112]	0.658	0.568	-	-	-
r_M^t(CI)	0.45	0.38	0.33	-	-
HM [159]	0.66	0.65	-	0.47	0.50
LFF [160]	0.66	0.58	-	0.55	0.35
PM [161]	-	-	-	0.67	0.46
	$u\bar{b}$	$s\bar{b}$	$c\bar{b}$	$c\bar{c}$	$b\bar{b}$
Our Result	0.34	0.24	0.17	0.20	0.07
SDE [121, 155]	-	-	-	0.24	0.09
Lattice [149, 156, 157]	-	-	-	0.25	-
r_M^t [112]	-	-	-	0.13	0.03
r_M^t(CI)	-	-	-	0.09	0.02
LFF [160]	0.61	0.34	0.20	-	-
PM [161]	0.73	0.46	-	-	-

decreasing charge radii with increasing constituent quark mass seems reassuring, e.g., the following hierarchies are noticeable:

$$r_{u\bar{d}} > r_{u\bar{s}} > r_{c\bar{u}} > r_{u\bar{b}}\,,$$
$$r_{u\bar{s}} > r_{s\bar{s}} > r_{c\bar{s}} > r_{s\bar{b}}\,,$$
$$r_{c\bar{u}} > r_{c\bar{s}} > r_{c\bar{c}} > r_{c\bar{b}}\,,$$
$$r_{u\bar{u}} > r_{s\bar{s}} > r_{c\bar{c}} > r_{b\bar{b}}\,.$$

We must emphasize that the CI is only a simple model. Refined QCD calculations are required to confirm or refute these findings.

This concludes our detailed analysis of all the ground state PS heavy ($Q\bar{Q}$), heavy-light

$(Q\bar{q})$ as well as light $(q\bar{q})$ mesons. We now turn our attention to a similar analysis of the scalar mesons.

5.4 EFFs and TFFs of Goldstone bosons and heavy pseudo-scalar meson in an AM treatment

To carry out the following calculations, the Algebrac Model will be used.

5.4.1 Computing the EFFs using the AM

In order to find individual contributions of constituent quarks, $F_{\rm M}^{q}$, we contract Eq. (5.1) with the K^{μ} and taking the quark-photon vertex and the *Ansätze* of the AM, we find,

$$K^2 F_{\rm M}^{q}(Q^2) = 2N_c \int_k \int_{-1}^{1} \prod_{i=1}^{2} dw_i \rho(w_i) \Lambda_{w_i}^{2\nu_i} \mathcal{M}_{q,\bar{h}}(k,K) \mathcal{D}_{q,\bar{h}}^{\nu_{1,2}}(k,K)\,, \tag{5.15}$$

where the numerator $\mathcal{M}_{q,\bar{h}}$ has the form,

$$\begin{aligned} \mathcal{M}_{q,\bar{h}}(k,K) \equiv & -2(K\cdot k)[2k^2 + 4m_q^2 m_{\bar{h}}^2 - 2m_q^2 - 2m_M^2] \\ & + (4m_M^2 + Q^2)[2t^2 + 2m_q m_{\bar{h}}]\,, \end{aligned} \tag{5.16}$$

and $\mathcal{D}_{q,\bar{h}}^{\nu_{1,2}}(k,K)$ contains the product of all denominators

$$\begin{aligned} \mathcal{D}_{q,\bar{h}}^{\nu_{1,2}}(k,K) = & \Delta(k_{(1+w_1),i}^2, \Lambda_{w_1}^2)^{\nu_1} \Delta(k_{(1-w_2),f}^2, \Lambda_{w_1}^2)^{\nu_2} \\ & \times \Delta((k+p_f)^2, m_q^2) \Delta((k+p_i)^2, m_q^2) \Delta(k^2, m_{\bar{h}}^2)\,, \end{aligned} \tag{5.17}$$

with, $k_{(1\pm w),i} = k + (1 \pm w)p_i/2$.

To compute the integration on k in Eq. (5.15), we introduce Feynman parameterizations and applying a suitable change of variables. In this sense, we find that the denominator can be reduced to $[k^2 + \Omega^2]^{\nu_1+\nu_2+3}$ where Ω^2 has the following form,

$$\Omega^2 = \frac{1}{4}Q^2 c_0 + \frac{1}{2}(m_q^2 - m_{\bar{h}}^2)c_1 + \frac{1}{4}m_{\rm M}^2 c_2 + m_{\bar{h}}^2\,, \tag{5.18}$$

with, $c_{0,1,2}$ given in terms of Feynman parameters. Considering that we are computing an elastic scattering, it is clear that the initial meson is the same as the final meson, thus without loss of generality we choose $\nu = \nu_1 = \nu_2$. Hence, the integral in Eq. (5.15) becomes,

$$\int_k \frac{\mathcal{M}_{q,\bar{h}}(k,K)}{[t^2+\Omega^2]^{2\nu+3}} = \int_k \frac{k^2\mathcal{A}+\mathcal{B}}{[k^2+\Omega^2]^{2\nu+3}} = \alpha\frac{\mathcal{A}}{[\Omega^2]^{2\nu}} + \beta\frac{\mathcal{B}}{[\Omega^2]^{2\nu+1}}\,, \tag{5.19}$$

where,

$$\begin{aligned}
\mathcal{A} &= 3[u_1(1+w_1)+u_2(1-w_2)+2u_3+2u_4]-8\,,\\
\mathcal{B} &= -\frac{1}{2}m_{\rm M}^2[u_1(1+w_1)+u_2(1-w_2)+2(u_3+u_4-1)]^2\\
&\quad\times[u_1(1+w_1)+u_2(1-w_2)+2(u_3+u_4)]\\
&\quad+4m_q^2m_{\bar{h}}^2[u_1(1+w_1)+u_2(1-w_2)+2(u_3+u_4-1)]\\
&\quad-\frac{1}{2}Q^2[u_1(1+w_1)+2u_4][u_2(1-w_2)+2u_3]\\
&\quad\times[u_1(1+w_1)+u_2(1-w_2)+2(u_3+u_4-2)]\,,
\end{aligned} \tag{5.20}$$

with u_1, u_2, u_3 the Feynman parameters, and α and β are the constants:

$$\begin{aligned}
\alpha &= \frac{1}{(4\pi)^2}\frac{1}{2\nu(2\nu^2+3\nu+1)}\,,\\
\beta &= \nu\alpha\,.
\end{aligned} \tag{5.21}$$

Thus, the EFF can be expressed as follows

$$\begin{aligned}
F_{\rm M}^q(Q^2) = 2N_c\frac{\Gamma[2\nu+3]}{\Gamma[\nu]^2}\int_{-1}^{1}\prod_{i=1}^{2}dw_i\rho(w_i)\Lambda_{w_i}^{2\nu}\int_0^1 du_1\int_0^{1-u_1}du_2\cdots\int_0^{1-u_1-u_2-u_3}du_4\\
\times(u_1\,u_2)^{\nu-1}\left[\frac{\alpha\mathcal{A}}{\Omega^{2(2\nu)}}+\frac{\beta\mathcal{B}}{\Omega^{2(2\nu+1)}}\right].
\end{aligned} \tag{5.22}$$

Finally, this Eq. (5.22) can be computed numerically and with the definition given in Eq. (5.2) and using the spectral density extracted in Chapter 4, we can proceed to the analysis of the EFFs of pseudoscalar mesons.

5.4.2 Computing the TFFs

According to the AM, i.e., from the Eqs. (3.81), (3.82) and (3.98), we obtained the following form to the TFF,

$$G_{\rm M}(k_1^2, k_2^2, k_1\cdot k_2) = \frac{4\pi^2}{e^2}\frac{\epsilon_{\mu\nu\lambda\rho}k_{1\lambda}k_{2\rho}}{\epsilon_{\mu\nu\lambda\rho}k_{1\lambda}k_{2\rho}\epsilon_{\mu\nu\alpha\beta}k_{1\alpha}k_{2\beta}}\int_l\int_{-1}^{1} dw\rho(w)\Lambda_w^{2\nu}\mathcal{M}'(l,Q)\mathcal{D}'(l,Q)\ ,$$

where $\mathcal{M}'(l,Q)$ is the numerator that contains all the matrix information and $\mathcal{D}'(l,Q)$ corresponds to the product of all denominators as,

$$\mathcal{D}'(l,Q) = \Delta((l-k_2)^2, m_q^2)\Delta((l+k_1)^2, m_q^2)\Delta(l^2, m_q^2)\Delta(k_{(w-1)}^2, \Lambda_w^2)^\nu\ . \tag{5.23}$$

Again, introducing Feynman parametrization and reducing the denominator with a suitable change of variable, the above equation can be solved. Furthermore, since the photon can interact with the quark or the anti-quark, we could define the total TFF as, similarly to Eq. (5.2),

$$G_{\rm M}(Q^2) = e_q G_{\rm M}^q(Q^2) + e_{\bar{h}} G_{\rm M}^{\bar{h}}(Q^2)\,. \tag{5.24}$$

However, taking into account equal masses for the quark and antiquark, the TFF is reduced to $G_M(Q^2) = G_M^q(Q^2)$. Finally, with Eq. (5.2) and Eq. (5.24), we proceed to analyse the viability of the model in the next section.

5.4.3 Results

In this section we present the results for the EFF and TFF of pseudoscalar mesons; in particular, pion, kaon, η_c and η_b. In addition, we analyze the impact of our predictions in future experimental studies.

The determination of the parameters of the algebraic model were found by the implementation of a global χ^2 with experimental data and phenomenological inputs of EFFs and TFFs of pseudoscalar mesons. The standard χ^2 statistical test, for a set with N number of data points, is given by,

$$\chi^2 = \sum_{i=1}^{N}\frac{(E_i - T_i)^2}{\delta E_i^2}\,, \tag{5.25}$$

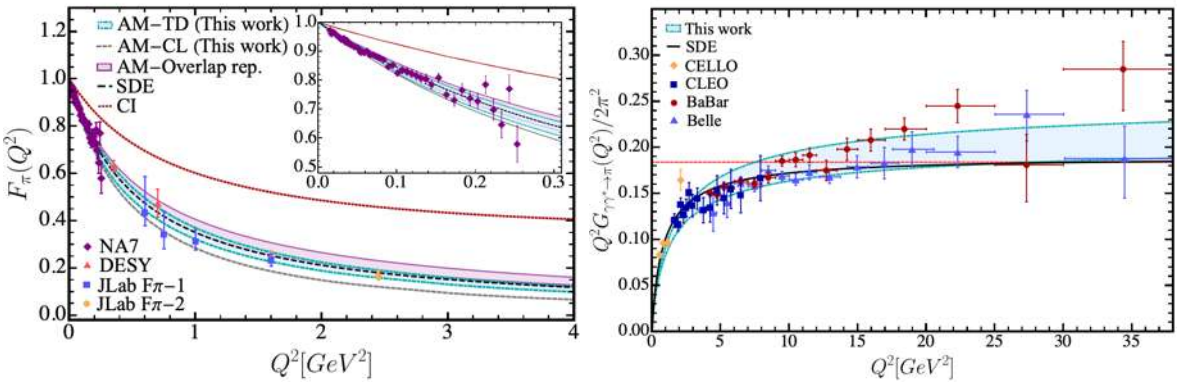

FIGURE 5.11: Pion EFF and TFF. Left panel- Pion EFF. Our pion results are represented with the light blue band. The purple band corresponds to the AM previous results from the overlap representation presented in [27]. Dashed black line is the SDE result for the pion [110, 148] and the SDE-driven predictions in the contact interaction (CI) model is represented by the dotted dark red line [28]. Diamonds, rectangles, triangles and circles represent the experimental data from Refs. [11–15]. Right panel- Pion TFF. The blue light band corresponds to our TFFs results of pion. The light red dashed line is the asymptotic limit. The black solid line corresponds to the SDEs results from [109] and the experimental results are taken from [16–19].

where E_i represents the i-th experimental data to fit, T_i the theoretical predicted i-th value for a given point and δE_i is the estimated error associated to the i-th fitted data. We therefore implemented the statistical analysis for the experimental data coming from the references shown in Table 5.8, in order to minimize the χ^2.

Meson	EFF	TFF
π	Refs. [11–15]	Ref. [16–19]
K	Ref. [162, 163]	—
η_c	—	Ref. [164]

TABLE 5.8: Experimental data fitted in our global analysis of EFFs and TFFs of pseudoscalar mesons.

It is important to highlight that experimental measurement of TFF for kaons are not available for this process. On the other hand, experimental inputs for η_c are only reported for TFF and for EFF we use the predictions coming from SDEs of the charge radii [165]. In the case of η_b, there are only theoretical predictions from SDEs [111] to analyze for TFF and in the case of EFF we use the expected charge radii of η_b from Ref. [166] as a value to fit.

5.4.3.1 The Pion case

We start our analysis with the lightest mesons, pions. Since pions are copiously produced in the high energy collision environment, we take the advantage of the largest amount of data points for both soft and hard processes to constrain the parameters of the AM using the experimental data. It is important to highlight that in order to reduce the complexity in the calculation we assume isospin symmetry between u and d quarks, such that $m_u = m_d$, and we allow variations around 0.3 GeV $< m_u <$ 0.5 GeV. In order to find the best phenomenological fitted values, we allow variations for the pion mass respecting the experimental data coming from the PDG [167]. Therefore, experimental data from Refs. [11–19] shall constraint the dimensionless parameters ν_π and α_u and the masses. In Tab. 5.9 we present the obtained best parameters for the χ^2.

m_u	m_π	ν_π	$\alpha_u^{(0)}$
0.3135	0.1395	0.8428	0.1964

TABLE 5.9: Best fitted values for the pion meson in the AM. The reported values for pion correspond to the $u-$quark since isospin symmetry between u and d quarks is considered. Masses are given in GeV.

Results extracted from the fit allow us to determine the charge radii of pions from EEF, r_π, obtaining,

$$r_\pi^{\text{fit}} = 0.67 \text{ fm}, \tag{5.26}$$

which presents small deviations from the experimental measurements of about 1.17 % [158].

In Tab. 5.10 we report the corresponding χ^2 per data sets for pions. We can distinguish that the global fit has a $\chi^2/d.o.f. \sim 1.93$ confirming that the predictions are in agreement with experimental data except for the BaBar data of the TFFs at large Q^2 in the TFFs. This fact is manifest in Figure 5.11. The error bands reported in Figure 5.11 were obtained by allowing a variation of 5% on the charge radii of the EFF only; the obtained parameters were used for pion TFF results.

It is important to recall that the phenomenological agreement is achieved when ν_π tends to unity and a small value for $\alpha_u^{(0)}$. This fact is due to the expected behaviour

experiment	# data in fit	χ^2
NA7[11]	45	48.42
DESY[12]	2	2.50
JLab Fπ-1[13]	4	1.16
JLab Fπ-2[14, 15]	4	2.56
CELLO[16]	5	83.55
CLEO[17]	15	15.44
Belle[19]	15	21.72
BaBar[18]	17	30.95
TOTAL:	107	206.3

TABLE 5.10: Data sets used in our global analysis for pions, the individual χ^2 values, and the total χ^2 of the fit.

of large Q^2 regime where the EFF and TFF are expected to decreased as Q^{-2} and the almost point-like interaction of the photon with the $u-$quark is raised. Therefore, these deviations could be understood as a first approximation of the complete theory.

With the previous results, we can analyze the expected theoretical predictions of the AM for EFF of pions for expected center of mass energies of the EIC and JLab. In Figure 5.12 we present the insight given by the AM and a comparison with other results from the SDEs and the monopole form from [110]. We point out that the predictions given by the global fit of pions are in accordance with the previous results of the SDEs and in turn have the expected behavior by the projected EIC [21] and JLab at 12 GeV and 22 GeV [25].

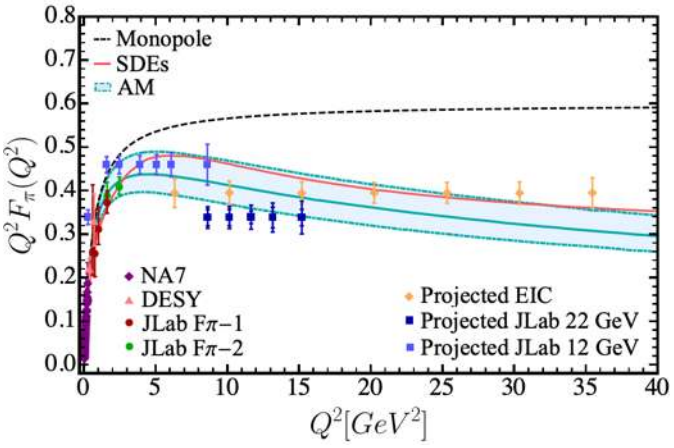

FIGURE 5.12: Predictions of the AM for the pion EFF at Q^2 up to 40 GeV. Projected EIC and JLab at 22 GeV and 12 GeV [21–25] are shown in here.

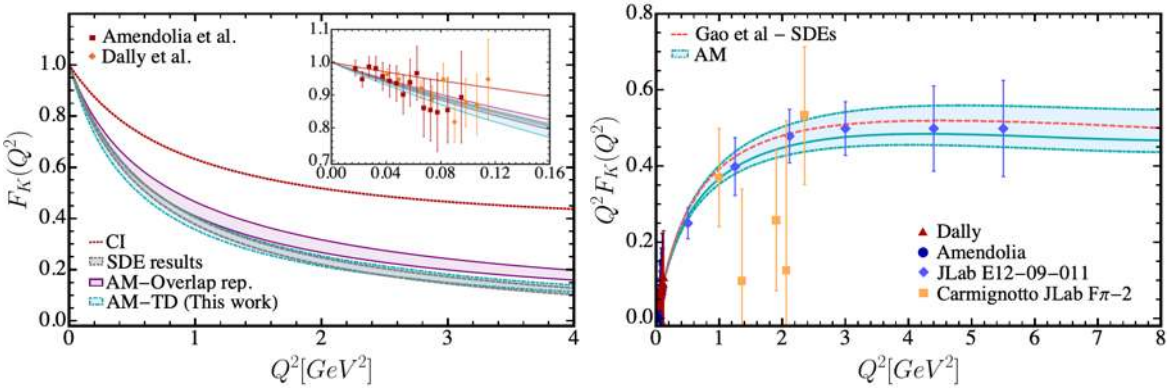

FIGURE 5.13: Kaon EFF. Our result is represented with the light blue band. The purple band corresponds to the AM previous results from the overlap representation presented in [27]. Circles, diamonds, rectangles and triangles represent the experimental data from Refs. [162, 163, 168]. For comparison, we have included the lower gray band that corresponds to the SDE result for the kaon [120, 169] as well as SDE-driven predictions in the contact interaction (CI) model (dotted dark red line) [28].

5.4.3.2 The Kaon case

We now turn to the study of kaon pseudoscalar mesons. The understanding of kaons as pions is of paramount importance. Since these are the only "massless" systems in QCD known as Nambu-Goldstone (NG) bosons, which are responsible for holding protons and neutrons together in the atomic nucleus. For this reason, they differ from all other hadrons that have nuclear-sized masses far in excess of anything that can directly be tied to the Higgs boson. Particularly, unlike the pion, the kaon is formed by quarks of different flavors (up and strange), which implies the need for a greater effort when seeking a complete understanding of its dynamics and internal structure, but this understanding would help in the comprehension of the mass hadrons origins and the distribution of it within them. However, the information obtained from pions, in particular those related to the u quark shall be an input for the fit. Regardless all efforts to tightly constraint the parameters of the s quark and the kaon mass, we posses only the experimental values of EFF of kaons. These values were fitted, within pion parameters, providing the best parameters shown in Tab. 5.11. Large uncertainties on the determination of the experimental data allow us to have $\nu_K = 0.913$ close to 1. Furthermore, we maintain between the kaon mass error of the PDG data [170] which gives a good hint on the determination of the properties of kaon mesons. In addition,

m_s	m_K	ν_K	$\alpha_s^{(0)}$
0.5274	0.4936	0.913	–

TABLE 5.11: Best fitted values for kaon mesons in the AM. Kaon parameters correspond to s quark since the values of the u quark is taken from Tab. 5.9. Masses are given in GeV.

we compute the charge radii of kaons, r_K of,

$$r_K^{\text{fit}} = 0.64 \text{ fm}\,, \tag{5.27}$$

which have a small deviation from the experimental result $\sim 0.58 \pm 0.2$ fm [171]. Besides, in Tab. 5.12 we report the χ^2 corresponding to the experimental data of kaon EFF which reports a $\chi^2/d.o.f. \sim 0.705$. We present our results of the EFFs for the

experiment	# data in fit	χ^2
Amendolia [162]	15	5.2822
Dally [163]	10	17.8976
Carmignotto JLab [168]	5	1.3620
JLab E12-09-011	6	0.8444
TOTAL:	36	25.3864

TABLE 5.12: Data sets used in our global analysis for kaons, the individual χ^2 values, and the total χ^2 of the fit.

fit of the kaon parameters in the AM on the left-hand side of Figure 5.13. Similarly to pion EFF, we report error bands of around 5% of the charge radii in kaon results. In addition, we explore on the right-hand side of Figure 5.13 the impact of our results and other references on the expected predictions given in Refs. [162, 163, 168] which are increasing the range of Q^2 up to 6 GeV in JLab experiments.

5.4.3.3 The η_c case

We now continue to the analysis of heavy pseudoscalar mesons such as quarkonia mesons. These are characterized by having large quark masses while having small relative moments. However, just like the SDEs the AM does not make any assumptions about the strength of the interaction between the quarks involved, so it is also possible for us to analyze systems wich probe different energy scales simultaneously.

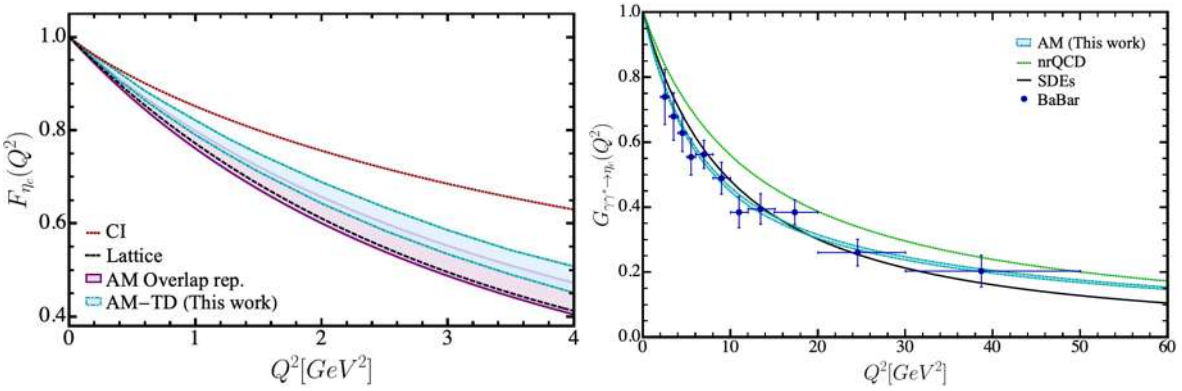

FIGURE 5.14: η_c EFF and TFF. Left panel- η_c EFF. The blue band represents our results with the parameters of Table 5.13. For comparison, we have included the following results: The light purple band that represents the η_c previous AM results from the overlap representation presented in [27], the dashed black line that corresponds to the lattice QCD results from Refs. [149, 150], and the SDE-driven predictions in the contact interaction (CI) model (dotted dark red line) [28]. Right panel- η_c TFF. The blue light band corresponds to our TFFs results. The black solid line corresponds to the SDEs results [111]. The green dotted line corresponds to the NLO nrQCD predictions [172]. The experimental data corresponds to BaBar collaboration from [164].

Therefore, the next simple pseudoscalar meson to analyze is the formed with the c quark, η_c. In this case, we have the charm mass, the η_c mass and the dimensionless parameters ν_{η_c} and α_c to determine from the fit. For η_c, we have only the experimental data coming from BaBar for TFF which shall help us to constraint the parameter space. On the other hand, we have constraints of EFF for η_c mesons coming the expected SDE prediction of the charge radii [166], $r_{\eta_c} = 0.219$. We present in Tab. 5.13 the best parameters which describe the data from BaBar and SDEs phenomenology. We find similar deviations of ν_{η_c} from unity as in the pion scenario and, in addition, the preferred mass of η_c meson deviates from Ref. [166] of around 4.9%.

m_c	m_{η_c}	ν_{η_c}	$\alpha_c^{(0)}$
1.7364	3.1307	0.8021	0.2669

TABLE 5.13: Best fitted values for η_c mesons in the AM. Masses are given in GeV.

We present in Tab. 5.14 the obtained χ^2 of our analysis of η_c pseudoscalar mesons. It is remarkable that in this case $\chi^2/d.o.f \sim 0.36$ which means that the fit is almost perfect. On the other hand, with the values reported in Tab. 5.14 we are able to predict a

experiment	# data in fit	χ^2
r_{η_c}[166]	1	0.67
BaBar [164]	11	3.97
TOTAL:	12	4.64

TABLE 5.14: Data sets used in our global analysis for η_c, the individual χ^2 values, and the total χ^2 of the fit.

charge radii for η_c mesons, $r_{\eta_c}^{\rm fit}$, of

$$r_{\eta_c}^{\rm fit} = 1.04\, r_{\eta_c}\,. \tag{5.28}$$

in the context of the AM.

In Figure 5.14 we depicted the obtained results for EFF and TFF for η_c. We plot in the left-hand side, our findings of η_c EFF and the predictions within Lattice, a Contact Interaction (CI) model and the AM in the overlap representation. Likewise pions and kaons, we reported error bands related of 5% variation in r_{η_c}; this variation is also reported in the TFF depicted in the right-hand side. In the case of TFF we show, on the right-hand side, the results of our study, the prediction of the SDEs and NLO nrQCD. In this particular scenario, we can distinguish that our results also agree with BaBar measurements and SDEs predictions.

5.4.3.4 The η_b case

The heaviest constituent quark in a meson is the b quark, therefore, we proceed with the study the dynamics of the b quark, through the EFF and TFF of η_b.

In the case of η_b mesons there are no experimental data to perform a data-driven global fit. Hence, in order to study EFF and TFF we proceed with phenomenological inputs. In particular, we use the expected charge radii for the η_b EFF from Ref. [166], which reports that the $r_{\eta_b} = 0.086$ fm. On the other hand, for TFF of η_b mesons, we used predictions coming from SDEs and, similar to η_c we compared our results with the NNLO nrQCD predictions. We allow estimated errors around 5% of the central value determined by SDEs. Then, we present in Tab. 5.15 the results of the phenomelogical fit of η_b TFF and EFF. We find a tendency slightly far from unity of ν_{η_b} around 27% and almost no deviation from the reported mass in Ref. [173]. The values

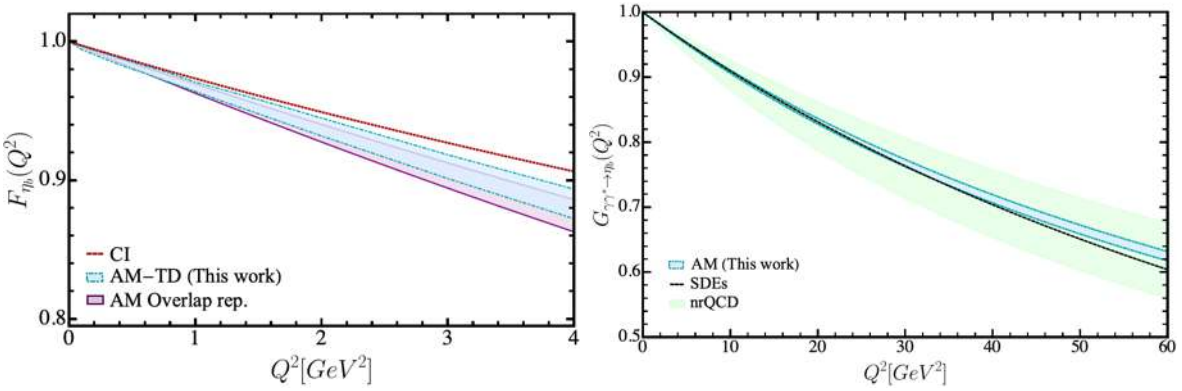

FIGURE 5.15: η_b EFF and TFF. Left panel- η_b EFF. The blue band represents our results with the parameters of Table 5.15. For comparison, we have included the following results: The light purple band that represents the η_b previous AM results from the overlap representation presented in [27]; the SDE-driven predictions in the contact interaction (CI) model (dotted dark red line) [28]. Right panel- η_b TFF; the blue light band corresponds to our TFFs results; the (black) dashed line corresponds to the SDEs results [111]; the light green band corresponds to NNLO nrQCD result for η_b (the band width expresses the sensitivity to the factorisation scale) from [172].

m_b	m_{η_b}	ν_{η_b}	$\alpha_b^{(0)}$
5.3443	9.3886	1.2743	0.1004

TABLE 5.15: Best fitted values for η_b meson in the AM. Masses are in GeV.

presented previously hits an almost perfect agreement between the phenomenological values and AM predictions. This can be appreciated in Tab. 5.16 were we reported a $\chi^2/d.o.f. \sim 10^{-3}$. The almost perfect agreement is depicted in Figure 5.15, where EFF

experiment	# data in fit	χ^2
r_{η_b}[166]	1	0.006
SDEs [111]	12	0.004
TOTAL:	11	0.01

TABLE 5.16: Data sets used in our global analysis for η_b, the individual χ^2 values, and the total χ^2 of the fit.

and TFF of η_b are plotted. We recall that the reported bands correspond to a variation of r_{η_b} of around 5%; this result is directly plotted in the TFF prediction. In the case of EFF, we find that,

$$r_{\eta_b}^{\text{fit}} = 0.99\, r_{\eta_b} \tag{5.29}$$

in perfect accordance. Regarding TFF, we present in the right hand side of Figure 5.15 our results, SDEs and NNLO nrQCD projections which all agree almost perfect.

Chapter 6

Discussion of results and conclusions

This chapter outlines the findings and conclusions of the study, as well as the practical implications that can be drawn from the results.

6.1 Summary and discussion

In this thesis, we put forward a fairly general AM for the pseudoscalar meson BSWF, which preserves its primary attractive feature of guaranteeing most calculations continue to be analytic. And, in addition we compare some of the results using a previous CI treatment.

For systematic and visual clarity, we italicize its main features and our key results in the following.

First corresponding to our AM:

- The key functions of the model are the spectral density $\rho_{\mathrm{M}}(w)$ and $\Lambda(w)$, which play the defining role for the dominant BSA, Eq. (3.82), of the pseudo-scalar mesons we study.
- The function $\Lambda(w)$, defined through Eq. (3.83), is quadratic in w which is as high as we can go in the power of this polynomial while still preserving the analytic nature of the calculations involved. In all previous models, $\Lambda(w)$ was merely taken as a constant mass scale Λ.

- Allowing Λ to become a function of the variable w allows us to connect LFWF with PDA algebraically, Eq. (4.8), without having the need to rather arbitrarily concoct the spectral density.

- Despite having emphasized the previous point, the fact remains that the spectral density can be extracted unequivocally through the knowledge of the PDA.

- Given the most up to date pseudo-scalar meson PDAs, we merely need to fix ν and $M_{q,\bar{h}}$. As $\nu = 1$ is a natural choice, we can safely say that the quark mass is the only free parameter to fix the model.

Corresponding the chapter 4 regarding the light-cone formalism:

- Crucially, the measure of factorizability of x and $k_\perp$ in the LFWF is evident through Eqs. (3.83) and (4.8). An immediate consequence is the hadronic scale relation between the PDA and the PDF, Eq. (4.31). This factorization is completely reinstated in the chiral limit, thus reproducing known results [53–55, 101, 102] as a particular case.

- With the exception of the leading-twist PDAs (which are external inputs) and the charge radii (used as benchmarks to set the values of the constituent masses, M_q), the rest of the distributions and other quantities derived herein are predictions.

On the other hand, according to the Chapter 5, we have presented the calculation of EFFs and TFFs of mesons by solving the interaction vertex $\mathrm{M}\gamma\mathrm{M}$ and $\gamma\mathrm{M}\gamma^*$ respectively, what we know as triangle diagrams. We used the CI model to solve the respective scalar and pseudoscalar EFFs and the AM to solve the EFFs and the TFFs of pseudoscalar mesons.

The principal insights are the following.

- First, we present an exhaustive computation of EFFs employing the CI model for twenty ground state PS and S mesons. Note that the CI findings for light mesons and heavy quarkonia are already found in the literature as mentioned before [84, 85, 98, 99]. We include these results for the sake of completeness and as a guide to pin down the best parameters in order to explore heavy-light systems. We thus report first results on the latter mesons within this model/formalism. We

expect these new EFFs to be harder than the exact QCD predictions, especially for the PS mesons due to the necessary inclusion of the F-amplitude. We also anticipate the charge radii to be in the ballpark of a (20-25)% error in light of the results where comparison with realistic studies and/or experiment has been possible.

- Concerning the CI model we also, analyze the sensitivity of the evolution of the EFFs by a change in appropriate parameters to allow for a 5% variation in the charge radii of the corresponding mesons. The evolution band has been shown explicitly for π, K, σ and η_c alone to avoid over-crowding in other collective plots. However, it is worth mentioning that the corresponding bands in other EFFs are almost identical. Interpolations have also been provided in Eqs. (5.13, 5.9) and Tables 5.6 and 5.4 which allow for a convenient algebraic analysis of the behavior of the EFFs in the momentum range that we mentioned above and for any application the reader may deem useful.

- Concerning the AM we carried out a global phenomenological analysis. Using experimental data and phenomenological contributions, we resorted to the minimization of χ^2 to obtain our best parameters: m_q, $m_{\rm M}$, $\nu_{\rm M}$ and $\alpha_q^{(0)}$. In addition, we added error bands obtained by allowing a variation of the 5% on the charge radii of the EFF only.

- For all the mesons, in the AM we obtained a $\chi^2/d.o.f.$ small, the largest being 1.93 corresponding to the pion given the large number of data found for this meson and the difference with BaBar data of the TFFs at large Q^2. Besides, in the case of the pion, we observe that our predictions of the EFFs at large energy scales are in agreement with the results of the SDEs and in turn have the behavior expected by the projected EIC and JLab at 12 GeV and 22 GeV. On the other hand, in the case of the kaon, we have that our predictions are again in good agreement with those obtained by the SDEs even at a higher energy scale than those normally reported, unlike CI. In turn, they are in almost perfect agreement with the new JLab experimental data which go up to a Q^2 of 5.5 GeV.

- Now, regarding the quarkonia mesons, we first have that the only experimental data corresponds to the BaBar Collaboration for the η_c TFFs, which our predictions are in complete agreement. However, our results for η_c differ to a greater extent with the CI predictions, to a small extent with the nrQCD predictions, and to an even lesser extent with those obtained by SDEs at large energy scales.

- Finally, for the η_b meson we do not have experimental data with which we can compare. However, our theoretical predictions are in complete agreement with those obtained by the SDEs, the previous AM and NNLO nrQCD.

6.2 Conclusions

Notably, our naive model faithfully reproduces previously known results concerning pions [103–105]. Our findings for the kaon are slightly different from those reported therein but can readily and correctly be attributed to the larger strange quark mass favored by this model. However, the description of pion and kaon is compatible with our experimental understanding of these mesons. It is worth mentioning that our pion valence-quark PDF is also compatible with the results from Ref. [174], in which the authors also obtain a NIR for the BSWF, but through the resolution of the corresponding BSE (modeling some of the ingredients that go into the latter). Novel results employing sophisticated mathematical techniques also validate the NIR approach [175]. The distributions reported for η_c and η_b, and other related quantities, are a completely novel feature of our study. In general, when a comparison is possible, our results also show agreement with other theoretical treatments such as SDEs, lattice QCD, as well as with experimental results. The structure of π^0, η_c and η_b is currently being investigated within this model, via two photon transition form factors.

In the study of the EFFs and TFFs by solving the respective vertex of interaction we conclude for our AM that except for BaBar data of the TFFs at large Q^2, our results compare favorably with all the available data, as well as with the SDEs. Moreover, the used AM has allowed us to calculate and extract EFFs and TFFs of pseudoscalar mesons, obtaining results that are close to reality, and being a first approximation of the complete theory, something that is further from the range of contact interaction, which was expected. However, it is of great help to visualize the effects that different approaches can have on a process. For this reason, we intend to continue exploiting the AM to extract all the theoretical information that it can provide us for example now for baryons.

Appendix A

General conventions

The conventions used in this thesis are the following:

- ***Dirac Matrices***

$$\{\gamma^\mu, \gamma^\nu\} = 2\eta^{\mu\nu}\,, \tag{A.1}$$

$$\gamma^\mu\gamma_\mu = 4I_4\,, \tag{A.2}$$

$$\{\gamma^5, \gamma^\nu\} = 0\,, \tag{A.3}$$

$$(\gamma^5)^2 = 1\,, \tag{A.4}$$

$$\gamma^\mu = \begin{pmatrix} 0 & \bar{\sigma}^\mu \\ \sigma^\mu & 0 \end{pmatrix}\,, \tag{A.5}$$

$$\sigma^\mu = (1, \vec{\sigma})\,, \qquad \bar{\sigma}^\mu = (1, -\vec{\sigma})\,, \tag{A.6}$$

  where σ^i are the Pauli matrices. And the $\sigma^{\mu\nu}$ tensor is defined as:

$$\sigma^{\mu\nu} = \frac{i}{2}[\gamma^\mu, \gamma^\nu]\,. \tag{A.7}$$

- ***Gamma Matrix Traces***

$$Tr[\gamma^\mu] = Tr[\gamma^5] = Tr[\gamma^5\gamma^\mu] = Tr[\gamma^{\mu_1}\gamma^{\mu_2}\ldots\gamma^{\mu_{2n+1}}] = 0\,, \tag{A.8}$$

$$Tr[\gamma^\mu\gamma^\nu] = 4\eta^{\mu\nu}\,, \tag{A.9}$$

$$Tr[\gamma^\mu\gamma^\nu\gamma^\alpha\gamma^\beta] = 4[\eta^{\mu\nu}\eta^{\alpha\beta} + \eta^{\mu\beta}\eta^{\nu\alpha} - \eta^{\mu\alpha}\eta^{\nu\beta}]\,, \tag{A.10}$$

$$\tag{A.11}$$

- ***Euclidean time vs. Minkowskian time***

  The Schwinger-Dyson equations (SDEs) are typically solved in Euclidean space, allowing us to employ a Wick rotation to transform the problem from Minkowski space to Euclidean space. To effect this change of spaces, we introduce momentum variables in Euclidean space (k_1, k_2, k_3, k_4) through the variable transformation:

$$k_4 = ik^0\,,\ \mathbf{k}^E = \mathbf{k}^M\,, \tag{A.12}$$

  where the subscripts E and M denote Euclidean and Minkowski spaces, respectively, for any vector in configuration or momentum space. This implies that to study inner products, an effective set of rules is used.

Minkowski		**Euclideano**
$\int_M d^4k$	$\rightarrow$	$i\int_E d^4k$
$\not{p}$	$\rightarrow$	$-i\gamma\cdot p$
$k\cdot p$	$\rightarrow$	$-k\cdot p$
p^μ	$\rightarrow$	$-ip^\mu$
$g^{\mu\nu}$	$\rightarrow$	$\delta_{\mu\nu}$
γ^μ	$\rightarrow$	γ_μ

  Where $\delta_{\mu\nu}$ is the Kronecker delta, and the Dirac matrices satisfy that

$$\{\gamma_\mu\,,\gamma_\nu\} = 2\delta_{\mu\nu}\,,\quad \gamma_\mu^\dagger = \gamma_\mu\,,\quad \gamma_5 = -\gamma_1\gamma_2\gamma_3\gamma_4\,, \tag{A.13}$$

- ***Light cone variables***

  The lightcone variables associated with a four-vector:

$$z^\mu = (z^+, \mathbf{z}_\perp, z^-) = (z^+, z^1, z^2, z^-)\,, \tag{A.14}$$

  are established as:

$$z^\pm = \frac{(z^0 \pm z^3)}{\sqrt{2}}\,, \qquad \mathbf{z}_\perp = (z^1, z^2)\,. \tag{A.15}$$

Appendix B

Feynman parameterization and Momentum integrals

In this appendix, we introduce a crucial integration technique known as Feynman parametrization, which simplifies integrals involving high powers in the denominator. Furthermore, we provide an explanation of our approach for resolving the moment integrals encountered.

First, it can be shown that the Feynman parameterization for n non-repeated denominators and also, different exponents for a $Re[\nu_j] > 0$ and $1 < j < n$ would be:

$$\frac{1}{A_1^{\nu_1} A_2^{\nu_1} \cdots A_n^{\nu_n}} = \frac{\Gamma(\nu_1 + \ldots \nu_n)}{\Gamma(\nu_1) \cdots \Gamma(\nu_n)} \int_0^1 du_1 \cdots \int_0^1 du_n \frac{\delta[1 - \sum_{j=1}^n u_j] u_1^{\nu_1 - 1} \cdots u^{\nu_n - 1}}{[\sum_{j=1}^n u_j A_j]^{\sum_{j=1}^n \nu_j}} \,. \tag{B.1}$$

where Γ is the Gamma function.

In this thesis, we typically encounter more intricate integrals due to the specific structure of the A's terms, often of the form:

$$\prod_{i=1}^{N} f_i(t; p_i, b_i, w_i) \sim \frac{1}{(t^2 + 2b_1 \cdot p_1 + w_1)^{\beta_1}} \times \cdots \times \frac{1}{(t^2 + 2b_N \cdot p_N + w_N)^{\beta_N}} \,. \tag{B.2}$$

Using Feynman parametrization, the denominators can take form: $[u_1 A_1 + u_2 A_2 + \ldots (1 - u_1 - \ldots u_n) A_n]^{\sum_{j=1}^{n} \nu_j}$, and according to the Feynman parameters and the moments the integrating became as:

$$\prod_{i=1}^{N} f_i(t; p_i, a_i, \tilde{m}) \sim \frac{1}{\{t^2 + 2t \cdot [a_1(\tilde{x} p_1) + \ldots + a_N(\tilde{x} p_N)] + \tilde{m}^2(\tilde{x}, w_i)\}^{\beta_1 + \ldots \beta_N}} \,, \tag{B.3}$$

where $a_i(\tilde{x})$ and $\tilde{m}^2(\tilde{x}, w_i)$ are constants that depend on the Feynman parameters and the w_i. Thus, if we consider the following:

$$\begin{aligned} c &= a_1(\tilde{x}) p_1 + \ldots + a_N(\tilde{x}) \,, \\ \Omega &= \tilde{m}^2 - c^2 \,, \\ \beta &= \beta_1 + \ldots + \beta_N \,. \end{aligned} \tag{B.4}$$

And, take the change of variable $t \to t - c$ we would arrive to:

$$\prod_{i=1}^{N} f_i(t; p_i, \Omega) \sim \frac{1}{(t^2 + \Omega^2)^{\beta}} \,. \tag{B.5}$$

Finally, we can analitycally solve the momentum integral using:

$$\int \frac{d^4 t}{(2\pi)^4} \frac{(t^2)^{\alpha}}{[t^2 + a^2]^{\beta}} = \frac{1}{(4\pi)^2} \frac{\Gamma[\beta - \alpha - 2] \Gamma[\alpha + 2]}{\Gamma[\beta] \Gamma[2]} (a^2)^{\alpha - \beta + 2} \,. \tag{B.6}$$

for $\alpha - \beta + 2 > 0$.

Appendix C

Acronyms

QCD: Quantum Chromodynamics
DCSB: Dynamical Chiral Symmetry Breaking
DIS: Deep inelastic scattering
EFFs: Electromagnetic Form Factors
PDFs: Parton Distribution Functions
GPDs: Generalized Parton Distribution Functions
DVCS: Deeply virtual Compton scattering
TFFs: Transition Form Factors
SDEs: Swchiger-Dyson Equations
BSE: Bethe-Salpeter Equation
BSA: Bethe-Salpeter Amplitude
BSWF: Bethe-Salpeter Wave Function
CI: Contact Interaction
AM: Algebraic Model
PDA: Parton Distribution Amplitude
LC: Light-Cone
LFWF: Light Front Wave Function
WTI: Ward Takahashi Identities
PS: Pseudo-scalars
V: Vectors
AV: Axial-Vectors

List of Publications

Articles Published in International Journals

1. **"Pseudo-scalar mesons: light front wave functions, GPDs and PDFs"**, L. Albino, I.M. Higuera-Angulo, K. Raya, A. Bashir. Phys. Rev. D106 (2022) 3, 034003 • e- Print: 2207.06550 [hep-ph].

2. **"Electromagnetic form factors and charge radii of pseudoscalar and scalar mesons: A comprehensive contact interaction analysis"**, R.J. Hernández-Pinto, L.X. Gutiérrez-Guerrero, A. Bashir, M.A. Bedolla, I.M. Higuera-Angulo. Phys.Rev.D 107 (2023) 5, 054002 • e- Print 2301.11881 [hep-ph].

3. **"Data-driven algebraic model computation of electromagnetic and transition form factors of pseudoscalar mesons to $\gamma\gamma^*$"**, I.M. Higuera-Angulo, A. Bashir, R.J. Hernandez-Pinto, K. Raya. **Status:** Approaching the conclusion of the writing process.

4. **"Electric, Magnetic and Quadrupolar Form Factors of Vector Mesons: From the light to heavy sector"**, R. J. Hernández-Pinto, L. X. Gutiérrez-Guerrero, A. Bashir, M. A. Bedolla, and I. M. Higuera-Angulo. **Status:** Approaching the conclusion of the writing process.

5. **"Strong Interaction Physics at the Luminosity Frontier with 22 GeV Electrons at Jefferson Lab"**, A. Accardi, P. Achenbach, W. Armstrong, and others. JLAB-PHY-23-3840, JLAB-THY-23-3848 • e-Print: 2306.09360 [nucl-ex]

Proceedings in International Conferences

1. **"Internal structure of pion and kaon: an algebraic model and its implications"**, I.M. Higuera-Angulo, L. Albino, K. Raya, A. Bashir. Rev. Mex. Fis. Suppl. 3 (2022) 3, 0308107 • Contribution to: HADRON 2021.

References

[1] Stanley Brodsky et al. "QCD and Hadron Physics". In: (Feb. 2015).

[2] F. Englert and R. Brout. "Broken Symmetry and the Mass of Gauge Vector Mesons". In: *Phys. Rev. Lett.* 13 (9 Aug. 1964), pp. 321–323. DOI: 10.1103/PhysRevLett.13.321. URL: https://link.aps.org/doi/10.1103/PhysRevLett.13.321.

[3] Craig D. Roberts. "Perspective on the Origin of Hadron Masses". In: *Few-Body Systems* 58.1 (Dec. 2016), p. 5. ISSN: 1432-5411. DOI: 10.1007/s00601-016-1168-z. URL: https://doi.org/10.1007/s00601-016-1168-z.

[4] Kenneth G. Wilson. "Confinement of quarks". In: *Phys. Rev. D* 10 (8 Oct. 1974), pp. 2445–2459. DOI: 10.1103/PhysRevD.10.2445. URL: https://link.aps.org/doi/10.1103/PhysRevD.10.2445.

[5] John M. Cornwall and George Tiktopoulos. "Infrared Behavior of Nonabelian Gauge Theories. 2." In: *Phys. Rev. D* 15 (1977), p. 2937. DOI: 10.1103/PhysRevD.15.2937.

[6] H. J. Munczek and A. M. Nemirovsky. "Ground-state $q\bar{q}$ mass spectrum in quantum chromodynamics". In: *Phys. Rev. D* 28 (1 July 1983), pp. 181–186. DOI: 10.1103/PhysRevD.28.181. URL: https://link.aps.org/doi/10.1103/PhysRevD.28.181.

[7] H. David Politzer. "Reliable Perturbative Results for Strong Interactions?" In: *Phys. Rev. Lett.* 30 (26 June 1973), pp. 1346–1349. DOI: 10.1103/PhysRevLett.30.1346. URL: https://link.aps.org/doi/10.1103/PhysRevLett.30.1346.

[8] David J. Gross and Frank Wilczek. "Asymptotically Free Gauge Theories. I". In: *Phys. Rev. D* 8 (10 Nov. 1973), pp. 3633–3652. DOI: 10.1103/PhysRevD.8.3633. URL: https://link.aps.org/doi/10.1103/PhysRevD.8.3633.

[9] David J. Gross and Frank Wilczek. "Ultraviolet Behavior of Non-Abelian Gauge Theories". In: *Phys. Rev. Lett.* 30 (26 June 1973), pp. 1343–1346. DOI: 10.1103/PhysRevLett.30.1343. URL: https://link.aps.org/doi/10.1103/PhysRevLett.30.1343.

[10] G. Peter Lepage and Stanley J. Brodsky. "Exclusive processes in perturbative quantum chromodynamics". In: *Phys. Rev. D* 22 (9 Nov. 1980), pp. 2157–2198. DOI: 10.1103/PhysRevD.22.2157. URL: https://link.aps.org/doi/10.1103/PhysRevD.22.2157.

[11] S.R. Amendolia et al. "A measurement of the space-like pion electromagnetic form factor". In: *Nuclear Physics B* 277 (1986), pp. 168–196. ISSN: 0550-3213. DOI: https://doi.org/10.1016/0550-3213(86)90437-2. URL: https://www.sciencedirect.com/science/article/pii/0550321386904372.

[12] H. Ackermann et al. "Determination of the longitudinal and the transverse part in + electroproduction". In: *Nuclear Physics B* 137.3 (1978), pp. 294–300. ISSN: 0550-3213. DOI: https://doi.org/10.1016/0550-3213(78)90523-0. URL: https://www.sciencedirect.com/science/article/pii/0550321378905230.

[13] J. Volmer et al. "Measurement of the Charged Pion Electromagnetic Form-Factor". In: *Phys. Rev. Lett.* 86 (2001), pp. 1713–1716. DOI: 10.1103/PhysRevLett.86.1713. arXiv: nucl-ex/0010009.

[14] T. Horn et al. "Determination of the Charged Pion Form Factor at Q**2 = 1.60 and 2.45-(GeV/c)**2". In: *Phys. Rev. Lett.* 97 (2006), p. 192001. DOI: 10.1103/PhysRevLett.97.192001. arXiv: nucl-ex/0607005.

[15] G. M. Huber et al. "Charged pion form-factor between Q**2 = 0.60-GeV**2 and 2.45-GeV**2. II. Determination of, and results for, the pion form-factor". In: *Phys. Rev. C* 78 (2008), p. 045203. DOI: 10.1103/PhysRevC.78.045203. arXiv: 0809.3052 [nucl-ex].

[16] H. J. Behrend et al. "A Measurement of the pi0, eta and eta-prime electromagnetic form-factors". In: *Z. Phys. C* 49 (1991), pp. 401–410. DOI: 10.1007/BF01549692.

[17] J. Gronberg et al. "Measurements of the meson-photon transition form factors of light pseudoscalar mesons at large momentum transfer". In: *Phys. Rev. D* 57 (1 Jan. 1998), pp. 33–54. DOI: 10.1103/PhysRevD.57.33. URL: https://link.aps.org/doi/10.1103/PhysRevD.57.33.

[18] B. Aubert et al. "Measurement of the $\gamma\gamma^* \to \pi^0$ transition form factor". In: *Phys. Rev. D* 80 (5 Sept. 2009), p. 052002. DOI: 10.1103/PhysRevD.80.052002. URL: https://link.aps.org/doi/10.1103/PhysRevD.80.052002.

[19] S. Uehara et al. "Measurement of $\gamma\gamma^* \to \pi^0$ transition form factor at Belle". In: *Phys. Rev. D* 86 (9 Nov. 2012), p. 092007. DOI: 10.1103/PhysRevD.86.092007. URL: https://link.aps.org/doi/10.1103/PhysRevD.86.092007.

[20] Ryosuke Itoh. "Status of Belle II and Physics Prospects". In: *Nuclear and Particle Physics Proceedings* 285-286 (2017). Sixth Workshop on Theory, Phenomenology and Experiments in Flavour Physics Interplay of Flavour Physics with Electroweak symmetry breaking, pp. 155–159. ISSN: 2405-6014. DOI: https://doi.org/10.1016/j.nuclphysbps.2017.03.028. URL: https://www.sciencedirect.com/science/article/pii/S2405601417300846.

[21] Arlene C. Aguilar et al. "Pion and Kaon Structure at the Electron-Ion Collider". In: *Eur. Phys. J. A* 55.10 (2019), p. 190. DOI: 10.1140/epja/i2019-12885-0. arXiv: 1907.08218 [nucl-ex].

[22] Tanja Horn. "Meson Form Factors and Deep Exclusive Meson Production Experiments". In: *EPJ Web Conf.* 137 (2017). Ed. by Y. Foka, N. Brambilla, and V. Kovalenko, p. 05005. DOI: 10.1051/epjconf/201713705005.

[23] G. M. Huber, D. Gaskell, et al. "Measurement of the Charged Pion Form Factor to High Q^2". In: *approved Jefferson Lab 12 GeV Experiment E12-06-101* (2006). Ed. by Jefferson Lab PAC 30 Proposal. DOI: https://www.jlab.org/exp_prog/proposals/06/PR12-06-101.pdf.

[24] T. Horn, G.M. Huber, et al. "Scaling Study of the L-T Separated Pion Electroproduction Cross Section at 11 GeV". In: *approved Jefferson Lab 12 GeV Experiment E12-07-105* (2007).

[25] A. Accardi et al. "Strong Interaction Physics at the Luminosity Frontier with 22 GeV Electrons at Jefferson Lab". In: (June 2023). arXiv: 2306.09360 [nucl-ex].

[26] F. J. Dyson. "The S matrix in quantum electrodynamics". In: *Phys. Rev.* 75 (1949), pp. 1736–1755. DOI: 10.1103/PhysRev.75.1736.

[27] L. Albino et al. "Pseudoscalar mesons: Light front wave functions, GPDs, and PDFs". In: *Phys. Rev. D* 106.3 (2022), p. 034003. DOI: 10.1103/PhysRevD.106.034003. arXiv: 2207.06550 [hep-ph].

[28] R. J. Hernández-Pinto et al. "Electromagnetic form factors and charge radii of pseudoscalar and scalar mesons: A comprehensive contact interaction analysis". In: *Phys. Rev. D* 107.5 (2023), p. 054002. DOI: 10.1103/PhysRevD.107.054002. arXiv: 2301.11881 [hep-ph].

[29] Professor E. Rutherford F.R.S. "LXXIX. The scattering of and particles by matter and the structure of the atom". In: *The London, Edinburgh, and Dublin Philosophical Magazine and Journal of Science* 21.125 (1911), pp. 669–688. DOI: 10.1080/14786440508637080. eprint: https://doi.org/10.1080/14786440508637080. URL: https://doi.org/10.1080/14786440508637080.

[30] R. Frisch and O. Stern. "Über die magnetische Ablenkung von Wasserstoffmolekülen und das magnetische Moment des Protons. I". In: *Zeitschrift für Physik* 85.1 (Jan. 1933), pp. 4–16. ISSN: 0044-3328. DOI: 10.1007/BF01330773. URL: https://doi.org/10.1007/BF01330773.

[31] R. Hofstadter, H. R. Fechter, and J. A. McIntyre. "High-Energy Electron Scattering and Nuclear Structure Determinations". In: *Phys. Rev.* 92 (4 Nov. 1953), pp. 978–987. DOI: 10.1103/PhysRev.92.978. URL: https://link.aps.org/doi/10.1103/PhysRev.92.978.

[32] Robert Hofstadter. "Electron scattering and nuclear structure". In: *Rev. Mod. Phys.* 28 (1956), pp. 214–254. DOI: 10.1103/RevModPhys.28.214.

[33] Murray Gell-Mann. "The Eightfold Way: A Theory of strong interaction symmetry". In: (Mar. 1961). DOI: 10.2172/4008239.

[34] E. D. Bloom et al. "High-Energy Inelastic $e-p$ Scattering at 6° and 10°". In: *Phys. Rev. Lett.* 23 (16 Oct. 1969), pp. 930–934. DOI: 10.1103/PhysRevLett.23.930. URL: https://link.aps.org/doi/10.1103/PhysRevLett.23.930.

[35] M. Breidenbach et al. "Observed Behavior of Highly Inelastic Electron-Proton Scattering". In: *Phys. Rev. Lett.* 23 (16 Oct. 1969), pp. 935–939. DOI: 10.1103/PhysRevLett.23.935. URL: https://link.aps.org/doi/10.1103/PhysRevLett.23.935.

[36] J. D. Bjorken. "Asymptotic Sum Rules at Infinite Momentum". In: *Phys. Rev.* 179 (5 Mar. 1969), pp. 1547–1553. DOI: 10.1103/PhysRev.179.1547. URL: https://link.aps.org/doi/10.1103/PhysRev.179.1547.

[37] J. D. Bjorken and E. A. Paschos. "Inelastic Electron-Proton and γ-Proton Scattering and the Structure of the Nucleon". In: *Phys. Rev.* 185 (5 Sept. 1969), pp. 1975–1982. DOI: 10.1103/PhysRev.185.1975. URL: https://link.aps.org/doi/10.1103/PhysRev.185.1975.

[38] Richard P. Feynman. "Very High-Energy Collisions of Hadrons". In: *Phys. Rev. Lett.* 23 (24 Dec. 1969), pp. 1415–1417. DOI: 10.1103/PhysRevLett.23.1415. URL: https://link.aps.org/doi/10.1103/PhysRevLett.23.1415.

[39] C. G. Callan and David J. Gross. "High-Energy Electroproduction and the Constitution of the Electric Current". In: *Phys. Rev. Lett.* 22 (4 Jan. 1969), pp. 156–159. DOI: 10.1103/PhysRevLett.22.156. URL: https://link.aps.org/doi/10.1103/PhysRevLett.22.156.

[40] V. Khachatryan et al. "Measurement of the inclusive 3-jet production differential cross section in proton–proton collisions at 7 TeV and determination of the strong coupling constant in the TeV range". In: *The European Physical Journal C* 75.5 (May 2015), p. 186. ISSN: 1434-6052. DOI: 10.1140/epjc/s10052-015-3376-y. URL: https://doi.org/10.1140/epjc/s10052-015-3376-y.

[41] G. Peter Lepage and Stanley J. Brodsky. "Exclusive Processes in Perturbative Quantum Chromodynamics". In: *Phys. Rev. D* 22 (1980), p. 2157. DOI: 10.1103/PhysRevD.22.2157.

[42] V. N. Gribov and L. N. Lipatov. "Deep inelastic e p scattering in perturbation theory". In: *Sov. J. Nucl. Phys.* 15 (1972). [Yad. Fiz.15,781(1972)], pp. 438–450.

[43] Guido Altarelli and G. Parisi. "Asymptotic Freedom in Parton Language". In: *Nucl. Phys. B* 126 (1977), pp. 298–318. DOI: 10.1016/0550-3213(77)90384-4.

[44] A. V. Radyushkin. "Scaling limit of deeply virtual Compton scattering". In: *Phys. Lett. B* 380 (1996), pp. 417–425. DOI: 10.1016/0370-2693(96)00528-X. arXiv: hep-ph/9604317.

[45] Xiang-Dong Ji. "Gauge-Invariant Decomposition of Nucleon Spin". In: *Phys. Rev. Lett.* 78 (1997), pp. 610–613. DOI: 10.1103/PhysRevLett.78.610. arXiv: hep-ph/9603249.

[46] M. Diehl et al. "The overlap representation of skewed quark and gluon distributions". In: *Nucl. Phys. B* 596 (2001). [Erratum: Nucl.Phys.B 605, 647–647 (2001)], pp. 33–65. DOI: 10.1016/S0550-3213(00)00684-2. arXiv: hep-ph/0009255.

[47] Matthias Burkardt. "Impact parameter space interpretation for generalized parton distributions". In: *Int. J. Mod. Phys. A* 18 (2003), pp. 173–208. DOI: 10.1142/S0217751X03012370. arXiv: hep-ph/0207047.

[48] M. Diehl. "Generalized parton distributions". In: *Phys. Rept.* 388 (2003), pp. 41–277. DOI: 10.1016/j.physrep.2003.08.002. arXiv: hep-ph/0307382.

[49] A. V. Belitsky and A. V. Radyushkin. "Unraveling hadron structure with generalized parton distributions". In: *Phys. Rept.* 418 (2005), pp. 1–387. DOI: 10.1016/j.physrep.2005.06.002. arXiv: hep-ph/0504030.

[50] Michel Guidal, Hervé Moutarde, and Marc Vanderhaeghen. "Generalized Parton Distributions in the valence region from Deeply Virtual Compton Scattering". In: *Rept. Prog. Phys.* 76 (2013), p. 066202. DOI: 10.1088/0034-4885/76/6/066202. arXiv: 1303.6600 [hep-ph].

[51] Martha Constantinou et al. "Parton distributions and lattice-QCD calculations: Toward 3D structure". In: *Prog. Part. Nucl. Phys.* 121 (2021), p. 103908. DOI: 10.1016/j.ppnp.2021.103908. arXiv: 2006.08636 [hep-ph].

[52] N. Chouika et al. "Covariant Extension of the GPD overlap representation at low Fock states". In: *Eur. Phys. J. C* 77.12 (2017), p. 906. DOI: 10.1140/epjc/s10052-017-5465-6. arXiv: 1711.05108 [hep-ph].

[53] N. Chouika et al. "A Nakanishi-based model illustrating the covariant extension of the pion GPD overlap representation and its ambiguities". In: *Phys. Lett. B* 780 (2018), pp. 287–293. DOI: 10.1016/j.physletb.2018.02.070. arXiv: 1711.11548 [hep-ph].

[54] J. M. Morgado Chávez et al. "Accessing the pion 3D structure at US and China Electron-Ion Colliders". In: (Oct. 2021). arXiv: 2110.09462 [hep-ph].

[55] José Manuel Morgado Chavez et al. "Pion GPDs: A path toward phenomenology". In: (Oct. 2021). arXiv: 2110.06052 [hep-ph].

[56] Julian S. Schwinger. "On the Green's functions of quantized fields. 1." In: *Proc. Nat. Acad. Sci.* 37 (1951), pp. 452–455. DOI: 10.1073/pnas.37.7.452.

[57] Julian S. Schwinger. "On the Green's functions of quantized fields. 2." In: *Proc. Nat. Acad. Sci.* 37 (1951), pp. 455–459. DOI: 10.1073/pnas.37.7.455.

[58] Si-xue Qin and Craig D Roberts. "Impressions of the Continuum Bound State Problem in QCD". In: *Chin. Phys. Lett.* 37.12 (2020), p. 121201. DOI: 10.1088/0256-307X/37/12/121201. arXiv: 2008.07629 [hep-ph].

[59] Craig D. Roberts and Anthony G. Williams. "Dyson-Schwinger equations and their application to hadronic physics". In: *Progress in Particle and Nuclear Physics* 33 (1994), pp. 477–575. ISSN: 0146-6410. DOI: https://doi.org/10.1016/0146-6410(94)90049-3. URL: https://www.sciencedirect.com/science/article/pii/0146641094900493.

[60] Kenneth G. Wilson. "Confinement of Quarks". In: *Phys. Rev. D* 10 (1974). Ed. by J. C. Taylor, pp. 2445–2459. DOI: 10.1103/PhysRevD.10.2445.

[61] G. Peter Lepage et al. "Improved nonrelativistic QCD for heavy-quark physics". In: *Phys. Rev. D* 46 (9 Nov. 1992), pp. 4052–4067. DOI: 10.1103/PhysRevD.46.4052. URL: https://link.aps.org/doi/10.1103/PhysRevD.46.4052.

[62] E. E. Salpeter and H. A. Bethe. "A Relativistic Equation for Bound-State Problems". In: *Phys. Rev.* 84 (6 Dec. 1951), pp. 1232–1242. DOI: 10.1103/PhysRev.84.1232. URL: https://link.aps.org/doi/10.1103/PhysRev.84.1232.

[63] Murray Gell-Mann and Francis Low. "Bound States in Quantum Field Theory". In: *Phys. Rev.* 84 (2 Oct. 1951), pp. 350–354. DOI: 10.1103/PhysRev.84.350. URL: https://link.aps.org/doi/10.1103/PhysRev.84.350.

[64] Julian Schwinger. "The Theory of Quantized Fields. II". In: *Phys. Rev.* 91 (3 Aug. 1953), pp. 713–728. DOI: 10.1103/PhysRev.91.713. URL: https://link.aps.org/doi/10.1103/PhysRev.91.713.

[65] D. Lurié, A. J. Macfarlane, and Y. Takahashi. "Normalization of Bethe-Salpeter Wave Functions". In: *Phys. Rev.* 140 (4B Nov. 1965), B1091–B1099. DOI: 10.1103/PhysRev.140.B1091. URL: https://link.aps.org/doi/10.1103/PhysRev.140.B1091.

[66] Pieter Maris and Peter C. Tandy. "Bethe-Salpeter study of vector meson masses and decay constants". In: *Phys. Rev. C* 60 (5 Oct. 1999), p. 055214. DOI: 10.1103/PhysRevC.60.055214. URL: https://link.aps.org/doi/10.1103/PhysRevC.60.055214.

[67] Si-Xue Qin, Craig D. Roberts, and Sebastian M. Schmidt. "Ward–Green–Takahashi identities and the axial-vector vertex". In: *Physics Letters B* 733 (2014), pp. 202–208. ISSN: 0370-2693. DOI: https://doi.org/10.1016/j.physletb.2014.04.041. URL: https://www.sciencedirect.com/science/article/pii/S0370269314002810.

[68] A. Bashir et al. "Confinement and dynamical chiral symmetry breaking in QED3". In: *Phys. Rev. C* 78 (5 Nov. 2008), p. 055201. DOI: 10.1103/PhysRevC.78.055201. URL: https://link.aps.org/doi/10.1103/PhysRevC.78.055201.

[69] K. Raya et al. "Multiple solutions for the fermion mass function in QED3". In: *Phys. Rev. D* 88 (9 Nov. 2013), p. 096003. DOI: 10.1103/PhysRevD.88.096003. URL: https://link.aps.org/doi/10.1103/PhysRevD.88.096003.

[70] Si-xue Qin et al. "Interaction model for the gap equation". In: *Phys. Rev. C* 84 (2011), p. 042202. DOI: 10.1103/PhysRevC.84.042202. arXiv: 1108.0603 [nucl-th].

[71] I.L. Bogolubsky et al. "Lattice gluodynamics computation of Landau-gauge Green's functions in the deep infrared". In: *Physics Letters B* 676.1 (2009), pp. 69–73. ISSN: 0370-2693. DOI: https://doi.org/10.1016/j.physletb.2009.04.076. URL: https://www.sciencedirect.com/science/article/pii/S0370269309005206.

[72] A. C. Aguilar, D. Binosi, and J. Papavassiliou. "QCD effective charges from lattice data". In: *Journal of High Energy Physics* 2010.7 (July 2010), p. 2. ISSN: 1029-8479. DOI: 10.1007/JHEP07(2010)002. URL: https://doi.org/10.1007/JHEP07(2010)002.

[73] A. Ayala et al. "Quark flavor effects on gluon and ghost propagators". In: *Phys. Rev. D* 86 (7 Oct. 2012), p. 074512. DOI: 10.1103/PhysRevD.86.074512. URL: https://link.aps.org/doi/10.1103/PhysRevD.86.074512.

[74] A. C. Aguilar et al. "New method for determining the quark-gluon vertex". In: *Phys. Rev. D* 90 (6 Sept. 2014), p. 065027. DOI: 10.1103/PhysRevD.90.065027. URL: https://link.aps.org/doi/10.1103/PhysRevD.90.065027.

[75] A. Bashir et al. "Dynamical chiral symmetry breaking and the fermion–gauge-boson vertex". In: *Phys. Rev. C* 85 (4 Apr. 2012), p. 045205. DOI: 10.1103/PhysRevC.85.045205. URL: https://link.aps.org/doi/10.1103/PhysRevC.85.045205.

[76] Lei Chang, Yu-Xin Liu, and Craig D. Roberts. "Dressed-Quark Anomalous Magnetic Moments". In: *Phys. Rev. Lett.* 106 (7 Feb. 2011), p. 072001. DOI: 10.1103/PhysRevLett.106.072001. URL: https://link.aps.org/doi/10.1103/PhysRevLett.106.072001.

[77] A. I. Davydychev, P. Osland, and L. Saks. "Quark-gluon vertex in arbitrary gauge and dimension". In: *Phys. Rev. D* 63 (1 Dec. 2000), p. 014022. DOI: 10.1103/PhysRevD.63.014022. URL: https://link.aps.org/doi/10.1103/PhysRevD.63.014022.

[78] Pieter Maris and Peter C. Tandy. "Quark-photon vertex and the pion charge radius". In: *Phys. Rev. C* 61 (4 Mar. 2000), p. 045202. DOI: 10.1103/PhysRevC.61.045202. URL: https://link.aps.org/doi/10.1103/PhysRevC.61.045202.

[79] Lei Chang et al. "Imaging Dynamical Chiral-Symmetry Breaking: Pion Wave Function on the Light Front". In: *Phys. Rev. Lett.* 110 (13 Mar. 2013), p. 132001. DOI: 10.1103/PhysRevLett.110.132001. URL: https://link.aps.org/doi/10.1103/PhysRevLett.110.132001.

[80] Khépani Raya et al. "Structure of the neutral pion and its electromagnetic transition form factor". In: *Phys. Rev. D* 93 (7 Apr. 2016), p. 074017. DOI: 10.1103/PhysRevD.93.074017. URL: https://link.aps.org/doi/10.1103/PhysRevD.93.074017.

[81] Khépani Raya et al. "Partonic structure of neutral pseudoscalars via two photon transition form factors". In: *Phys. Rev. D* 95 (7 Apr. 2017), p. 074014. DOI: 10.1103/PhysRevD.95.074014. URL: https://link.aps.org/doi/10.1103/PhysRevD.95.074014.

[82] Minghui Ding et al. "Leading-twist parton distribution amplitudes of S-wave heavy-quarkonia". In: *Phys. Lett. B* 753 (2016), pp. 330–335. DOI: 10.1016/j.physletb.2015.11.075. arXiv: 1511.04943 [nucl-th].

[83] Noboru Nakanishi. "Partial-Wave Bethe-Salpeter Equation". In: *Phys. Rev.* 130 (3 May 1963), pp. 1230–1235. DOI: 10.1103/PhysRev.130.1230. URL: https://link.aps.org/doi/10.1103/PhysRev.130.1230.

[84] L. X. Gutierrez-Guerrero et al. "Pion form factor from a contact interaction". In: *Phys. Rev. C* 81 (2010), p. 065202. DOI: 10.1103/PhysRevC.81.065202. arXiv: 1002.1968 [nucl-th].

[85] Khepani Raya et al. "Heavy quarkonia in a contact interaction and an algebraic model: mass spectrum, decay constants, charge radii and elastic and transition form factors". In: *Few Body Syst.* 59.6 (2018), p. 133. DOI: 10.1007/s00601-018-1455-y. arXiv: 1711.00383 [nucl-th].

[86] H. L. L. Roberts et al. "Abelian anomaly and neutral pion production". In: *Phys. Rev. C* 82 (2010), p. 065202. DOI: 10.1103/PhysRevC.82.065202. arXiv: 1009.0067 [nucl-th].

[87] H. L. L. Roberts et al. "pi- and rho-mesons, and their diquark partners, from a contact interaction". In: *Phys. Rev. C* 83 (2011), p. 065206. DOI: 10.1103/PhysRevC.83.065206. arXiv: 1102.4376 [nucl-th].

[88] Chen Chen et al. "Features and flaws of a contact interaction treatment of the kaon". In: *Phys. Rev. C* 87 (2013), p. 045207. DOI: 10.1103/PhysRevC.87.045207. arXiv: 1212.2212 [nucl-th].

[89] Xiaobin Wang et al. "Pion scalar, vector, and tensor form factors from a contact interaction". In: *Phys. Rev. D* 106.5 (2022), p. 054016. DOI: 10.1103/PhysRevD.106.054016. arXiv: 2207.04339 [hep-ph].

[90] Patrick O. Bowman et al. "Unquenched gluon propagator in Landau gauge". In: *Phys. Rev. D* 70 (2004), p. 034509. DOI: 10.1103/PhysRevD.70.034509. arXiv: hep-lat/0402032.

[91] L. X. Gutiérrez-Guerrero et al. "Masses of Light and Heavy Mesons and Baryons: A Unified Picture". In: *Phys. Rev.* D100.11 (2019), p. 114032. DOI: 10.1103/PhysRevD.100.114032. arXiv: 1911.09213 [nucl-th].

[92] Ph. Boucaud et al. "The Infrared Behaviour of the Pure Yang-Mills Green Functions". In: *Few Body Syst.* 53 (2012), pp. 387–436. DOI: 10.1007/s00601-011-0301-2. arXiv: 1109.1936 [hep-ph].

[93] A. C. Aguilar et al. "Evidence of ghost suppression in gluon mass scale dynamics". In: *Eur. Phys. J.* C78.3 (2018), p. 181. DOI: 10.1140/epjc/s10052-018-5679-2. arXiv: 1712.06926 [hep-ph].

[94] Daniele Binosi and Joannis Papavassiliou. "Coupled dynamics in gluon mass generation and the impact of the three-gluon vertex". In: *Phys. Rev.* D97.5 (2018), p. 054029. DOI: 10.1103/PhysRevD.97.054029. arXiv: 1709.09964 [hep-ph].

[95] Fei Gao et al. "Locating the Gribov horizon". In: *Phys. Rev.* D97.3 (2018), p. 034010. DOI: 10.1103/PhysRevD.97.034010. arXiv: 1706.04681 [hep-ph].

[96] L. X. Gutiérrez-Guerrero, G. Paredes-Torres, and A. Bashir. "Mesons and baryons: Parity partners". In: *Phys. Rev. D* 104.9 (2021), p. 094013. DOI: 10.1103/PhysRevD.104.094013. arXiv: 2109.09058 [hep-ph].

[97] Pei-Lin Yin et al. "Masses of ground-state mesons and baryons, including those with heavy quarks". In: *Phys. Rev.* D100 (2019), p. 034008. DOI: 10.1103/PhysRevD.100.034008. arXiv: 1903.00160 [nucl-th].

[98] Marco A. Bedolla, J. J. Cobos-Martínez, and Adnan Bashir. "Charmonia in a contact interaction". In: *Phys. Rev.* D92.5 (2015), p. 054031. DOI: 10.1103/PhysRevD.92.054031. arXiv: 1601.05639 [hep-ph].

[99] Marco A. Bedolla et al. "η_c elastic and transition form factors: Contact interaction and algebraic model". In: *Phys. Rev. D* 93.9 (2016), p. 094025. DOI: 10.1103/PhysRevD.93.094025. arXiv: 1606.03760 [hep-ph].

[100] Pei-Lin Yin et al. "Masses of positive- and negative-parity hadron ground-states, including those with heavy quarks". In: *Eur. Phys. J. C* 81.4 (2021), p. 327. DOI: 10.1140/epjc/s10052-021-09097-6. arXiv: 2102.12568 [hep-ph].

[101] C. Mezrag, H. Moutarde, and J. Rodriguez-Quintero. "From Bethe–Salpeter Wave functions to Generalised Parton Distributions". In: *Few Body Syst.* 57.9 (2016), pp. 729–772. DOI: 10.1007/s00601-016-1119-8. arXiv: 1602.07722 [nucl-th].

[102] C. Mezrag et al. "Sketching the pion's valence-quark generalised parton distribution". In: *Phys. Lett. B* 741 (2015), pp. 190–196. DOI: 10.1016/j.physletb.2014.12.027. arXiv: 1411.6634 [nucl-th].

[103] Khépani Raya and José Rodríguez-Quintero. "Highlights of pion and kaon structure from continuum analyses". In: Apr. 2022. arXiv: 2204.01642 [hep-ph].

[104] Khepani Raya et al. "Revealing pion and kaon structure via generalised parton distributions". In: *Chin. Phys. C* 46.26 (2022), p. 013105. DOI: 10.1088/1674-1137/ac3071. arXiv: 2109.11686 [hep-ph].

[105] Jin-Li Zhang et al. "Measures of pion and kaon structure from generalised parton distributions". In: *Phys. Lett. B* 815 (2021), p. 136158. DOI: 10.1016/j.physletb.2021.136158. arXiv: 2101.12286 [hep-ph].

[106] Shu-Sheng Xu et al. "Pion and kaon valence-quark parton quasidistributions". In: *Phys. Rev. D* 97.9 (2018), p. 094014. DOI: 10.1103/PhysRevD.97.094014. arXiv: 1802.09552 [nucl-th].

[107] M. Atif Sultan et al. "Effect of the quark-gluon vertex on dynamical chiral symmetry breaking". In: *Phys. Rev. D* 103.5 (2021), p. 054036. DOI: 10.1103/PhysRevD.103.054036. arXiv: 1810.01396 [nucl-th].

[108] M. Atif Sultan et al. "Effect of the quark-gluon vertex on dynamical chiral symmetry breaking". In: *Phys. Rev. D* 103.5 (2021), p. 054036. DOI: 10.1103/PhysRevD.103.054036. arXiv: 1810.01396 [nucl-th].

[109] K. Raya et al. "Structure of the neutral pion and its electromagnetic transition form factor". In: *Phys. Rev. D* 93.7 (2016), p. 074017. DOI: 10.1103/PhysRevD.93.074017. arXiv: 1510.02799 [nucl-th].

[110] L. Chang et al. "Pion electromagnetic form factor at spacelike momenta". In: *Phys. Rev. Lett.* 111.14 (2013), p. 141802. DOI: 10.1103/PhysRevLett.111.141802. arXiv: 1307.0026 [nucl-th].

[111] Khepani Raya et al. "Partonic structure of neutral pseudoscalars via two photon transition form factors". In: *Phys. Rev. D* 95.7 (2017), p. 074014. DOI: 10.1103/PhysRevD.95.074014. arXiv: 1610.06575 [nucl-th].

[112] Minghui Ding et al. "$\gamma^*\gamma \to \eta, \eta'$ transition form factors". In: *Phys. Rev. D* 99.1 (2019), p. 014014. DOI: 10.1103/PhysRevD.99.014014. arXiv: 1810.12313 [nucl-th].

[113] Khépani Raya, Adnan Bashir, and Pablo Roig. "Contribution of neutral pseudoscalar mesons to a_μ^{HLbL} within a Schwinger-Dyson equations approach to QCD". In: *Phys. Rev. D* 101.7 (2020), p. 074021. DOI: 10.1103/PhysRevD.101.074021. arXiv: 1910.05960 [hep-ph].

[114] Robert Delbourgo and Peter C. West. "A Gauge Covariant Approximation to Quantum Electrodynamics". In: *J. Phys. A* 10 (1977), p. 1049. DOI: 10.1088/0305-4470/10/6/024.

[115] L. Albino et al. "Transverse Takahashi Identities and Their Implications for Gauge Independent Dynamical Chiral Symmetry Breaking". In: *Phys. Rev. D* 100.5 (2019), p. 054028. DOI: 10.1103/PhysRevD.100.054028. arXiv: 1812.02280 [nucl-th].

[116] R. Bermudez et al. "Quark-gluon Vertex: A Perturbation Theory Primer and Beyond". In: *Phys. Rev. D* 95.3 (2017), p. 034041. DOI: 10.1103/PhysRevD.95.034041. arXiv: 1702.04437 [hep-ph].

[117] Craig D. Roberts and Anthony G. Williams. "Dyson-Schwinger equations and their application to hadronic physics". In: *Prog. Part. Nucl. Phys.* 33 (1994), pp. 477–575. DOI: 10.1016/0146-6410(94)90049-3. arXiv: hep-ph/9403224.

[118] Gernot Eichmann et al. "Baryons as relativistic three-quark bound states". In: *Prog. Part. Nucl. Phys.* 91 (2016), pp. 1–100. DOI: 10.1016/j.ppnp.2016.07.001. arXiv: 1606.09602 [hep-ph].

[119] Fei Gao et al. "Exposing strangeness: projections for kaon electromagnetic form factors". In: *Phys. Rev. D* 96.3 (2017), p. 034024. DOI: 10.1103/PhysRevD.96.034024. arXiv: 1703.04875 [nucl-th].

[120] Gernot Eichmann, Christian S. Fischer, and Richard Williams. "Kaon-box contribution to the anomalous magnetic moment of the muon". In: *Phys. Rev. D* 101.5 (2020), p. 054015. DOI: 10.1103/PhysRevD.101.054015. arXiv: 1910.06795 [hep-ph].

[121] Ángel Miramontes et al. "Pion and Kaon box contribution to a_μ^{HLbL}". In: (Dec. 2021). arXiv: 2112.13916 [hep-ph].

[122] Khepani Raya et al. "Dyson-Schwinger equations and the muon g-2". In: *Suplemento de la Revista Mexicana de Física* 3.2 (2022), pp. 1–9. DOI: 10.31349/SuplRevMexFis.3.020709. arXiv: 2204.01652 [hep-ph].

[123] Lei Chang et al. "Imaging dynamical chiral symmetry breaking: pion wave function on the light front". In: *Phys. Rev. Lett.* 110.13 (2013), p. 132001. DOI: 10.1103/PhysRevLett.110.132001. arXiv: 1301.0324 [nucl-th].

[124] Minghui Ding et al. "Symmetry, symmetry breaking, and pion parton distributions". In: *Phys. Rev. D* 101.5 (2020), p. 054014. DOI: 10.1103/PhysRevD.101.054014. arXiv: 1905.05208 [nucl-th].

[125] Minghui Ding et al. "Drawing insights from pion parton distributions". In: *Chin. Phys. C* 44.3 (2020), p. 031002. DOI: 10.1088/1674-1137/44/3/031002. arXiv: 1912.07529 [hep-ph].

[126] Zhu-Fang Cui et al. "Higgs modulation of emergent mass as revealed in kaon and pion parton distributions". In: *Eur. Phys. J. A* 57.1 (2021), p. 5. DOI: 10.1140/epja/s10050-020-00318-2. arXiv: 2006.14075 [hep-ph].

[127] Zhu-Fang Cui et al. "Kaon and pion parton distributions". In: *Eur. Phys. J. C* 80.11 (2020), p. 1064. DOI: 10.1140/epjc/s10052-020-08578-4.

[128] Z. -F. Cui et al. "Concerning pion parton distributions". In: *Eur. Phys. J. A* 58.1 (2022), p. 10. DOI: 10.1140/epja/s10050-021-00658-7. arXiv: 2112.09210 [hep-ph].

[129] Z. -F. Cui et al. "Emergence of pion parton distributions". In: (Jan. 2022). arXiv: 2201.00884 [hep-ph].

[130] G. Peter Lepage and Stanley J. Brodsky. "Exclusive Processes in Quantum Chromodynamics: Evolution Equations for Hadronic Wave Functions and the Form-Factors of Mesons". In: *Phys. Lett. B* 87 (1979), pp. 359–365. DOI: 10.1016/0370-2693(79)90554-9.

[131] A. V. Efremov and A. V. Radyushkin. "Factorization and Asymptotical Behavior of Pion Form-Factor in QCD". In: *Phys. Lett. B* 94 (1980), pp. 245–250. DOI: 10.1016/0370-2693(80)90869-2.

[132] M. Rinaldi, F. A. Ceccopieri, and V. Vento. "The pion in the graviton soft-wall model: phenomenological applications". In: (Apr. 2022). arXiv: 2204.09974 [hep-ph].

[133] Stanley J. Brodsky, Fu-Guang Cao, and Guy F. de Teramond. "Evolved QCD predictions for the meson-photon transition form factors". In: *Phys. Rev. D* 84 (2011), p. 033001. DOI: 10.1103/PhysRevD.84.033001. arXiv: 1104.3364 [hep-ph].

[134] Lei Chang, Khépani Raya, and Xiaobin Wang. "Pion Parton Distribution Function in Light-Front Holographic QCD". In: *Chin. Phys. C* 44.11 (2020), p. 114105. DOI: 10.1088/1674-1137/abae52. arXiv: 2001.07352 [hep-ph].

[135] Guy F. de Teramond et al. "Universality of Generalized Parton Distributions in Light-Front Holographic QCD". In: *Phys. Rev. Lett.* 120.18 (2018), p. 182001. DOI: 10.1103/PhysRevLett.120.182001. arXiv: 1801.09154 [hep-ph].

[136] J. S. Conway et al. "Experimental study of muon pairs produced by 252-GeV pions on tungsten". In: *Phys. Rev. D* 39 (1 Jan. 1989), pp. 92–122. DOI: 10.1103/PhysRevD.39.92. URL: https://link.aps.org/doi/10.1103/PhysRevD.39.92.

[137] Matthias Aicher, Andreas Schäfer, and Werner Vogelsang. "Soft-Gluon Resummation and the Valence Parton Distribution Function of the Pion". In: *Phys. Rev. Lett.* 105 (25 Dec. 2010), p. 252003. DOI: 10.1103/PhysRevLett.105.252003. URL: https://link.aps.org/doi/10.1103/PhysRevLett.105.252003.

[138] Yuri L. Dokshitzer. "Calculation of the Structure Functions for Deep Inelastic Scattering and e+ e- Annihilation by Perturbation Theory in Quantum Chromodynamics." In: *Sov. Phys. JETP* 46 (1977). [Zh. Eksp. Teor. Fiz.73,1216(1977)], pp. 641–653.

[139] L. N. Lipatov. "The parton model and perturbation theory". In: *Yad. Fiz.* 20 (1974), pp. 181–198.

[140] R. Keith Ellis, W. James Stirling, and B. R. Webber. *QCD and collider physics*. Vol. 8. Cambridge University Press, Feb. 2011. ISBN: 978-0-511-82328-2, 978-0-521-54589-1.

[141] J. S. Conway et al. "Experimental Study of Muon Pairs Produced by 252-GeV Pions on Tungsten". In: *Phys. Rev. D* 39 (1989), pp. 92–122. DOI: 10.1103/PhysRevD.39.92.

[142] J. Badier et al. "Measurement of the K^-/π^- Structure Function Ratio Using the Drell-Yan Process". In: *Phys. Lett. B* 93 (1980), pp. 354–356. DOI: 10.1016/0370-2693(80)90530-4.

[143] Raza Sabbir Sufian et al. "Pion Valence Quark Distribution from Current-Current Correlation in Lattice QCD". In: *Phys. Rev. D* 102.5 (2020), p. 054508. DOI: 10.1103/PhysRevD.102.054508. arXiv: 2001.04960 [hep-lat].

[144] Bálint Joó et al. "Pion valence structure from Ioffe-time parton pseudodistribution functions". In: *Phys. Rev. D* 100.11 (2019), p. 114512. DOI: 10.1103/PhysRevD.100.114512. arXiv: 1909.08517 [hep-lat].

[145] Raza Sabbir Sufian et al. "Pion Valence Quark Distribution from Matrix Element Calculated in Lattice QCD". In: *Phys. Rev. D* 99.7 (2019), p. 074507. DOI: 10.1103/PhysRevD.99.074507. arXiv: 1901.03921 [hep-lat].

[146] José Rodríguez-Quintero et al. "Process-independent effective coupling and the pion structure function". In: *J. Phys. Conf. Ser.* 1643.1 (2020), p. 012177. DOI: 10.1088/1742-6596/1643/1/012177. arXiv: 1909.13802 [hep-ph].

[147] Ya Lu et al. "Proton and pion distribution functions in counterpoint". In: (Mar. 2022). arXiv: 2203.00753 [hep-ph].

[148] Gernot Eichmann et al. "Single pseudoscalar meson pole and pion box contributions to the anomalous magnetic moment of the muon". In: *Phys. Lett. B* 797 (2019). [Erratum: Phys.Lett.B 799, 135029 (2019)], p. 134855. DOI: 10.1016/j.physletb.2019.134855. arXiv: 1903.10844 [hep-ph].

[149] Jozef J. Dudek, Robert G. Edwards, and David G. Richards. "Radiative transitions in charmonium from lattice QCD". In: *Phys. Rev. D* 73 (2006), p. 074507. DOI: 10.1103/PhysRevD.73.074507. arXiv: hep-ph/0601137.

[150] Jozef J. Dudek et al. "Radiative physics in charmonium from lattice QCD". In: *J. Phys. Conf. Ser.* 69 (2007), p. 012006. DOI: 10.1088/1742-6596/69/1/012006.

[151] P.A. Zyla et al. "Review of Particle Physics". In: *PTEP* 2020.8 (2020), p. 083C01. DOI: 10.1093/ptep/ptaa104.

[152] M. S. Bhagwat et al. "Mind the gap". In: *Eur. Phys. J. A* 31 (2007). Ed. by Antonio Dobado, Felipe J. Llanes-Estrada, and Vicente Vento, pp. 630–637. DOI: 10.1140/epja/i2006-10271-9. arXiv: nucl-th/0612027.

[153] Enrique Ruiz Arriola and Wojciech Broniowski. "Solution of the Kwiecinski evolution equations for unintegrated parton distributions using the Mellin transform". In: *Phys. Rev. D* 70 (2004), p. 034012. DOI: 10.1103/PhysRevD.70.034012. arXiv: hep-ph/0404008.

[154] Aurore Courtoy and Pavel M. Nadolsky. "Testing momentum dependence of the nonperturbative hadron structure in a global QCD analysis". In: *Phys. Rev. D* 103.5 (2021), p. 054029. DOI: 10.1103/PhysRevD.103.054029. arXiv: 2011.10078 [hep-ph].

[155] M. S. Bhagwat and P. Maris. "Vector meson form factors and their quark-mass dependence". In: *Phys. Rev.* C77 (2008), p. 025203. DOI: 10.1103/PhysRevC.77.025203. arXiv: nucl-th/0612069 [nucl-th].

[156] Xiang Gao et al. "Pion form factor and charge radius from lattice QCD at the physical point". In: *Phys. Rev. D* 104.11 (2021), p. 114515. DOI: 10.1103/PhysRevD.104.114515. arXiv: 2102.06047 [hep-lat].

[157] C. T. H. Davies et al. "Meson Electromagnetic Form Factors from Lattice QCD". In: *PoS* LATTICE2018 (2018), p. 298. DOI: 10.22323/1.334.0298. arXiv: 1902.03808 [hep-lat].

[158] P. A. Zyla et al. "Review of Particle Physics". In: *PTEP* 2020.8 (2020), p. 083C01. DOI: 10.1093/ptep/ptaa104.

[159] R. J. Lombard and J. Mares. "On the meson charge radii". In: *Phys. Lett.* B472 (2000), pp. 150–154. DOI: 10.1016/S0370-2693(99)01395-7.

[160] Chien-Wen Hwang. "Charge radii of light and heavy mesons". In: *Eur. Phys. J.* C23 (2002), pp. 585–590. DOI: 10.1007/s100520200904. arXiv: hep-ph/0112237 [hep-ph].

[161] T Das, D K Choudhury, and N S Bordoloi. "Charge radii of heavy flavored mesons in a potential model". In: (2016). arXiv: 1608.06896 [hep-ph].

[162] S.R. Amendolia et al. "A measurement of the kaon charge radius". In: *Physics Letters B* 178.4 (1986), pp. 435–440. ISSN: 0370-2693. DOI: https://doi.org/10.1016/0370-2693(86)91407-3. URL: https://www.sciencedirect.com/science/article/pii/0370269386914073.

[163] E. B. Dally et al. "Direct Measurement of the Negative-Kaon Form Factor". In: *Phys. Rev. Lett.* 45 (4 July 1980), pp. 232–235. DOI: 10.1103/PhysRevLett.45.232. URL: https://link.aps.org/doi/10.1103/PhysRevLett.45.232.

[164] J. P. Lees et al. "Measurement of the $\gamma\gamma * --> \eta_c$ transition form factor". In: *Phys. Rev. D* 81 (2010), p. 052010. DOI: 10.1103/PhysRevD.81.052010. arXiv: 1002.3000 [hep-ex].

[165] M. S. Bhagwat and P. Maris. "Vector meson form factors and their quark-mass dependence". In: *Phys. Rev. C* 77 (2 Feb. 2008), p. 025203. DOI: 10.1103/PhysRevC.77.025203. URL: https://link.aps.org/doi/10.1103/PhysRevC.77.025203.

[166] M. S. Bhagwat et al. "Mind the gap". In: *The European Physical Journal A* 31.4 (Mar. 2007), pp. 630–637. ISSN: 1434-601X. DOI: 10.1140/epja/i2006-10271-9. URL: https://doi.org/10.1140/epja/i2006-10271-9.

[167] M. Tanabashi et al. "Review of Particle Physics". In: *Phys. Rev. D* 98 (3 Aug. 2018), p. 030001. DOI: 10.1103/PhysRevD.98.030001. URL: https://link.aps.org/doi/10.1103/PhysRevD.98.030001.

[168] M. Carmignotto et al. "Separated kaon electroproduction cross section and the kaon form factor from 6 GeV JLab data". In: *Phys. Rev. C* 97 (2 Feb. 2018), p. 025204. DOI: 10.1103/PhysRevC.97.025204. URL: https://link.aps.org/doi/10.1103/PhysRevC.97.025204.

[169] Fei Gao et al. "Exposing strangeness: Projections for kaon electromagnetic form factors". In: *Phys. Rev. D* 96 (3 Aug. 2017), p. 034024. DOI: 10.1103/PhysRevD.96.034024. URL: https://link.aps.org/doi/10.1103/PhysRevD.96.034024.

[170] Particle Data Group et al. "Review of Particle Physics". In: *Progress of Theoretical and Experimental Physics* 2020.8 (Aug. 2020), p. 083C01. ISSN: 2050-3911. DOI: 10.1093/ptep/ptaa104. eprint: https://academic.oup.com/ptep/article-pdf/2020/8/083C01/34673722/ptaa104.pdf. URL: https://doi.org/10.1093/ptep/ptaa104.

[171] S. R. Amendolia et al. "A Measurement of the Kaon Charge Radius". In: *Phys. Lett. B* 178 (1986), pp. 435–440. DOI: 10.1016/0370-2693(86)91407-3.

[172] Feng Feng, Yu Jia, and Wen-Long Sang. "Can Nonrelativistic QCD Explain the $\gamma\gamma^* \to \eta_c$ Transition Form Factor Data?" In: *Phys. Rev. Lett.* 115.22 (2015), p. 222001. DOI: 10.1103/PhysRevLett.115.222001. arXiv: 1505.02665 [hep-ph].

[173] K. A. Olive et al. "Review of Particle Physics". In: *Chin. Phys. C* 38 (2014), p. 090001. DOI: 10.1088/1674-1137/38/9/090001.

[174] W. de Paula et al. "Parton distribution function in a pion with Minkowskian dynamics". In: *Phys. Rev. D* 105.7 (2022), p. L071505. DOI: 10.1103/PhysRevD.105.L071505. arXiv: 2203.07106 [hep-ph].

[175] Gernot Eichmann, Eduardo Ferreira, and Alfred Stadler. "Going to the light front with contour deformations". In: *Phys. Rev. D* 105.3 (2022), p. 034009. DOI: 10.1103/PhysRevD.105.034009. arXiv: 2112.04858 [hep-ph].